Non destructive analysis of grain sub-structuration in single grains of an Aluminium polycrystal deformed in uniaxial tension.

Ernesto Francesco Filippelli

N° d'ordre NNT: 2017LYSEM001

PROJET DE THÈSE DE L'UNIVERSITÉ DE LYON

opérée au sein de

l'École des Mines de Saint-Étienne

École doctorale N°488

Sciences, Ingénierie, Santé

Spécialité de doctorat : Science et Génie des Matériaux

présenté par

Ernesto Francesco Filippelli

Non destructive analysis of grain sub-structuration in single grains of an Aluminium polycrystal deformed in uniaxial tension

–

Analyse non destructive de la sous-structuration des grains individuels dans un polycrystal d'aluminium déformé en traction uniaxiale

---

Devant le jury composé de :

Rapporteurs :	Laszlo	TOTH	Professeur, LEM3, Université de Lorraine
	Henry	PROUDHON	Chargé de Recherche CNRS, Mines ParisTech
Examinateurs :	Nathalie	BOZZOLO	Professeur, CEMEF Mines ParisTech
	Gilbert	CHAHINE	Docteur, Chercheur ESRF
	Claire	MAURICE	Chargée de Recherche CNRS, ENSM-SE
Directeur de thèse:	András	BORBÉLY	Directeur de recherche, ENSM-SE
Co-directrice de thèse :	Anna	FRACZKIEWICZ	Directrice de recherche, ENSM-SE

Spécialités doctorales	Responsables :	Spécialités doctorales	Responsables
SCIENCES ET GENIE DES MATERIAUX	K. Wolski Directeur de recherche	MATHEMATIQUES APPLIQUEES	O. Roustant, Maître-assistant
MECANIQUE ET INGENIERIE	S. Drapier, professeur	INFORMATIQUE	O. Boissier, Professeur
GENIE DES PROCEDES	F. Gruy, Maître de recherche	IMAGE, VISION, SIGNAL	JC. Pinoli, Professeur
SCIENCES DE LA TERRE	B. Guy, Directeur de recherche	GENIE INDUSTRIEL	A. Dolgui, Professeur
SCIENCES ET GENIE DE L'ENVIRONNEMENT	D. Graillot, Directeur de recherche	MICROELECTRONIQUE	S. Dauzere Peres, Professeur

EMSE : Enseignants-chercheurs et chercheurs autorisés à diriger des thèses de doctorat (titulaires d'un doctorat d'État ou d'une HDR)

ABSI	Nabil	CR	Génie industriel	CMP
AVRIL	Stéphane	PR2	Mécanique et ingénierie	CIS
BALBO	Flavien	PR2	Informatique	FAYOL
BASSEREAU	Jean-François	PR	Sciences et génie des matériaux	SMS
BATTAIA-GUSCHINSKAYA	Olga	CR		FAYOL
BATTON-HUBERT	Mireille	PR2	Sciences et génie de l'environnement	FAYOL
BERGER DOUCE	Sandrine	PR2	Sciences de gestion	FAYOL
BIGOT	Jean Pierre	MR(DR2)	Génie des Procédés	SPIN
BILAL	Essaid	DR	Sciences de la Terre	SPIN
BLAYAC	Sylvain	MA(MDC)	Microélectronique	CMP
BOISSIER	Olivier	PR1	Informatique	FAYOL
BONNEFOY	Olivier	MA(MDC)	Génie des Procédés	SPIN
BORBELY	Andras	MR(DR2)	Sciences et génie des matériaux	SMS
BOUCHER	Xavier	PR2	Génie Industriel	FAYOL
BRODHAG	Christian	DR	Sciences et génie de l'environnement	FAYOL
BRUCHON	Julien	MA(MDC)	Mécanique et ingénierie	SMS
BURLAT	Patrick	PR1	Génie Industriel	FAYOL
COURNIL	Michel	PR0	Génie des Procédés	DIR
DARRIEULAT	Michel	IGM	Sciences et génie des matériaux	SMS
DAUZERE-PERES	Stéphane	PR1	Génie Industriel	CMP
DEBAYLE	Johan	CR	Image Vision Signal	CIS
DELAFOSSE	David	PR0	Sciences et génie des matériaux	SMS
DELORME	Xavier	MA(MDC)		FAYOL
DESRAYAUD	Christophe	PR1	Mécanique et ingénierie	SMS
DOLGUI	Alexandre	PR0	Génie Industriel	FAYOL
DRAPIER	Sylvain	PR1	Mécanique et ingénierie	SMS
FAVERGEON	Loïc	CR	Génie des Procédés	SPIN
FEILLET	Dominique	PR1	Génie Industriel	CMP
FRACZKIEWICZ	Anna	DR	Sciences et génie des matériaux	SMS
GARCIA	Daniel	MR(DR2)	Génie des Procédés	SPIN
GAVET	Yann	MA(MDC)	Image Vision Signal	CIS
GERINGER	Jean	MA(MDC)	Sciences et génie des matériaux	CIS
GOEURIOT	Dominique	DR	Sciences et génie des matériaux	SMS
GRAILLOT	Didier	DR	Sciences et génie de l'environnement	SPIN
GROSSEAU	Philippe	DR	Génie des Procédés	SPIN
GRUY	Frédéric	PR1	Génie des Procédés	SPIN
GUY	Bernard	DR	Sciences de la Terre	SPIN
HAN	Woo-Suck	MR	Mécanique et ingénierie	SMS
HERRI	Jean Michel	PR1	Génie des Procédés	SPIN
KERMOUCHE	Guillaume	PR2	Mécanique et Ingénierie	SMS
KLOCKER	Helmut	DR	Sciences et génie des matériaux	SMS
LAFOREST	Valérie	MR(DR2)	Sciences et génie de l'environnement	FAYOL
LERICHE	Rodolphe	CR	Mécanique et ingénierie	FAYOL
LI	Jean-Michel		Microélectronique	CMP
MALLIARAS	Georges	PR1	Microélectronique	CMP
MAURINE	Philippe	Ingénieur de recherche		CMP
MOLIMARD	Jérôme	PR2	Mécanique et ingénierie	CIS
MONTHEILLET	Frank	DR	Sciences et génie des matériaux	SMS
MOUTTE	Jacques	CR	Génie des Procédés	SPIN
NEUBERT	Gilles	PR		FAYOL
NIKOLOVSKI	Jean-Pierre	Ingénieur de recherche		CMP
NORTIER	Patrice	PR1		SPIN
OWENS	Rosin	MA(MDC)		CMP
PICARD	Gauthier	MA(MDC)		FAYOL
PIJOLAT	Christophe	PR0	Génie des Procédés	SPIN
PIJOLAT	Michèle	PR1	Génie des Procédés	SPIN
PINOLI	Jean Charles	PR0	Image Vision Signal	CIS
POURCHEZ	Jérémy	MR	Génie des Procédés	CIS
ROBISSON	Bruno	Ingénieur de recherche		CMP
ROUSSY	Agnès	MA(MDC)	Génie industriel	CMP
ROUSTANT	Olivier	MA(MDC)	Mathématiques appliquées	FAYOL
ROUX	Christian	PR	Image Vision Signal	CIS
STOLARZ	Jacques	CR	Sciences et génie des matériaux	SMS
TRIA	Assia	Ingénieur de recherche	Microélectronique	CMP
VALDIVIESO	François	PR2	Sciences et génie des matériaux	SMS
VIRICELLE	Jean Paul	DR	Génie des Procédés	SPIN
WOLSKI	Krzystof	DR	Sciences et génie des matériaux	SMS
XIE	Xiaolan	PR1	Génie industriel	CIS
YUGMA	Gallian	CR	Génie industriel	CMP

ENISE : Enseignants-chercheurs et chercheurs autorisés à diriger des thèses de doctorat (titulaires d'un doctorat d'État ou d'une HDR)

BERGHEAU	Jean-Michel	PU	Mécanique et Ingénierie	ENISE
BERTRAND	Philippe	MCF	Génie des procédés	ENISE
DUBUJET	Philippe	PU	Mécanique et Ingénierie	ENISE
FEULVARCH	Eric	MCF	Mécanique et Ingénierie	ENISE
FORTUNIER	Roland	PR	Sciences et Génie des matériaux	ENISE
GUSSAROV	Andrey	Enseignant contractuel	Génie des procédés	ENISE
HAMDI	Hédi	MCF	Mécanique et Ingénierie	ENISE
LYONNET	Patrick	PU	Mécanique et Ingénierie	ENISE
RECH	Joël	PU	Mécanique et Ingénierie	ENISE
SMUROV	Igor	PU	Mécanique et Ingénierie	ENISE
TOSCANO	Rosario	PU	Mécanique et Ingénierie	ENISE
ZAHOUANI	Hassan	PU	Mécanique et Ingénierie	ENISE

Mise à jour : 11/05/2015

Table of contents

Introduction

In most cases, the materials used in industrial applications are made up of polycrystals. Understanding their behavior under complex thermomechanical loads is of central importance for engineering applications, as well as for the development of novel materials with improved performances. For this reason, a large field of research is interested in the study of plastic deformation of metals. Plasticity of metals is an irreversible process that leads to a permanent change within the material and results in a macroscopic change of shape. At the sub-micron scale this change is the product of the collective behavior of linear defects of the atomic lattice called dislocations, discovered by Orowan, Polanyi and Taylor in 1934. During plastic deformation the dislocations form complex patterns, such as cell structures for example, which are separated by dislocation boundaries. With increasing deformation the boundaries become more visible as the crystallographic misorientation between adjacent regions they separate steadily increases. This phenomenon is often referred to as grain subdivision or grain fragmentation.

There are several experimental methods for the study of deformation induced dislocation structures. Due to its high spatial resolution the Transmission Electron Microscope (TEM) seems to be the most adequate one to analyse dislocations and dislocation structures. It allowed gaining insight on the prevailing dislocation types, their organization in patterned structures or on local stresses [1]. Obtaining statistical information, however, was difficult due to the large amount of the work involved, therefore alternative methods for their characterization have been developed. X-ray diffraction usually used for structure determination represented a good opportunity and as evidenced by the pioneering works by Warren and Krivoglaz, peak broadening can be related to the density of lattice defects (mean square strain) and to the so called particle or coherent domain size [2]. This allowed the development Line Profile Analysis (LPA), which interprets peak broadening in terms of the average dislocation density. Recently, the development of synchrotron sources was of central importance, establishing a powerful instrument for materials science. Thanks to their high energy and highly brilliant beams the exposure time of such measurements has been considerably reduced, facilitating novel in situ experiments, which may lead to a better understanding of the deformation process and the evolution of dislocation structures.

Over the last decades, by exploiting the improvement of the Scanning Electron Microscope (SEM), major efforts have been undertaken for the development of the backscattered electron diffraction (EBSD) technique, which has the power to provide

local crystallographic orientation and creation of orientation maps of relatively large regions of several millimeter square and with resolutions of the order of tens of nanometers. Furthermore, high angular resolution electron backscatter diffraction (HR-EBSD) was also developed, which is capable to measure residual elastic strain and lattice rotation with very high precision [3, 4]. The latter technique may open new ways for studying strain localization and damage initiation in polycrystalline materials.

Although many studies were already focused on dislocation patterning during the last decades, further work is needed to improve the comprehension of plastic deformation of polycrystalline materials and subdivision mechanisms of their grains. This work aims to address this subject by using non-destructive in situ techniques based on hard synchrotron radiation and classical EBSD. The main questions we want to answer are related to the creation and the evolution of the deformation induced dislocation structures. The study will be mainly conducted by analysing the orientation spread developed in individual grains and its correlation with the grain average orientation and size.

This manuscript is organised into five chapters; the bibliographic review, presented in Chapter 1, summarizes the theory of dislocations as well as the mechanisms of formation of the geometrically necessary boundaries. The state of the art regarding the characterization of dislocation structures is presented, together with the theoretical models available in the literature about grain fragmentation. The experimental devices used for the investigation of the orientation distribution arising during deformation are described in Chapter 2, that is divided in two parts: first, the 3DXRD setup available at the ID11 beamline of the European Synchrotron Radiation Facility (ESRF) is illustrated, paying specific attention to the description of the test parameters we chose for our experiment and to the post-treatment of the recorded data. The second part regards the description of the experimental protocol based on the EBSD technique. In Chapter 3 we present the results derived from the 3DXRD analysis: we present the algorithm developed for characterizing the orientation spread of individual grains of a polycrystal starting from diffraction spots, as well as the evolution of intragranular orientation gradients during deformation. Chapter 4 shows the comparison with the EBSD results, as well as the investigation of grain subdivision dynamics. Finally, Chapter 5 illustrates the application of a novel X-Ray scanning technique to the study of deformed polycrystals. The K-map method, developed at the ID01 beamline at the ESRF, was used to complete the EBSD investigations, providing an intragranular strain map as well as the dislocation density arising in deformed single grains.

1 Bibliographic background

Contents

The aim of this chapter is to introduce the basic notions of dislocation theory and dislocation interaction with grain boundaries, in order to introduce the work which has been realised in this thesis. In the first part, after a brief presentation of the basic principles of dislocation structure and glide, we discuss their arrangement in regular arrays that are at the origin of orientation gradients built during deformation. The second part is dedicated to recent advances in dislocation structures characterization, carried out by means of the classical electron and X-Rays based techniques. Finally, we discuss about the theory of interaction between dislocations and grain boundaries, presenting the simplest mode of arrangement of line defects in the proximity of the boundary.

1.1 Basic notions of dislocation theory

From a theoretical point of view, the macroscopic deformation of crystals is reached when the interatomic forces are high enough to break the atomic bonds between two adjacent atoms of the crystal lattice. In spite of this, experimental observations showed that the yield stress is much lower than the theoretical one: this is caused by the presence of defects in the crystal, called dislocations, which are linear defects whose displacement causes the deformation of the material under an applied stress.

1.1.1 Burgers vector of a dislocation

The description of a dislocation is usually given in terms of its *Burgers vector*, whose definition is linked to the definition of the *Burgers circuit C* surrounding the dislocation line. The Burgers vector is a quantity that represents the magnitude and the direction of dislocation displacement.

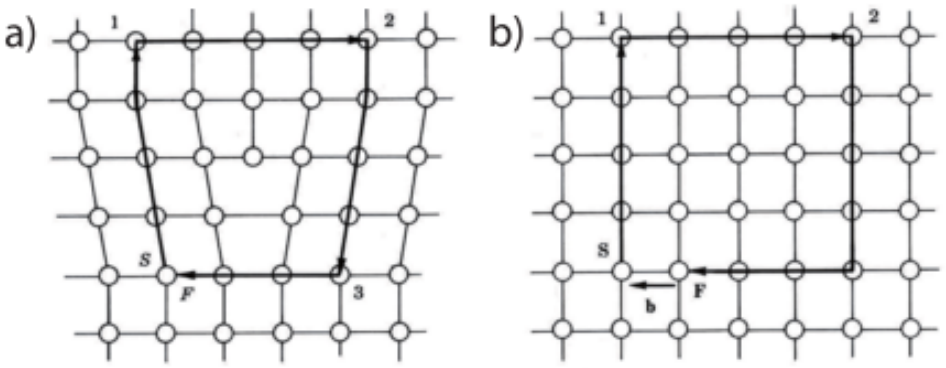

Figure 1.1 – *(a) Burgers circuit around an edge dislocation. (b) The Burgers vector corresponds to the missing quantity that would be necessary to close the Burgers circuit in the perfect crystal [5].*

The Burgers circuit is an atom-to-atom path traced around the linear defect, which forms a closed loop, as illustrated in the Figure 1.1. Now we can trace the same circuit in a dislocation-free crystal, then the resulting path is no more closed: the closure failure is represented by the *Burgers vector* of the dislocation. The mathematical description of the Burgers vector is given by the Equation 1.1.

$$\vec{b} = \oint_C \frac{\partial \vec{u}}{\partial l} dl \tag{1.1}$$

In the Figure 1.1, the Burgers vector is perpendicular to the dislocation line direction, which is the case of an *edge dislocation*. For *screw dislocations*, the displacement direction is parallel to the dislocation line, converting the atomic planes into a helical surface. In the most general case, the dislocation line is never straight, but undulates through the crystal, although the Burgers vector remains constant. So, the dislocation character can be edge-like in some regions, screw or mixed in others, and the angle between the line direction and the Burgers vector varies in the range between 0° and 90°.

1.1.2 Movement of dislocations

If a high enough stress acts on a dislocation line, the dislocation can move and deform the crystal. The movement of an edge dislocation is showed in the Figure 1.2.

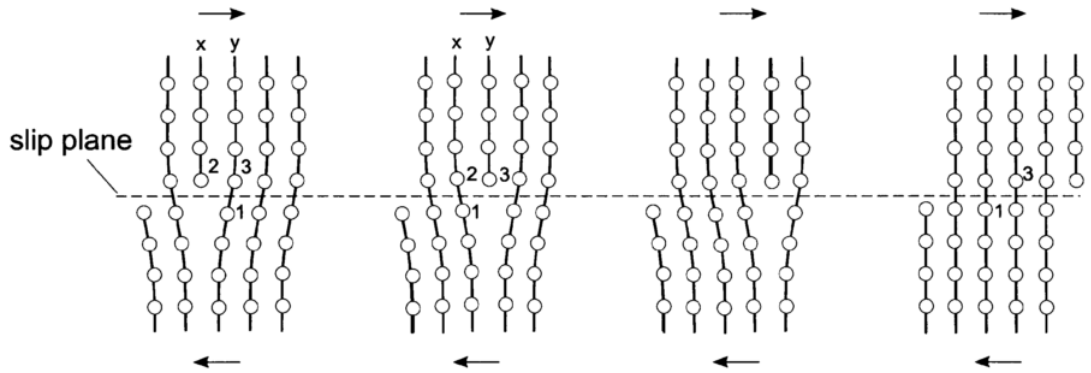

Figure 1.2 – *Movement of an edge dislocation under an applied shear stress [6].*

In the proximity of the dislocation line the stress field causes the displacement of atoms from their equilibrium position. If a shear stress is applied to the crystal, trying to move the upper part with respect to the lower part, the atomic bonds are stretched, and the dislocation is able to propagate to the nearest vertical atomic plane. This process is repeated until the upper and the lower part of the crystal are displaced each from the other. The edge dislocation moves in a *slip plane* that is defined by the line direction and the Burgers vector. This is an irreversible process, since the dislocation does not come back to its starting point when the crystal is unloaded. A gliding dislocation does not change the volume of the crystal. This is the reason why we can assume that the macroscopic volume of materials does not change during the plastic deformation.

1.1.3 Slip systems

At low temperatures, the most common way in which dislocations move through the crystal is *glide*. We saw that, during dislocation movement, the upper part of the crystal slips with respect to the lower one: the plane separating these two zones is called *the glide plane* which together with the *the slip direction* defines a *slip system*. For an edge dislocation the slip direction is also the direction of the dislocation movement, while for screw dislocations, these directions are perpendicular. The preferred slip systems can vary, depending on material structure and atomic bonding (some examples are given in Table 1.1). Normally, easy slip planes are the planes in which the atomic packing is the most dense.

Slip systems can be represented by means of the stereographic projection 1.3. Every slip system can be linked to a stereographic triangle. When a mechanical stress acts on the crystal and if the stress axis lies in the centre of a stereographic triangle, the associated slip system is preferentially activated. If the projection of this axis lies at the border between two triangles, the two related slip systems are equally activated. The slip activity can be observed at the surface of the deformed

Table 1.1 – *Glide planes and glide directions of different types of materials [7].*

Crystal	Burgers vector (glide direction)	Glide plane
fcc metal	$\frac{1}{2}\langle 110\rangle$	{111},{110},{100}
bcc metal	$\frac{1}{2}\langle 111\rangle$,$\langle 100\rangle$	{110},{112},{123}
hcp metal	$\frac{1}{3}\langle 11\bar{2}0\rangle$, $\langle 0001\rangle$, $\frac{1}{3}\langle 11\bar{2}3\rangle$	(0001),{$1\bar{1}00$}
Bl (Na-Cl type)	$\langle 110\rangle$	{110},{100},{111}
Quartz	$\frac{1}{3}\langle 11\bar{2}0\rangle$, $\langle 0001\rangle$, $\frac{1}{3}\langle 11\bar{2}3\rangle$	(0001),{$10\bar{1}0$},{$10\bar{1}1$}
Spinel	$\frac{1}{2}\langle 110\rangle$	{110},{111},{100}
Garnet	$\frac{1}{2}\langle 111\rangle$,$\langle 100\rangle$	{110}
Olivine	[100],[001]	(010),(100),(001),{0kl}
Orthopyroxene	[001]	(100),(010)
Clinopyroxene	[001]	(100)
Wadsleyite	[100],[001],$\frac{1}{2}\langle 111\rangle$	{0kl},{$1\bar{1}0$}
Perovskite(cubic)	$\langle 100\rangle$,$\langle 110\rangle$	{100},{110}
Perovskite ($CaTiO_3$)	[100]	(010)
Ilmenite	$\frac{1}{3}\langle 11\bar{2}0\rangle$	(0001)

crystal, when its orientation is favourable. The figure 1.4, shows the formation of slip bands due to dislocation glide.

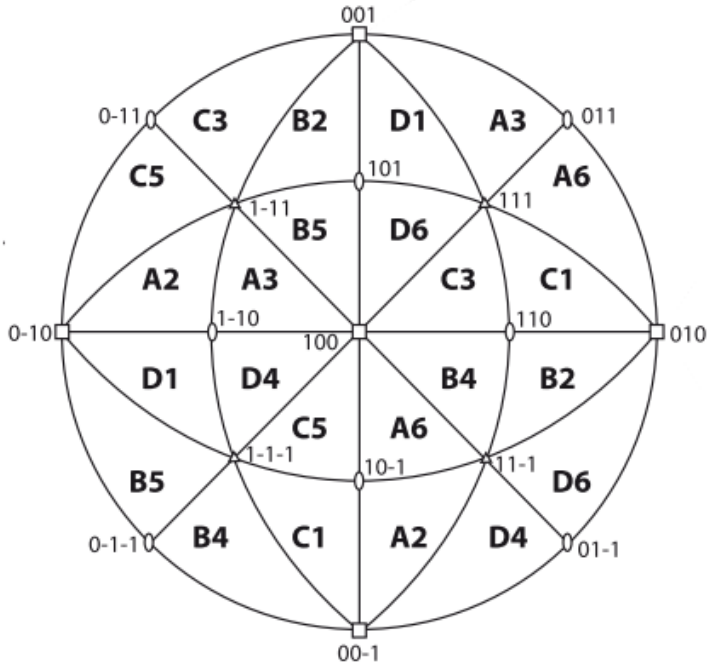

Figure 1.3 – *Stereographic projection of the most active slip systems when the stress axis lies in the corresponding triangle [8].*

In this work an Al 0.1%Mn alloy was used, which has a face-centred cubic struc-

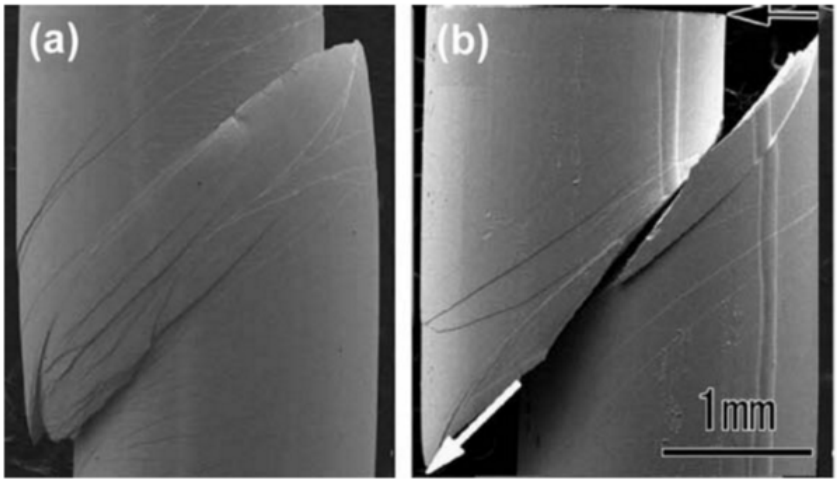

Figure 1.4 – *SEM observation of the formation of slip bands at the surface of a single crystal, due to dislocation glide [9].*

ture. Planes of type $\{111\}$ and directions of type $\langle 110 \rangle$ are close-packed, which correspond to slip planes and directions at room temperature. If we consider the planes of opposite Miller indices as the same one, there are four different slip planes and three slip directions for each. We have then 12 independent slip systems in this Bravais lattice at room temperature. For an edge dislocation, the Burgers vector and the dislocation line direction are perpendicular, so the slip plane can uniquely be defined as:

$$\vec{n} = \frac{\vec{b} \times \vec{t}}{\| \vec{b} \times \vec{t} \|} \tag{1.2}$$

For screw dislocations, the Burgers vector and the dislocation line direction are parallel, so the slip plane is not defined uniquely. Screw dislocations can glide on several planes and overcome obstacles by *cross slip*. Edge dislocations can show a different mechanism of overcoming the obstacles, but only at high temperatures, the so-called *climb*.

1.1.4 Interactions between dislocations

The atoms of a crystal containing dislocations are not at their equilibrium position. This is source of internal stresses in the crystal, and the resulting distortion creates the *stress field* around the dislocation and in the whole material. The crystal is not in its lowest energy state, this extra energy is minimized through the interaction between the stress field of adjacent dislocations. Consider two edge dislocations lying in the same slip plane with the same sign of their Burgers vector. When they are very close together, the total strain energy is much higher than that they would have if they were separated by a long distance: the two dislocations repeal each other. Conversely, two dislocations with opposite sign attract each other, since

the total strain energy would be equal to zero. Similar conclusions are true also for two dislocations that do not lie in the same slip plane, but their interaction mechanism is more complicated. Consider two dislocations lying parallel to the z axis, as shown in Figure 1.5. The total energy of the system is composed of the self-energy of dislocation I, the self-energy of dislocation II, and the *interaction energy* E_{int} that is necessary to propagate the cut in the presence of the stress field of the other dislocation. By visualising the cut parallel to the x or y axis, two alternative expressions are proposed for E_{int} per unit length of dislocation:

$$\mathrm{E_{int}} = + \int_{\mathrm{x}}^{\infty} (\mathrm{b_x}\sigma_{\mathrm{xy}} + \mathrm{b_y}\sigma_{\mathrm{yy}} + \mathrm{b_z}\sigma_{\mathrm{zy}})\mathrm{dx} \tag{1.3}$$

$$\mathrm{E_{int}} = - \int_{\mathrm{y}}^{\infty} (\mathrm{b_x}\sigma_{\mathrm{xx}} + \mathrm{b_y}\sigma_{\mathrm{yx}} + \mathrm{b_z}\sigma_{\mathrm{zx}})\mathrm{dy} \tag{1.4}$$

where the stress components are due to dislocation I. The interaction force on dislocation II is obtained simply deriving these expressions:

$$\mathrm{F_x} = -\frac{\partial \mathrm{E_{int}}}{\partial \mathrm{x}} \tag{1.5}$$

$$\mathrm{F_y} = -\frac{\partial \mathrm{E_{int}}}{\partial \mathrm{y}} \tag{1.6}$$

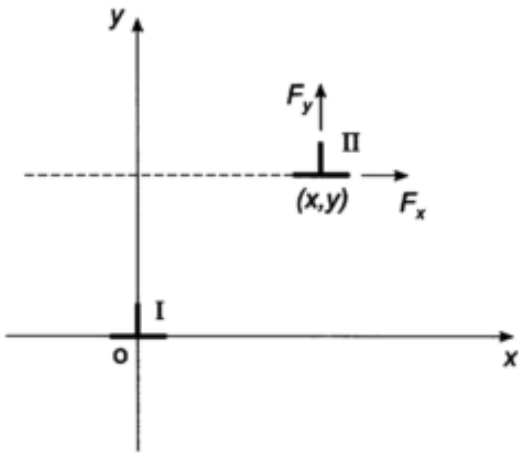

Figure 1.5 – *Interaction between two edge dislocations lying on different slip planes [6].*

For the edge dislocations of Figure 1.5, $\vec{b} = b_x$ and $b_y = b_z = 0$. The two expressions 1.5 and 1.6 are thus equal to:

$$\mathrm{F_x} = \mathrm{b_x}\sigma_{\mathrm{xy}} \tag{1.7}$$

$$\mathrm{F_y} = -\mathrm{b_x}\sigma_{\mathrm{xx}} \tag{1.8}$$

Since dislocations can glide on the slip plane, the most important component in determining dislocations behaviour is F_x. Substituting the expression of σ_{xy} [6] in the Equation 1.7, we have:

$$\mathrm{F_x} = \frac{\mathrm{Gb^2}}{2\pi(1-\nu)} \frac{\mathrm{x(x^2-y^2)}}{\mathrm{(x^2+y^2)^2}} \tag{1.9}$$

where G is the shear modulus of the material. The sign of F_x, hence its nature, is dependent on the ratio x/y. This force is attractive for $-y<x<y$ and repulsive elsewhere. Such a behaviour is inverted in the case of two unlike dislocations, as shown in the Figure 1.6.

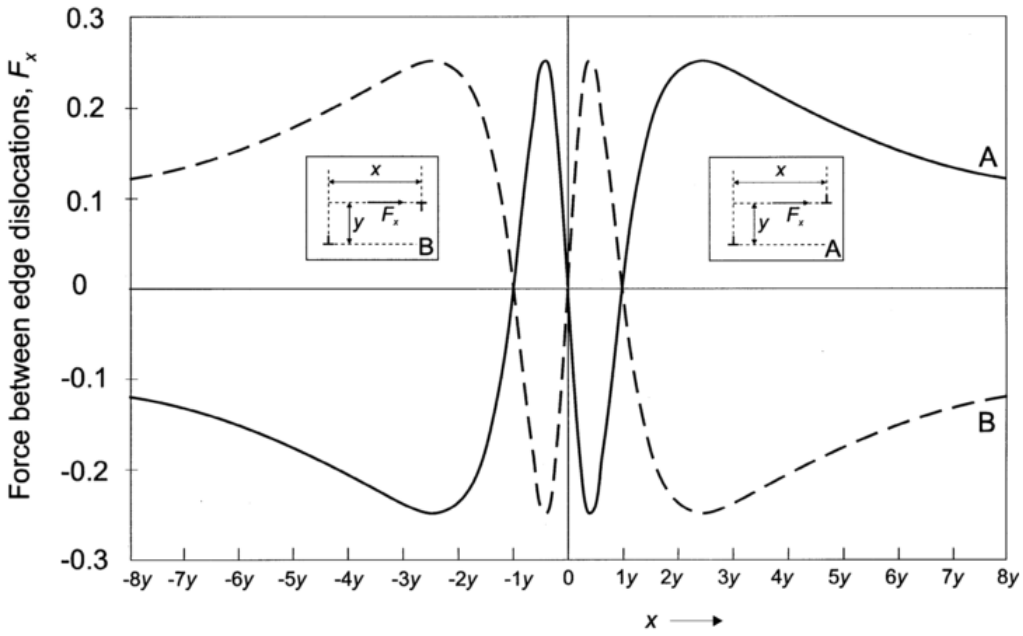

Figure 1.6 – *Variation of Fx with dislocation relative position. The full curve A is relative to dislocations of the same type, the broken curve B to unlike dislocations [6].*

Two edge dislocations of the same sign are in equilibrium position at x = 0 for every value of y. It follows that a vertical array composed of this kind of dislocation is stable. This is the simplest structure of low angle boundary, the *tilt boundary*. The reduction of the extra strain energy is the reason why, during plastic deformation, dislocations interact in order to form ordered arrays. The stress field of such a structure can be calculated simply as the summation of the contributions of single dislocations. The wall applies a stress onto a dislocation which actually is in its proximity. The Figure 1.7 indicates the regions in which the single dislocation is attracted or pushed away by the wall.

The Figure 1.7 can also explain the mechanism of formation of low angle boundaries during *recovery*. The edge dislocation, which initially lie in the repulsive region, can climb thanks to the high temperature, reaching the attractive region and occupying an equilibrium a position in the wall.

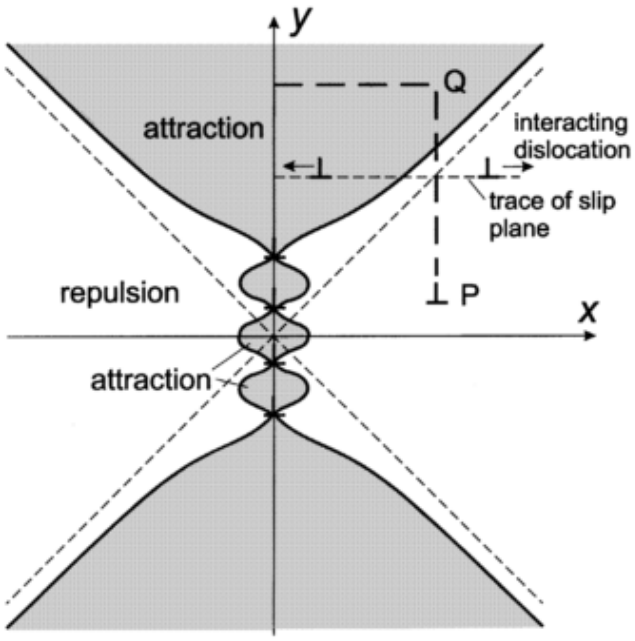

Figure 1.7 – *Dislocation wall composed of four edge dislocations with the same sign. Edge dislocations gliding on a parallel slip plane can be attracted (shaded regions) or repelled [6].*

1.1.5 The Schmid factor

The activation of a slip system under an applied macroscopic stress is governed by the Schmid law, which states that dislocation glide begins when a critical shear stress is reached on a slip plane in a slip direction. In the case of an uniaxial applied stress shown in the Figure 1.8, the slip system is activated when the *resolved shear stress* on this plane and in this direction reaches a critical value τ_{cr}. The criterion can be expressed through the formula:

$$\tau_{\mathrm{ns}} = \sigma \cos\lambda \cos\phi = \tau_{\mathrm{cr}} \tag{1.10}$$

where τ_{ns} is the resolved shear stress on the slip plane, with normal n in the slip direction s. The term $\cos\lambda$ indicates the cosine of the angle between the tensile axis and the slip direction, and $\cos\phi$ is the cosine of the angle between the tensile direction and the normal of the slip plane. Finally, τ_{cr} is the critical resolved shear stress.

In the most general case, the applied stress is multi-axial, so we need to take into account the contribution of the six independent components of the stress tensor to calculate the total resolved shear stress on the considered slip system. The equation 1.10 can be generalised as:

$$\tau_{\mathrm{ns}}{}^{\mathrm{m}} = \mathrm{t}_{\mathrm{ij}}{}^{\mathrm{m}} \sigma_{\mathrm{ij}} \tag{1.11}$$

where $t_{ij}{}^{\mathrm{m}}$ is the Schmid tensor relative to the slip system m, which is defined as:

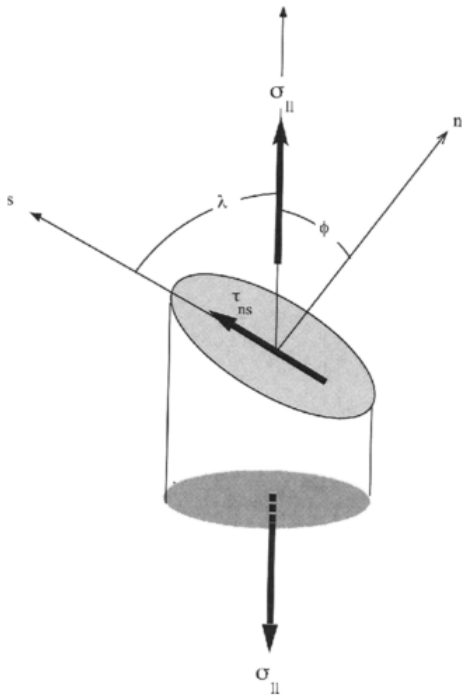

Figure 1.8 – *Schematic view of the Schmid criterion for the activation of a slip system under an uniaxial applied stress. [10].*

$$t_{ij}{}^{m} = \frac{1}{2}(s_i{}^{m}n_j{}^{m} + s_j{}^{m}n_i{}^{m}) \tag{1.12}$$

1.2 Geometrically Necessary and Incidental Dislocation Boundaries

A deformed grain normally presents a relatively high dislocation density. It is always possible to revert it to the undeformed state, through a thermal treatment, known as *recrystallization*. After this process, deformed grains are replaced by new grains which nucleate and grow until the original grains are entirely consumed. The spread between the local orientation within a grain and its mean orientation is very little in this case. If a stress is now applied to the material, grains deform and orientation gradients within them appear. In this section, we will discuss the mechanism of this process, which is strictly linked to the organization of dislocations into regular arrays.

In the previous section, we saw that glide dislocations tend to assemble into ordered dislocation boundaries. Microscopically, such boundaries appear as *dense dislocation walls* or *microbands* [11]. In general, two types of dislocation boundaries may result from plastic deformation of crystalline materials [12]. Grains can be subdivided into equi-axed zones with a low dislocation density, separated by dense dislocation walls, called *Incidental Dislocation Boundaries (IDB)*, resulting from the statistical

mutual trapping of glide dislocations. The net Burgers vector of such structure is zero and because dislocations are randomly distributed there is no any geometrical consequence on the crystal shape [13]. In this work, we will focus on the other type of arrangement, known as *Geometrically Necessary Boundary (GNB)*. These ordered structures having a non-zero net Burgers vector, are composed of dislocations coming from different slip systems and accommodate lattice misorientations that arise during plastic deformation.

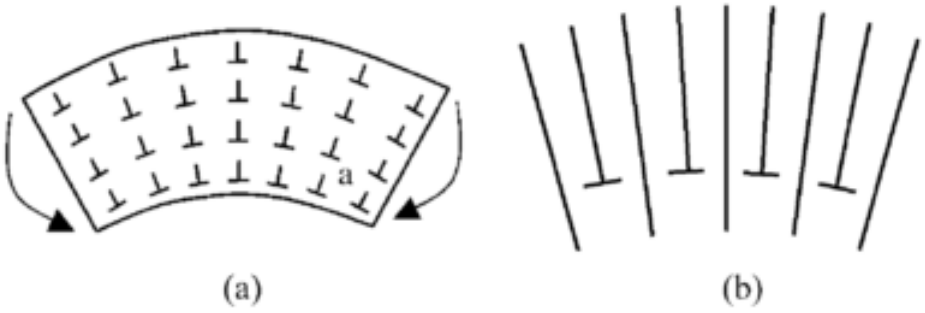

Figure 1.9 – *Geometrically necessary dislocations arrangement accommodating the crystal curvature (a). Schematic view of geometrically necessary dislocations in the plastically bent lattice (b) [14].*

This dislocation storage causes disorientation across the boundaries. The higher is the deformation within the grain, the higher is the dislocation density within the wall, and the disorientation angle between the adjacent regions increases. Due to their geometrical differences, the disorientation angle across a GNB grows much more quickly with the equivalent strain than in the case of an IDB [15].

The importance of GNB in accommodating lattice curvature can be easily depicted through a simple example [14]. The Figure 1.9 shows a bent metal beam, in which a certain number of geometrically necessary dislocations must be present to accommodate the lattice curvature. Moreover, such dislocation structure acts as an obstacle to further dislocation movement, and hence contributes to the *work hardening* of the material. Previously, we saw that dislocations gather into regular clusters in order to reduce by screening their long-range stress field. Now, one can wonder what is the mechanism of formation of dislocation walls. Plastic shear strains cause lattice rotations as a simple geometrical effect. In real polycrystals, grain deformation is not homogeneous, due to the presence of grain boundaries. Consequently, less than five slip systems can operate in different areas of the grain [16]. Hence, the different shear strain and active slip systems give rise to a boundary accounting for the rotation between two adjacent volume elements. Its dislocation content is provided by the gliding dislocations that stop at the boundary.

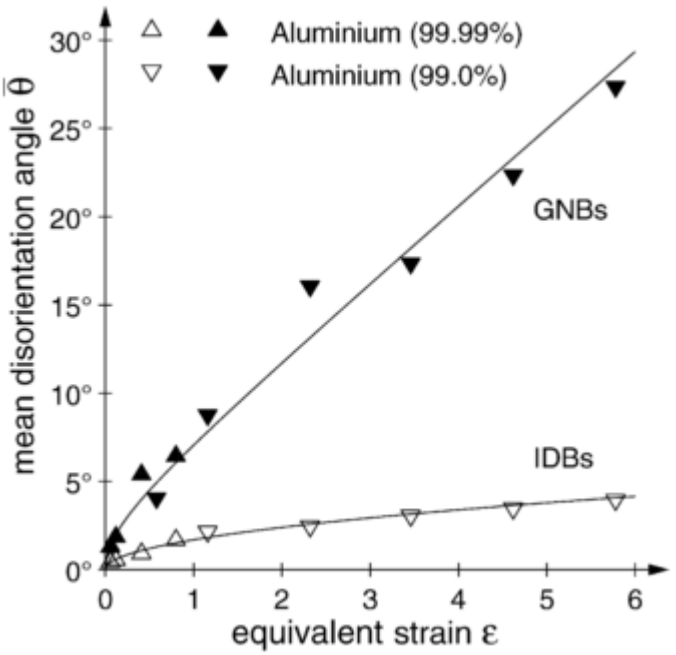

Figure 1.10 – *Evolution of the mean disorientation angle across the boundaries (both GNB and IDB) during cold-rolling, for two different Aluminium alloys (99.99% and 99%) [15].*

1.3 Recent advances in dislocation wall characterization

Dislocation structures play a very important role in the *work hardening* of materials, since they act as obstacles to further movement of dislocations: hence, the characterization of dislocation walls structure and density has a great scientific interest. Many authors carried out characterization studies, mainly by Transmission Electron Microscopy (TEM) and X-Ray Diffraction (XRD).

1.3.1 Analysis by Transmission Electron Microscopy

Thanks to its high spatial resolution, Transmission Electron Microscopy provided a complete characterization of dislocation arrangements and their formation mechanisms. Geometrically necessary boundaries are seen as parallel, almost straight lines, and the incidental dislocation boundaries as short curved segments. Such observations allowed to distinguish among three types of possible configurations [17]:

Type 1: Grains are subdivided by long and straight dislocation boundaries (GNB) aligned with {111} crystallographic planes. Such structures, named *crystallographic boundaries*, form cell blocks containing ordinary dislocation cells.

Type 2: Grains are subdivided by GNBs as for Type 1, but they are not aligned with {111} planes. Hence, these structures are named *non crystallographic boundaries*.

Type 3: Grains are subdivided by Incidental Dislocation Boundaries forming a

three dimensional cell structure.

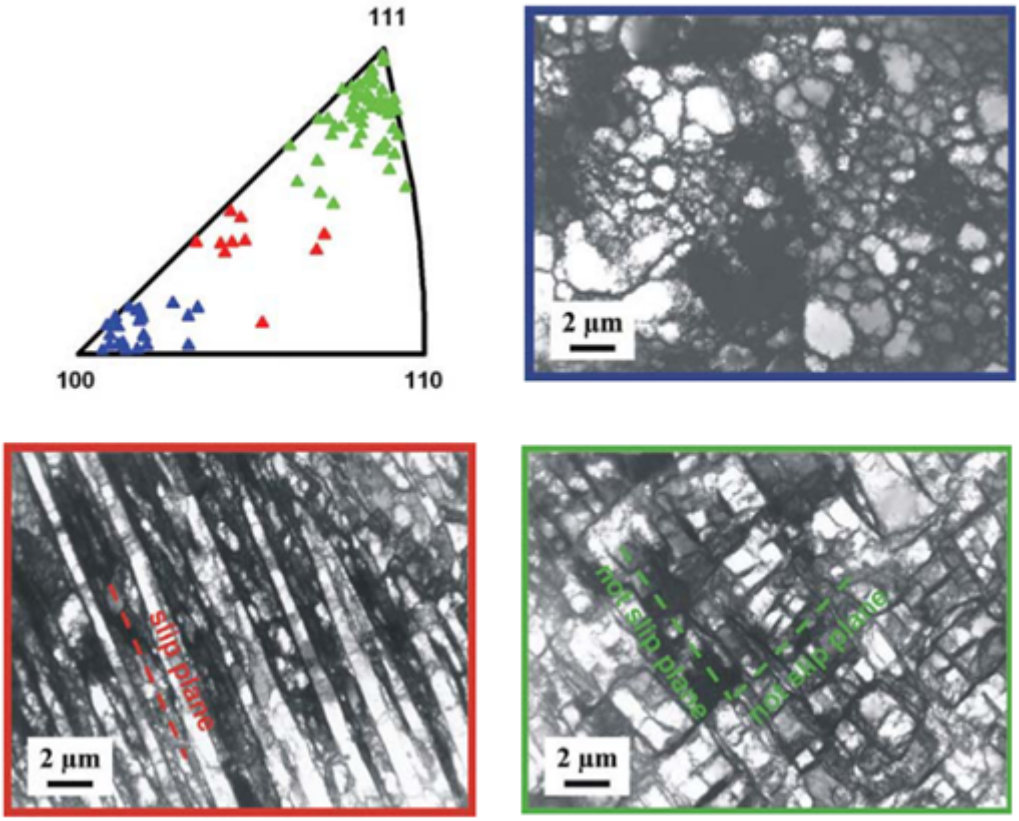

Figure 1.11 – *Different types of dislocation arrangements forming in a tensile strained Aluminium. The boundary type is strongly dependent on the orientation of the grain with respect to the tensile axis. Crystallographic boundaries form in red-marked grains. Non crystallographic boundaries are detected in grains near the 111 pole of the stereographic triangle. Finally, incidental dislocation boundaries are observed in grains near the 001 pole [18].*

The accurate prediction of the plane of a GNB is only possible by TEM [19]. Tilting the sample, it is possible to align the beam with two different crystallographic directions for which the boundary trace is narrow and sharp, i. e. the boundary is viewed *edge on*. The boundary plane can be obtained as the cross product of the two observation directions.

The occurrence of the slip-plane-aligned GNBs was found to be strongly dependent on the initial crystallographic orientation of the grain relative to the macroscopic deformation mode [20]. Figure 1.11 shows the grain orientation dependence of dislocation structures formed in a tensile stressed polycrystal of Aluminium. Grains near the 100 pole only form dislocation cells contoured by incidental dislocation boundaries. Geometrically necessary boundaries are present in the rest of the grains, but these lie on different crystallographic planes. In the middle of the triangle, grains have Type 1 crystallographic boundaries, aligned with slip planes, whereas grains near the 111 pole have non crystallographic geometrically necessary boundaries.

GNBs form due to the mutual interactions of different dislocations coming from

different slip systems: the dependence of dislocation structures on grain orientation is therefore interpreted as a dependence on the slip systems. In general, it was found that a GNB aligns with a slip plane if a significant fraction of the total slip amount is concentrated on that plane [21]. Taylor model represents therefore a useful tool that allows to evaluate the slip amount of every slip system, in order to predict the dislocation arrangement in single grains. The problem with the Taylor model is that it has an ambiguity in the selection of the slip systems, i. e. several equivalent but different solutions are predicted. However, it was found that the rotational path of the grains of an Aluminium polycrystal can be satisfactorily predicted by the Taylor model, whose solution is obtained by maximizing the slip amount on the most active slip system [22], as shown in Figure 1.12.

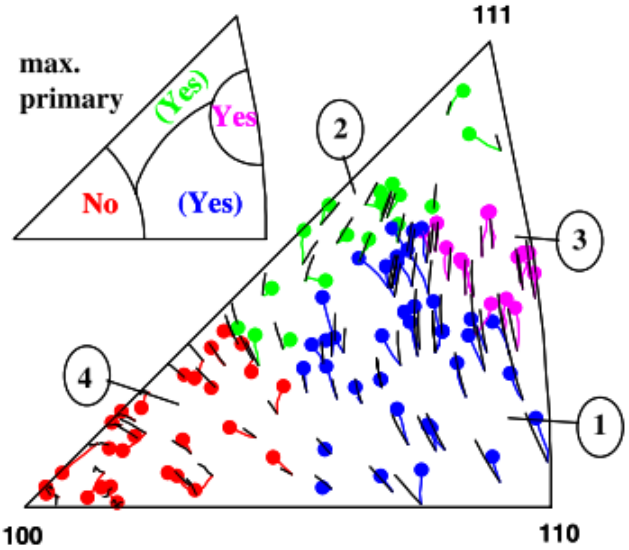

Figure 1.12 – *Comparison between the experimental rotational paths of Aluminium grains and the predictions of the Taylor model (black lines). The solution to the ambiguity problem is the maximization of the slip amount on the most active slip system. The smaller triangle indicates the regions whether the agreement is acceptable or not [22].*

It can be seen that the theoretical model gives some acceptable predictions with the experimental observations in the regions 1, 2, 3 of the stereographic triangle. In the region 4 the theoretical rotations do not match at all the experimental ones, probably due to a simultaneous activity of several slip systems with equivalent slip amounts, that cannot be reproduced by the Taylor model. This phenomenon should be linked to the presence of incidental dislocation boundaries in these grains, but further work is necessary to understand the reasons of the lack of GNBs in grains near the 100 pole.

The dislocation content of deformation induced geometrically necessary boundaries was widely explored in the literature [23, 24]. In particular, Hong et al. [25] carried out a TEM-based characterization of the dislocation content of GNBs forming in a cold rolled Aluminium. The authors assumed that only dislocations with

Burgers vector of type $\frac{1}{2}\langle 110\rangle$ compose the boundary. The choice of the diffraction vectors for the correct execution of the observation is crucial. In this regard, the *invisibility criterion* coats a significant importance. It states that when the diffraction vector $\vec{g}$ and the Burgers vector $\vec{b}$ of a dislocation are perpendicular, the beam is not deviated by the dislocation displacement field, and the defect is *out of contrast* or invisible:

$$\vec{g} \cdot \vec{b} = 0 \tag{1.13}$$

This way, the Burgers vector of a dislocation is defined by the cross product between two diffraction vectors $\vec{g_1}$ and $\vec{g_2}$ that fulfils the Equation 1.13.

$$\vec{b} = \vec{g_1} \times \vec{g_2} \tag{1.14}$$

The dislocation content of dislocation walls can be fully described by tilting the thin foil inside the TEM. Figure 1.14 shows typical weak beam images of a geometrically necessary boundary using three different diffraction vectors. The Burgers vector of the visible dislocations corresponding to the actual value of diffraction vectors are shown as full lines, following the colour code defined in Figure 1.13. Dashed lines represent invisible dislocation lines. Figure 1.14(d) shows the entire network, with the typical hexagonal and rectangular dislocations configuration within it.

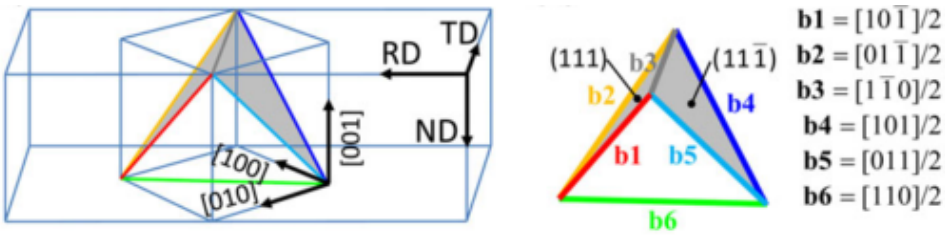

Figure 1.13 – *Rolling geometry of the sample. Slip planes of the coplanar slip systems predicted active are coloured grey. The scheme on the right shows the Burgers vectors of dislocations which are supposed to form the boundaries [25].*

Two main types of dislocation networks were identified: *(a)* An hexagonal path composed of three sets of dislocations. Two of these have Burgers vector coming from the slip systems which are expected to be active. The third is attributed to dislocation reactions. *(b)* The other configuration is dominated by two sets of straight parallel dislocations which cross each other to form a rectangular network.

McCabe et al. [23] characterized the dislocation content of a single slip-plane-aligned GNB in a near-Brass-oriented grain of a rolled copper polycrystal. In this study, the boundary dislocations were also found to originate from active slip systems, but dislocation reactions forming *Lomer locks* were also observed. Anyway, the experimentally observed dislocation content of the boundary does not match with the predictions of the low-energy-configurations theoretical models, i. e. the *Frank*

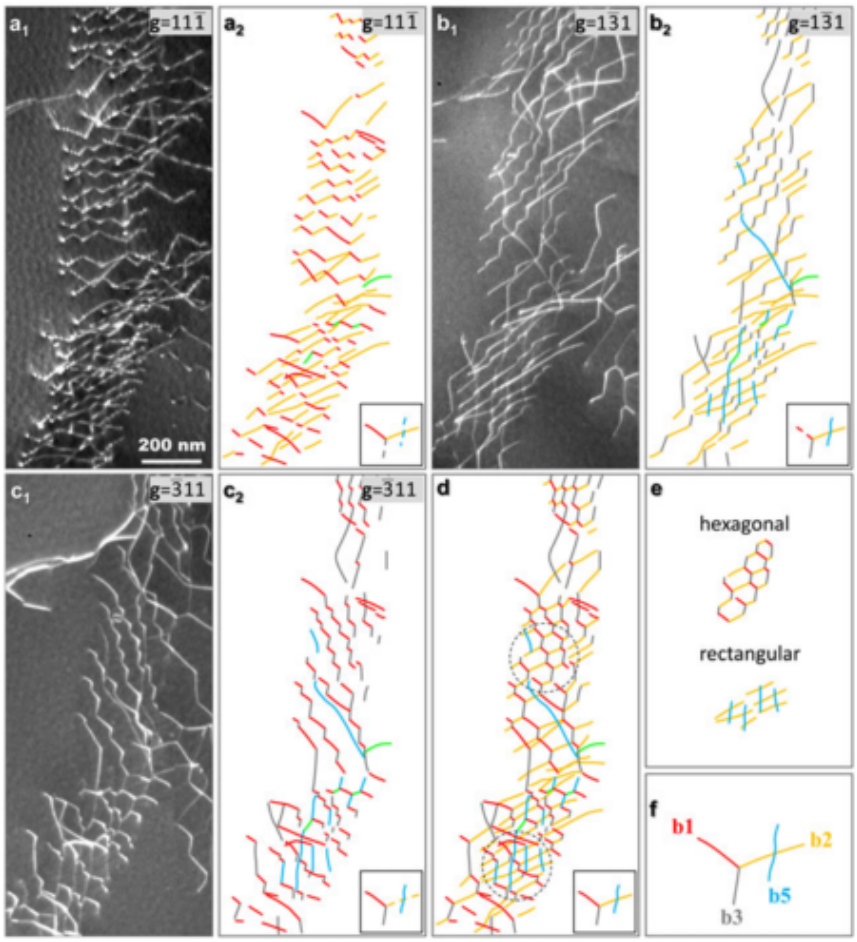

Figure 1.14 – *Determination of the dislocation content of a geometrically necessary boundary using three different diffraction vectors* $\vec{g_1} = [11\bar{1}]$, $\vec{g_2} = [1\bar{3}1]$ *and* $\vec{g_3} = [\bar{3}11]$. *The lower right insets indicate the Burgers vectors of dislocations, where full lines indicate visible dislocations and the dashed lines the invisible ones. (e) Two main dislocation networks in the boundary [25].*

formula. Further work is therefore necessary to build a theoretical model being able to predict the dislocation content of geometrically necessary boundaries forming in grains with different initial orientations.

1.3.2 X-Ray line profile analysis

Real materials are not ideal and perfectly ordered single crystals; they contains lattice defects such as grain boundaries, dislocations, stacking faults,vacancies or interstitial atoms. In the previous section, we saw that materials microstructure can be directly investigated by Transmission Electron Microscopy, nevertheless the oldest technique of characterization is represented by X-Ray Diffraction (XRD). The analysis of peak shape provides indirect information about the microstructure, and then the parameters and the defect structures are extracted from the broadening and the shape of peak profiles.

The procedure of evaluation of peak profiles for the characterization of the mi-

crostructure is referred to as *X-Ray Line Profile Analysis*. From a theoretical point of view, the intensity distribution of a large free-of-defects crystal is similar to a Dirac δ function, as pointed out by Warren [26]. X-Ray diffraction peak profiles may broaden due to the small crystallite size, dislocations, planar defects (stacking faults and planar boundaries) and/or chemical inhomogeneities [27]. The intensity distribution scattered around a diffraction vector $\vec{g}$ in the reciprocal space is three dimensional, as indicated by the contour lines in Figure 1.15.

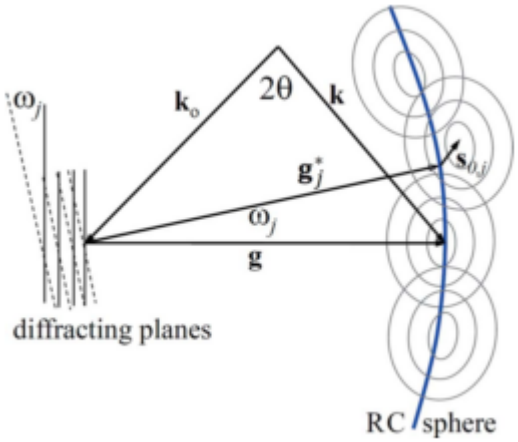

Figure 1.15 – *Schematic X-Ray scattered intensity distribution around a fundamental Bragg reflection defined by the diffraction vector $\vec{g}$ in the reciprocal space. $\overrightarrow{k_D}$ and $\overrightarrow{k_0}$ are the diffracted and the incident wavevectors, respectively, and 2θ is the diffraction angle. Two sets of diffracting planes (indicate as solid and dashed lines) are rotated by a rocking angle ω_j. The corresponding diffraction vectors are denoted as $\vec{g}$ and $\vec{g}_j^{\,*}$. The intensity distribution caused by such rotated planes lies on the rocking curve sphere with radius equal to $|\,\vec{g}\,|$, indicated by a solid blue line. [28].*

The local changes of lattice plane spacing causes a broadening of the intensity distribution along a direction that is parallel to $\vec{g}$. Local lattice rotations and tilts cause a broadening along a sphere with radius $|\,\vec{g}\,|$, which is called *rocking curve sphere*. Summarizing, broadening along a direction parallel to $\vec{g}$ is denoted as *radial broadening* or *line broadening*, while broadening in the perpendicular directions is called *azimuthal broadening* or *rocking curve*. Generally, real crystals may generate anisotropic peak broadening around a fundamental Bragg reflection [29], and rocking curve broadening is much larger than radial broadening. A theoretical description of the peak broadening induced by dislocation walls was provided by Wilkens [30] and compared to the Warren-Averbach method [26]. Experimental line broadening essentially depends on the simultaneous action of two factors, e. g. the so called *particle size* broadening related to the small size of the coherent volume and the *strain broadening* related to the strain/stress field of crystal defects. The Warren-Averbach method allows to analyse the influence of these two mechanisms separately. The scattered intensity I as a function of the radial coordinate q in the reciprocal space can be described by the Equation 1.15

$$\mathrm{q} = \frac{2(\sin\theta - \sin\theta_0)}{\lambda} \tag{1.15}$$

where θ_0 is the Bragg angle of the perfect reference lattice and λ is the X-Rays wavelength. The intensity distribution can be normalized according to Equation 1.16, and represented by means of its Fourier transform A(L) (Equation 1.17).

$$\int \mathrm{I(q)dq} = 1 \tag{1.16}$$

$$\mathrm{A(L)} = \int \mathrm{I(q)exp(-2\pi iqL)dq} \tag{1.17}$$

L is a distance vector which can be parallel (L>0) or antiparallel (L<0) to the diffraction vector $\vec{g}$ associated with the reflecting lattice planes. According to the Warren-Averbach model, Equation 1.17 can be expressed in the form:

$$\mathrm{A(L)} = \int \exp 2\pi \mathrm{i}\,\vec{g} \cdot [\vec{R}(\vec{r} + \vec{L}) - \vec{R}(\vec{r})] \tag{1.18}$$

where $\vec{R}$ is the displacement field vector. This expression can be now factorized as [26]:

$$\mathrm{A_n(L)} = \mathrm{A^P(L)A_n{}^s(L)} \tag{1.19}$$

where the subscript n indicates the order of the Bragg reflection. $A^{\mathrm{P}}(L)$ denotes the component of the Fourier transform given by the particle size, and it does not depend on the diffraction vector order, whereas $A_n{}^{\mathrm{s}}(L)$ is the strain broadening effect, which can be approximated as:

$$\mathrm{A_n{}^s(L)} = \exp(-2(\pi \mid \vec{g} \mid \mathrm{L})^2\langle\varepsilon_{\mathrm{L}}^2\rangle) \tag{1.20}$$

where $\langle\varepsilon_L^2\rangle$ is called *mean square strain*, averaged in the reference volume. Finally, if the total Fourier transform is calculated for at least two orders of Bragg reflection. it is possible to analyse separately the two effects given by the strain broadening and the particle size, according to Equations 1.20 and 1.19.

$$\ln(\mathrm{A_1(L)}) - \ln(\mathrm{A_2(L)}) = 6(\pi \mid \vec{g_1} \mid \mathrm{L})^2\langle\varepsilon_{\mathrm{L}}^2\rangle \tag{1.21}$$

$$4\ln(\mathrm{A_1(L)}) - \ln(\mathrm{A_2(L)}) = 3\ln(\mathrm{A^P(L)}) \tag{1.22}$$

The Warren-Averbach method can be applied in order to calculate the X-Ray intensity distribution caused by the presence of dislocation arrangements or *small angle boundaries*, provided that the displacement field is known.

In his analysis, Wilkens considered an elastically isotropic and infinitely extended

crystal, in which small angle boundaries are placed perpendicular to the x direction of the reference coordinate system, at a distance D from each other. Such boundaries are composed of edge dislocations, whose Burgers vector is parallel to the x axis, as well as the diffraction vector $\vec{g}$. Within a small angle boundary, the distance between to consecutive edge dislocations is denoted by d. Figure 1.16 shows the considered dislocation configuration.

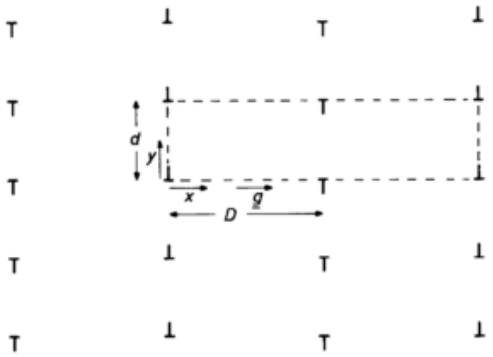

Figure 1.16 – *Schematic view of the dislocation arrangement considered by Wilkens [30].*

At all (x,y) points, the displacement field can be calculated as the sum of the contribution of all dislocations in the reference volume element. The Fourier transform, as defined by Equation 1.18 can be calculated for two orders of $\vec{g}$ pointing along the same direction according to Equations 1.22 and 1.21, providing the "apparent" values of $A^{\mathrm{P}}(L)_a$ and $\langle\varepsilon_L^2\rangle_a$. The first term was compared to the correct value $A^{\mathrm{P}}(L)_c$ (see Figure 1.17); if the small angle boundary acts as true particle boundary, this value is equal to

$$\mathrm{A^P(L)_c} = 1 - \frac{|\mathrm{L}|}{\mathrm{D}} \tag{1.23}$$

Figure 1.17 shows the plot of the apparent and correct particle size coefficients for different values of D/d. With increasing values of D/d, the slope of $A^{\mathrm{P}}(L)_a$ reveals an extended linear slope, and the tendency is closer to the one predicted by the Warren-Averbach model.

The extrapolation of the linear slope down to the abscissa provides the apparent particle size $\bar{L}_a$ that can be compared to the correct value $\bar{L}_a = D$. The ratio between these two quantities is close to 1 for D/d = 10, but it increases with decreasing values of D/d. This means that the measured particle size is close to the real one when the distance between dislocation walls is at least 10 times higher than the distance between to adjacent dislocations within the wall. All curves show a negative curvature for small L (*hook effect*) which is in contradiction with the Warren-Averbach analysis. Another disagreement with the model was found by plotting the total Fourier transform $A_n(L)$ with respect to n^2 using L/d as a parameter (Figure 1.18). One would expect the data to lie on a straight line, and the $A^{\mathrm{P}}(L)_c$ value should be

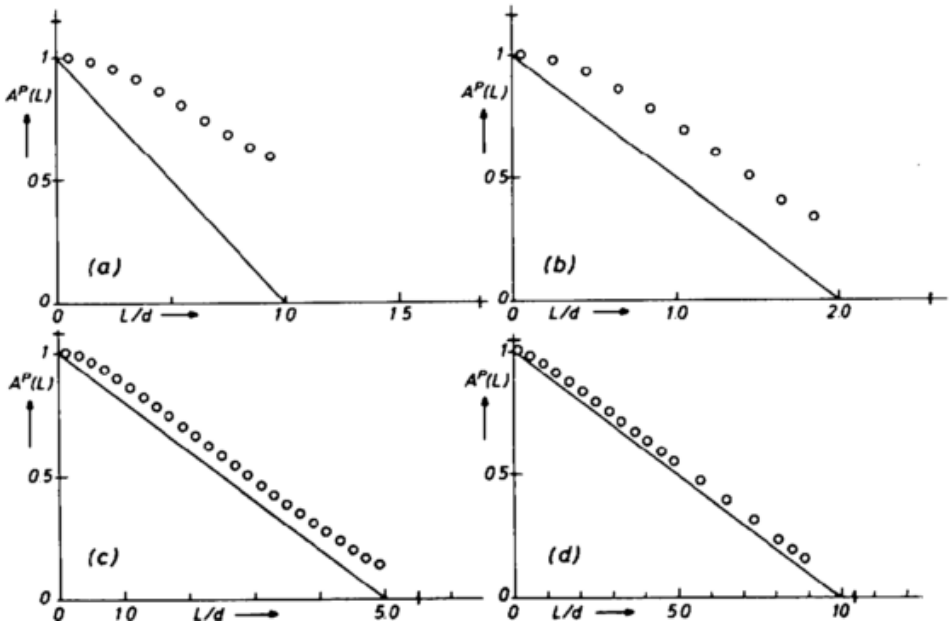

Figure 1.17 – *Plot of the particle size coefficients $A^P(L)_a$ (circles) and $A^P(L)_c$ (solid lines) as a function of L/d for different values of D/d. (a) D/d = 1 (b) D/d = 2 (c) D/d = 5 and (d) D/d = 10 [30].*

defined by the intercept between the linear slope and the ordinate axis, but this is far to be the case.

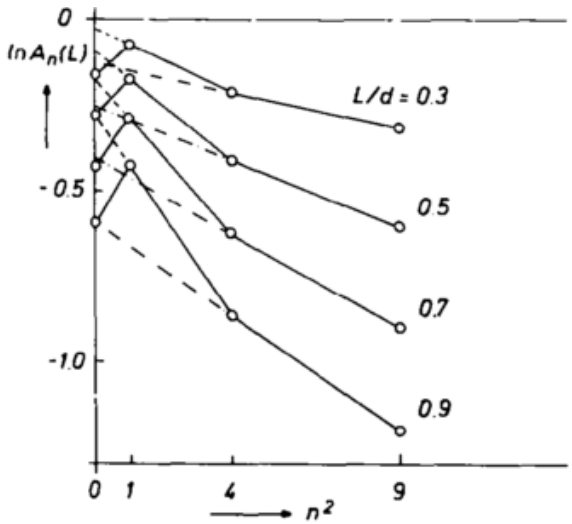

Figure 1.18 – *Plot of the Fourier transform of the scattered intensity distribution evaluated for D/d = 2, as a function of n^2, with L/d as parameter. Data do not lie on a straight line, in contradiction with the Warren-Averbach model [30].*

X-Ray line profile analysis was widely used in the literature for the microstructural characterization of plastically deformed metals. Borbely et al. [31] proposed a method providing the evaluation of the average particle size and of the average total dislocation density from experimentally measured X-Ray diffraction peaks. The line profiles can be represented in terms of the second and fourth order moments, which are dependent on q:

$$M_2(q) = \frac{q}{\pi^2 \varepsilon_F} - \frac{L}{4\pi^2 K^2 \varepsilon_F^2} + \frac{\Lambda(\rho)\ln(q/q_0)}{2\pi^2} \tag{1.24}$$

$$\frac{M_4(q)}{q^2} = \frac{q}{3\pi^2 \varepsilon_F} + \frac{\Lambda(\rho)}{4\pi^2} + \frac{3\Lambda(\rho)}{(2\pi)^2 q \varepsilon_F}\ln(q/q_1) + \frac{3\Lambda^2\langle\rho^2\rangle}{4\pi^4 q^2}\ln^2(q/q_2) \tag{1.25}$$

These equations show that both moments are dependent on the particle size ε_F and the total dislocation density ρ.

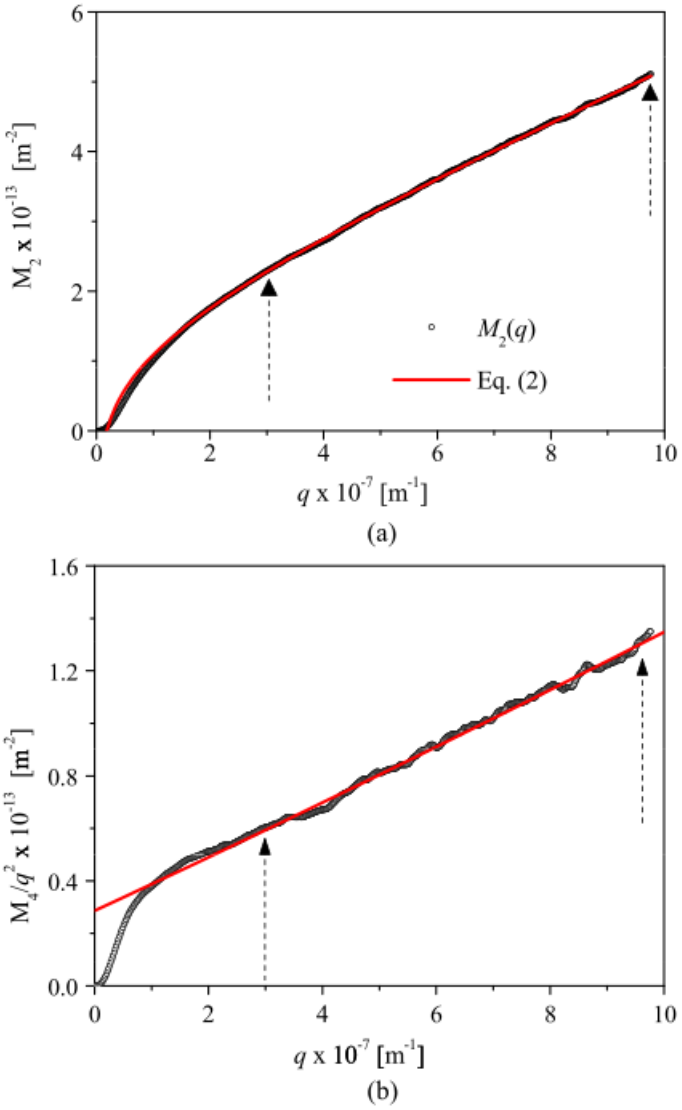

Figure 1.19 – *Plots of (a) second order moment and (b) fourth order moment of a X-Ray diffraction peak for a deformed copper (epsilon = 0.15). Arrows indicate the considered q interval for the fit. [31].*

Figure 1.19 shows the plot of the second and fourth moments calculated for a deformed copper. It is clearly visible that the asymptotic behaviour of the curves is linear with q. ε_F and ρ can be easily calculated resolving a system of two equations. The moments method is able to provide the average total dislocation density within

the grains of a polycrystal.

1.3.3 Rocking curves

Mughrabi and Obst [32] proposed an interesting analysis that provides the density of those dislocations which are responsible of intra-grain misorientations, hence geometrically necessary. Before that, only the lower and the upper limit values of ρ_{GND} could be calculated [33]. Combining the geometrical parameters of two kinds of low angle grain boundaries (of tilt and twist character) with mechanical constants of the material, the authors found an analytical relation which links the *full width at half maximum* (FWHM) of rocking curves $\beta_{1/2}$, the ratio between the geometrically necessary dislocation density and the total dislocation density ρ_{GND}/ρ and the resolved shear stress acting on the most stressed slip system τ:

$$\beta_{1/2} = 0.0169 \frac{\rho_{\mathrm{GND}}}{\rho} \tau \tag{1.26}$$

$$\beta_{1/2} = 0.00189 \frac{\rho_{\mathrm{GND}}}{\rho} \tau \tag{1.27}$$

Equation 1.26 is referred to tilt boundaries, with a misorientation axis of $\langle 121 \rangle$ type, while Equation 1.27 describes a pure twist boundary, with a $\langle 121 \rangle$ misorientation axis. The constant value depends on the mechanical features of the material, such as the Young modulus, and the modulus of dislocation Burgers vector. An interesting tendency was found between the resolved shear stress and several values of rocking curve broadening measured for copper single crystals (Figure 1.20).

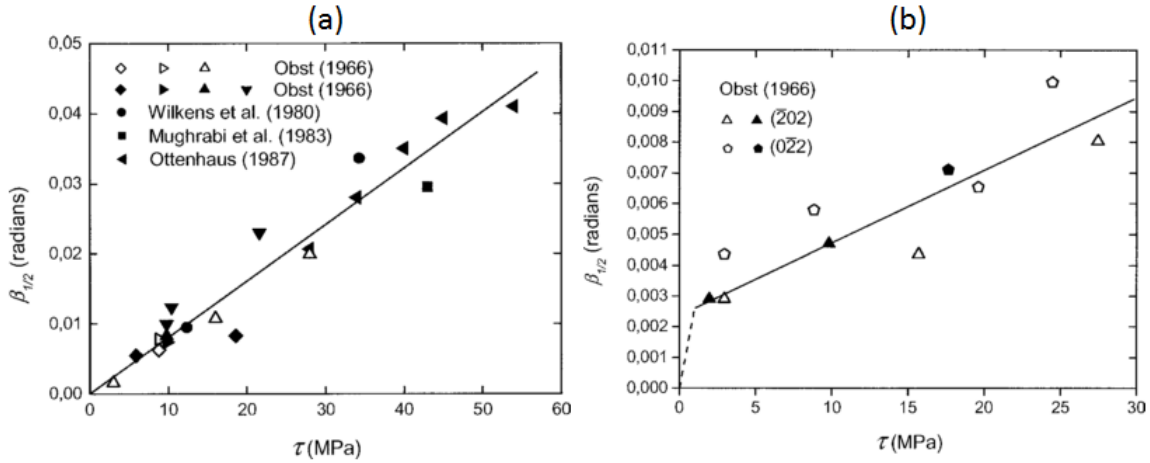

Figure 1.20 – *Half widths $\beta_{1/2}$ of X-Ray rocking curves referred to (a) tilt misorientations and (b) twist misorientations measured on copper single crystals. The dashed line indicates the sudden increase of $\beta_{1/2}$ at low resolved shear stresses [32].*

The relation between $\beta_{1/2}$ and τ is well approximated by a straight line, this means that the increase of the ratio ρ_{GND}/ρ is constant and it is independent of

the resolved shear stress. The combination between the experimental line equation with Equations 1.26 and 1.27 makes possible the evaluation of ρ_{GND}/ρ for the two types of boundaries. The authors found that geometrically necessary dislocations are only a small percentage of the total dislocation density (about 10%). The non-zero intercept on the ordinate axis of Figure 1.27(b) can be explained by imagining a sudden increase of the GND density during the transition between stage I and stage II work-hardening of copper single crystals, which well corresponds to a stress value of about 3 MPa.

Recently, Barabash and co-workers [34] modelled the three-dimensional intensity profile around a reciprocal lattice site, scattered by a deformed crystal. They found that the lattice rotations caused by simple dislocation arrangements, such as *tilt boundaries* arising at low strains, produces a spread of the diffracted intensity around the reciprocal lattice point. The azimuthal projection of the resulting anisotropic intensity distribution is generally close to that of a Gaussian function, and presents a pronounced broadening along a particular crystallographic direction $\vec{h}$, that is perpendicular both to the direction of the diffraction vector $\vec{H}$ and to the misorientation axis of the boundary $\vec{\omega}_a$:

$$\vec{h} = \vec{H} \times \vec{\omega}_{\mathrm{a}} \tag{1.28}$$

Different reflections scattered from the same grain containing a tilt boundary present different broadening. The invisibility criterion states that reflections with diffraction vector perpendicular to the Burgers vector of the dislocations forming the boundary should have a circular isotropic shape, whose broadening is only due to the geometry of the detector (instrumental broadening). It is important to emphasize that this model reproduces well the the azimuthal projection of the scattered intensity distribution from grains containing boundaries with one type of dislocations. Pantleon et al. [35] proposed a model for boundaries containing two types of dislocations.

1.4 Dislocations behaviour near a grain boundary

It is known that grain boundaries at low temperature, act as strong obstacles to further movement of the dislocations, leading to an improvement of the mechanical behaviour of the material (*work hardening*). When the temperature and/or stress increases, dislocations can be incorporated into the boundary, and the lattice dislocation has to interact with the pre-existing dislocation network. Three types of dislocation reactions were observed: *combination*, *dissociation* and *transmission* to another grain [6].

1.4.1 Interactions between dislocations and grain boundaries

Combination with a boundary dislocation

A lattice dislocation with a Burgers vector $\overrightarrow{b_m}$ can react with an *intrinsic* dislocation $\overrightarrow{b_i}$ placed within the boundary, to produce an *extrinsic* dislocation $\overrightarrow{b_e}$ which will be incorporated to the boundary. Practically, this kind of reaction is energetically favourable only for low-angle boundaries with a misorientation angle of less than 10°, where the Burgers vectors of boundary dislocations are very close to that of the incoming lattice dislocation. In an ideal case, the lattice dislocation can be incorporated into the boundary without any reaction if the two types of dislocations have the same Burgers vector.

Dissociation

The lattice dislocation can be absorbed by the grain boundary by means of a decomposition process, where the initial dislocation is splitted into a glissile and sessile dislocations with smaller Burgers vectors. The geometrical features of the resulting dislocations are not casual: they have to be coherent with the DSC lattice of one of the two misoriented regions. Again, this process is energetically favourable for low angle boundaries; for high angle boundaries this phenomenon can take place at high temperatures [6].

Transmission

The last mechanism of interaction between lattice dislocations and grain boundaries occurs by transmission of the whole dislocation or of one of its decomposition products into the neighbouring crystal. This phenomenon strongly depends on the grain boundary geometry. The so-called *direct transmission* imposes that the trace of the two slip planes from each side of the boundary are almost common in the boundary plane, and that the resolved shear stress on the transmitted dislocation line are important. These conditions make that the direct transmission mechanism takes places very rarely. On the other side, dislocations can pass through a boundary interface by *indirect transmission*. This is the case when the segments of the dislocation network forming the boundary act as Frank-Read sources of dislocations, even at relatively low values of the shear stress. Another example of indirect transmission is the dislocation nucleation from a grain boundary, which is driven by the high stress field induced by the presence of *dislocation pile-ups*.

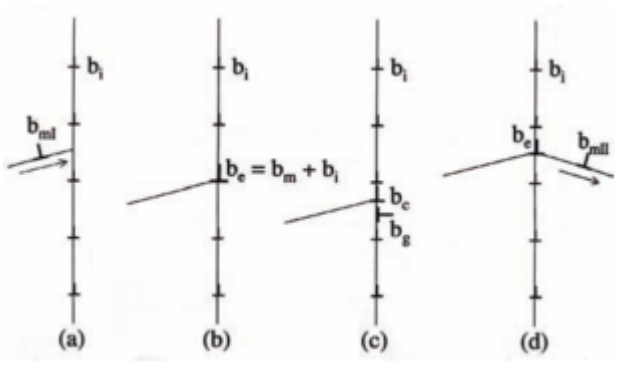

Figure 1.21 – *The most important mechanisms of interaction between a lattice dislocation and a grain boundary:(a) the grain boundary acts as a barrier, obstructing further dislocation movement (b) combination with an intrinsic dislocation (c) dissociation in two dislocations (d) transmission to the neighbouring grain [36].*

1.4.2 Dislocation pile-ups

When the interaction between dislocations and grain boundaries is not energetically favourable, dislocations tend to accumulate near the interface forming ordered arrays such as dislocation pile-ups, that were often observed in plastically deformed materials at low temperatures (see Figure 1.22).

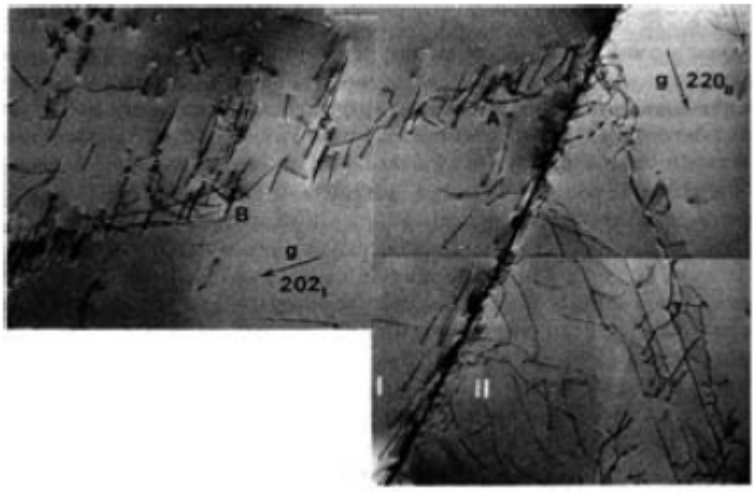

Figure 1.22 – *Transmission Electron Microscope image of a dislocation pile-up in the vicinity of a grain boundary [37].*

Consider a source which emits n edge dislocations, all belonging to the same slip system, under an applied resolved shear stress τ (Figure 1.23); the leading dislocation can meet a barrier impeding any further movement, such as a grain boundary or a sessile Lomer lock dislocation network. Dislocations are expected to pile-up against the barrier because they cannot combine, being of the same sign. The leading dislocation experiences a backward force due to the presence of the obstacle τ_b and a forward force τ_f being the sum of the applied resolved shear stress and the repulsive force induced by the dislocations behind it. In equilibrium, the two forces

must be equal to:

$$\tau_b = \tau_f = n\tau \tag{1.29}$$

Thus, the stress at the head of the pile-up, e. i. near the barrier, is magnified to n times the applied shear stress. Unlike low-angle boundaries, dislocation pile-ups produce long-range stress field. At grain boundaries, this can cause local yielding, dislocation nucleations or cracks nucleation and propagation. Most of the pile-ups are made up of edge dislocations, since screw dislocations can cross slip out of the slip plane.

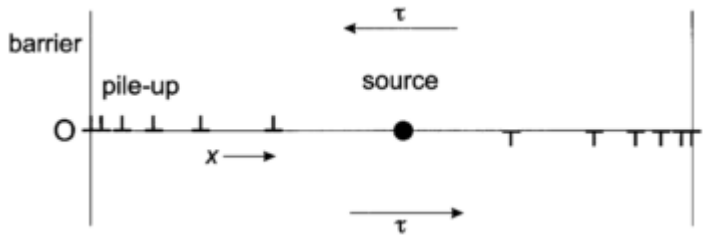

Figure 1.23 – *Schematic view of a dislocation pile-up: the source emits edge dislocations of the same sign, all lying on the same slip plane, under an applied shear stress* τ

1.5 Grain subdivision

Plastic deformation of polycrystals causes the onset of orientation gradients within single grains and the development of deformation textures. In particular, recrystallized grains do not rotate uniformly, but subdivide into portions separated by geometrically necessary dislocations, with local orientation changes within the original grain boundaries. This phenomenon was widely studied during the last decades, often mentioned as *grain subdivision* or *grain fragmentation* [38, 39]. Many experimental studies were carried out, mainly using TEM [40, 41] and via the analysis of back scattered Kikuchi patterns or EBSD [42–44].

The first application of the EBSD technique was presented by Skjervold et al. [45], who studied the orientation gradients which form in an Aluminium polycrystal subjected to axisymmetric compression. Continuous line scans were performed on characteristic regions of the polycrystalline sample, measuring the misorientation angle from a reference position. In this case, since the rotation axis remains nearly stationary, the measured misorientation corresponds to the true misorientation. It was found that orientation gradients do not develop randomly in single grains: these misorientations preferentially appear in constrained regions such as triple junctions and grain boundaries.

A parallel approach of investigation is represented by the plastic deformation of crystalline aggregates. Beaudoin et al. [38] used a model to study the deformation

of one grain embedded in a second grain: they observed the formation of different orientation domains in the embedded grain, that was interpreted as an evidence that crystal orientation evolution is strongly affected by grain neighbourhood. Raabe et al. [39] pointed out that crystal subdivision depends much more on the initial orientation of the grain than on the orientation of neighbouring crystals. Recently, Toth et al. [46] developed a model that does account for grain subdivision in considering grain size, misorientation distribution and strain hardening. The basic hypothesis is that the rigid rotation of crystallographic planes is more difficult near grain boundaries, so that the lattice rotation is different than in grain interior. As a consequence, the distorted lattice plane is expected to have a near S-shape, more distorted near grain boundaries, as illustrated in Fig. 1.24.

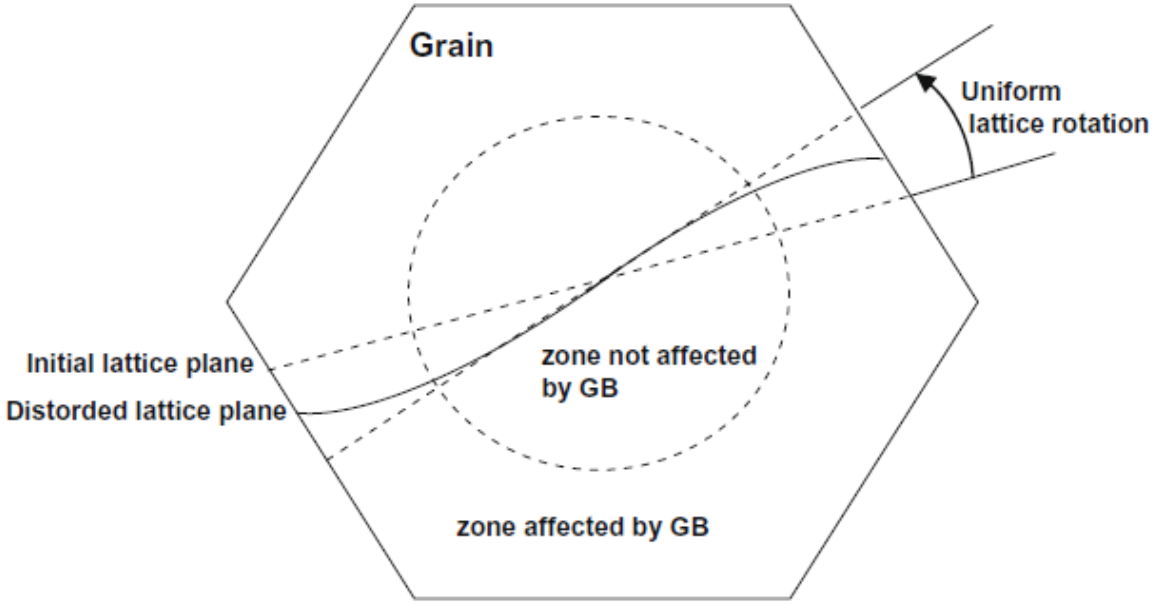

Figure 1.24 – *Lattice plane distortion in a deformed grain. Lattice curvature is higher near grain boundaries than in the interior, as hypothesized by Toth et al. [46]*

1.6 Conclusions

The comprehension of dislocations interaction mechanisms is essential to understand the theory of the formation of geometrically necessary boundaries within single grains of plastically deformed polycrystals. These structures are responsible for work-hardening, due to their obstruction to the free movement of lattice dislocations. For this reason, the investigation of such dislocation arrangements recovered a great scientific interest in the last decades. The standard characterization method is based on Transmission Electron Microscopy, providing a direct observation of the dislocation content of the wall, as well as a good identification of the boundary plane. X-Ray Diffraction techniques were also widely used, in order to calculate the geometrically

necessary dislocation density within deformed crystals.

Nevertheless, both techniques have some disadvantages, restricting the investigation field. X-Rays give averaged results over a relatively large region. TEM needs thin foils to carry out the observation, hence samples must be destroyed and the characterization is performed *post-mortem*. In this thesis, we propose new XRD methods (based on Three Dimensional X-Ray Diffraction and K-map techniques), allowing to follow in situ the evolution of deformation induced dislocation structures. Some results were cross checked by EBSD.

2 Experimental techniques for the characterization of dislocation structures

Contents

This chapter is dedicated to the description of the main experimental techniques that were used for our study. In the first part, we focus on Three Dimensional X-Ray Diffraction (3DXRD), which allowed the characterization of deformation induced misorientations in single grains of an Al 0.1 %wt Mn polycrystal, and their *in situ* evolution under the application of a macroscopic tensile stress (Chapter 3). The second part is dedicated to the description of grains indexing procedure starting from the analysis of diffraction spots, performed by means of the ImageD11 software [47], developed at the ID11 beamline of the European Synchrotron Radiation Facility (ESRF). The application of the EBSD technique for cross checking 3DXRD results is described. This tool was also used to study the deformation mechanisms within grains near grain boundaries (Chapter 4). Finally, we present the basic setup of the K-map technique, that was applied to evaluate lattice tilts and intragranular strain within a grain of the deformed polycrystal.

2.1 The material

The presented methodology was applied to study lattice misorientation evolution during uniaxial straining of an Al-0.1%Mn alloy. The reason behind this choice is that this alloy is easily deformable, with a typical FCC structure and a high *stacking*

fault energy; this means that Shockley partial dislocations do not form, that makes our interpretation of the results in terms of the predictions of a Taylor type crystal plasticity more simple. Moreover this material was widely used within our research group, particularly for studies regarding recovery and recrystallization.

The material was prepared by recrystallizing at 500 °C for 9 minutes a cold rolled specimen with reduction of 90% in thickness. The resulting grain size and intragranular orientation spread were characterized by EBSD in a JEOL JSM 6500F scanning electron microscope. Recrystallization resulted equiaxed grains with an average grain size of about 100 μm, and mean intragranular misorientation smaller than 1 degree in 99.3% of the grains. Such microstructure ensures that the observed misorientation spreads are only caused by deformation. The resulting grain size allows to carry out the analysis over a good number of diffracting grains with different average orientations.

In order to choose the strain levels for the 3DXRD in situ analysis, a standard dog-bone specimen with a transverse section of 20 X 4 mm^2 was deformed to obtain the stress-strain response of the recrystallized material. A tensile test was therefore carried out in our laboratory. The recrystallized material has a yield strength of 11 MPa (at $\epsilon = 0.2\%$) and shows a good ductile behaviour (see Figure 2.1).

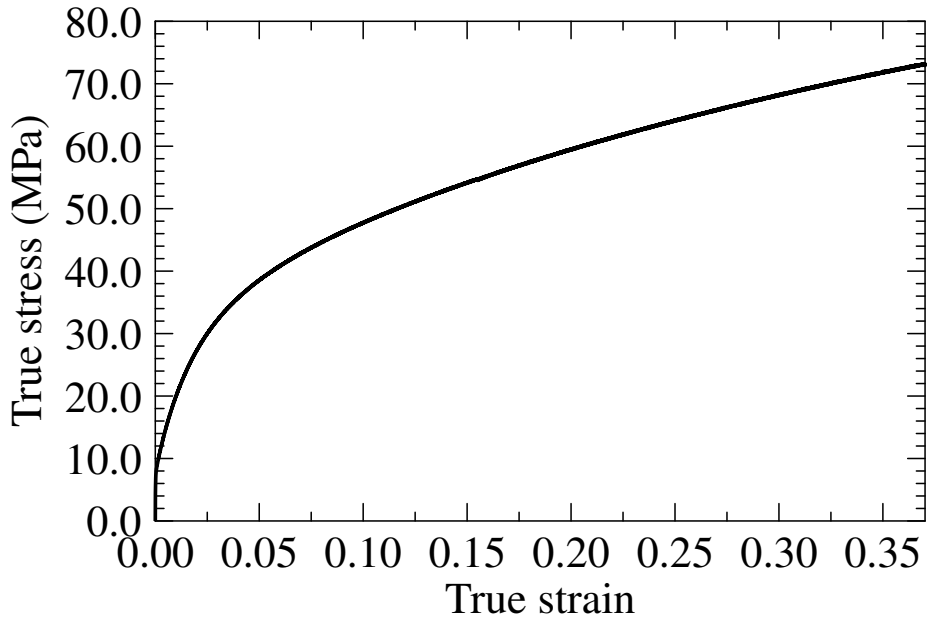

Figure 2.1 – *True stress - True strain curve of the recrystallized Al 0.1%wt Mn, with a mean grain size of 100 μm. The yield strength evaluated for a strain $\epsilon = 0.2\%$ is about 11 MPa.*

2.2 The 3DXRD technique

In this section we provide the basic setup of the 3DXRD technique used for our characterization at the ID11 beamline of the European Synchrotron Radiation Facility (ESRF) in Grenoble. A bibliographic review of the 3DXRD based experiments carried out in the last years is also presented. For more details about the technique, the reader is invited to consult the book of H. F. Poulsen [48].

2.2.1 Basics of the 3DXRD technique

The 3DXRD method can be seen as an extension of the rotation method, well known from single crystal crystallography. The basic set-up is shown in Fig. 2.2 and 2.3.

A dog-bone specimen is mounted in a Nanox tensile machine, working under force control (see Fig. 2.4). The macroscopic displacement can be applied on the sample by screwing an endless screw. The device allows measuring at the same time the corresponding applied force thanks to a piezoelectric load cell.

Such system is mounted on a ω rotation stage and centred at the origin of the *laboratory coordinate system xyz*, so that the specimen tensile axis coincides with the rotation axis z. As an option, x-, y- and z- translations can be added, as well as additional rotations. The specimen is illuminated by a monochromatic X-Ray beam, whose direction is perpendicular to the rotation axis z. A perfect Si monocrystal is used as monochromator, that can be oriented with respect to the direction of the incoming beam, in order to provide an X-Ray beam with the desired wavelength.

The beam is focused in order to illuminate a suitable cross-section of the specimen. The cross section of the incident beam can be varied, depending on the type of experiment that one wants to perform. There are three main configurations:

- *pencil beam*: the beam is confined to a circular shape, typically with a diameter of 5 μm. Such reduced size is particularly useful in the case of single grains analysis of materials with small grain size. To probe the entire cross section of the specimen, a 3D scan is required over y, z and ω.
- *line beam*: the beam has a rectangular shape, very thin in the z direction (typically 1 μm $\times$ 1 mm), providing a complete characterization of the illuminated layer. For three-dimensional scans, a set of layers must be analysed by displacing the sample in the z direction.
- *wide beam*: beam cross section is square (up to 1 mm $\times$ 1 mm). In this case, an ω-scan is able to provide a full 3D characterization of the illuminated volume.

The beam penetrates the entire sample, so diffraction occurs from all cells/subgrains/grains inside the illuminated gauge volume which fulfils the Bragg condition.

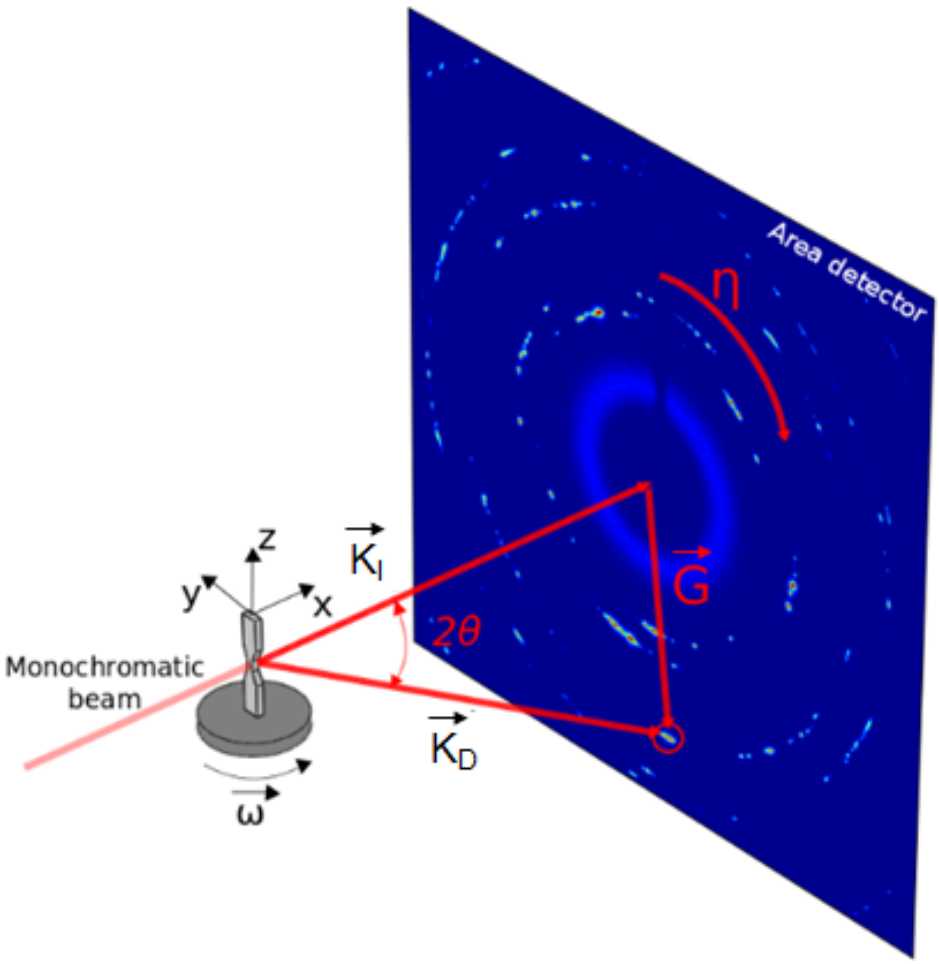

Figure 2.2 – *Sketch of the 3DXRD setup for the case of an incoming monochromatic X-Ray beam. The Bragg angle 2θ, the rotation angle ω and the azimuthal angle η are indicated, as well as the laboratory coordinate system centred on the sample. Diffraction spots coming from different grains of the polycrystalline sample appear onto the 2D detector, arranged along the Debye-Scherrer rings.*

In 1913, W. L. Bragg found a simple relation that states that a monochromatic X-Ray beam, with wavelength λ, hitting a crystalline sample, causes the diffraction of the hkl planes, if the Eq. 2.1 is satisfied:

$$2 \cdot \mathrm{d_{hkl}} \cdot \sin(\theta) = \mathrm{n}\lambda \tag{2.1}$$

where d_{hkl} is the distance between the hkl lattice planes, θ is the diffraction angle and n is the diffraction order, as schematically showed in Fig. 2.5.

Just behind the specimen, a FreLon 21 detector is placed, composed of 2048 X 2048 pixels whose size is 47 μm. Lattice planes which actually are under diffraction conditions generate a diffracted beam, at an angle of 2θ from the incident beam direction. This creates a *diffraction spot* on the 2D detector. The position of diffraction spots are unambiguously determined by the Bragg angle 2θ and the *azimuthal angle* η, that is measured starting from the top of the detector. By convention, the

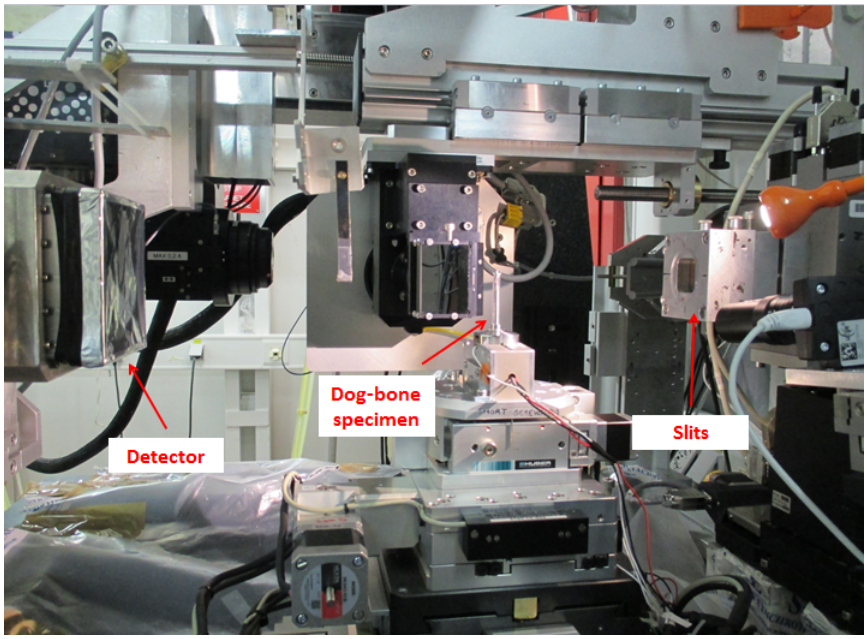

Figure 2.3 – *Experimental configuration of the 3DXRD microscope. The specimen is mounted into the tensile machine that is placed on the ω-stage. A 2D detector collects the diffraction spots produced by the diffraction of the monochromatic incoming beam.*

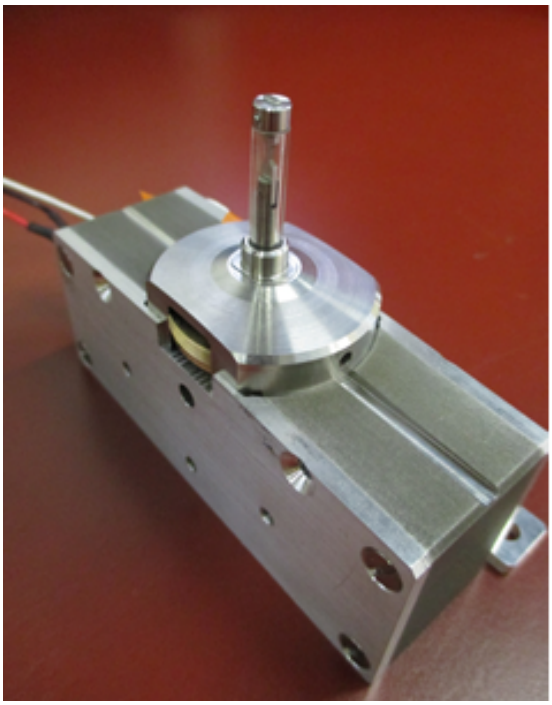

Figure 2.4 – *Uniaxial tensile machine used for the in-situ tensile experiment at the ID11 beamline of the ESRF ([49]).*

clockwise direction is set as the positive direction in this work.

In order to scan the complete structure, and not just the part that actually fulfils the diffraction condition, the sample is rotated around the z axis. Hence, many exposures are carried out for a certain ω range, with an angular interval of $\Delta\omega$. After a complete scan, the specimen is deformed by the application of the macroscopic

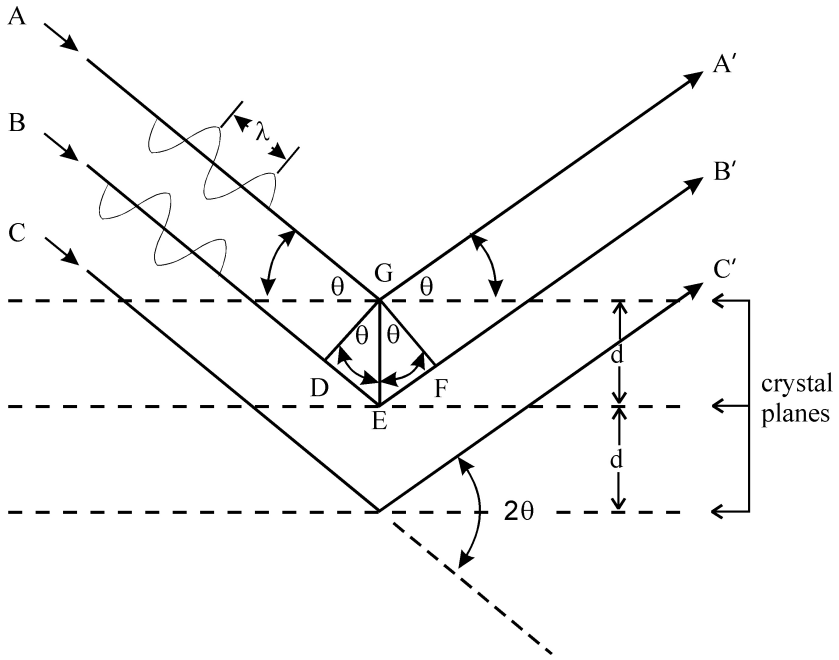

Figure 2.5 – *Schematic representation of the Bragg law. The line DEF indicates the difference between the optical paths of the waves A and B: if this quantity equals the wavelength of the monochromatic beam, the interference is constructive with the rise of the diffraction phenomenon.*

tensile stress, and another scan can be made over the same volume, in order to study the appearance and/or the evolution of dislocation structures within the same grains.

2.2.2 Crystal plasticity studies by 3DXRD

The development of the 3DXRD opened new insights for the non-destructive characterization of engineering materials. 3DXRD microscope was used for a wide range of applications, including grain rotations during deformation, recovery and recrystallization kinetics of single grains, phase transformation and subgrain dynamics. The most common approach is the measurement of the change of diffraction spots intensity and shape, while exposing the sample to stimuli such as stress and/or temperature.

When plastic deformation occurs, single grains experience a crystallographic rotation with respect to the sample coordinate system. Moreover, the activation of the most stressed slip systems gives rise to the nucleation and the multiplication of dislocations: their arrangement in dislocation boundaries becomes responsible for the local rotation of the crystal lattice, subdividing the original grains.

3DXRD allows the determination of the experimental rotation path of single grains of a polycrystal in-situ under the application of a macroscopic tensile stress (see Fig. 1.12). Experimental results obtained for an Aluminium specimen were compared to the predictions of the theoretical models proposed by Sachs [50] and Taylor [51]. Despite of the ambiguity problem, the Taylor model provides the best match with

the experimental results: nevertheless, the predicted rotations are often smaller than the real ones, especially for those grains whose average orientation is close to the 101 pole of the stereographic triangle. Nevertheless, grains near the 001 pole and close to the line 001-111 of the pole figure show an experimental behaviour that cannot be predicted by neither of those models which actually are available in the literature, so further work is still necessary to fully understand the deformation mechanisms of single grains.

A first attempt in this direction was made by Oddershede et al. [52], by analysing the projection onto the ω-η plane of a set of diffraction spots coming from three grains with initial tensile axes near <522> direction. Even if they have close initial orientations, these grains show a completely different rotational paths after the application of a macroscopic stress. Experimental results were compared to simulated diffraction spots, as illustrated in Fig. 2.6, by changing the amount of slip of the most activated slip systems. It was found that these grains experience a high variation of the relative slip activity that cannot depend only on their crystallographic orientation, and must be attributed to grain interactions.

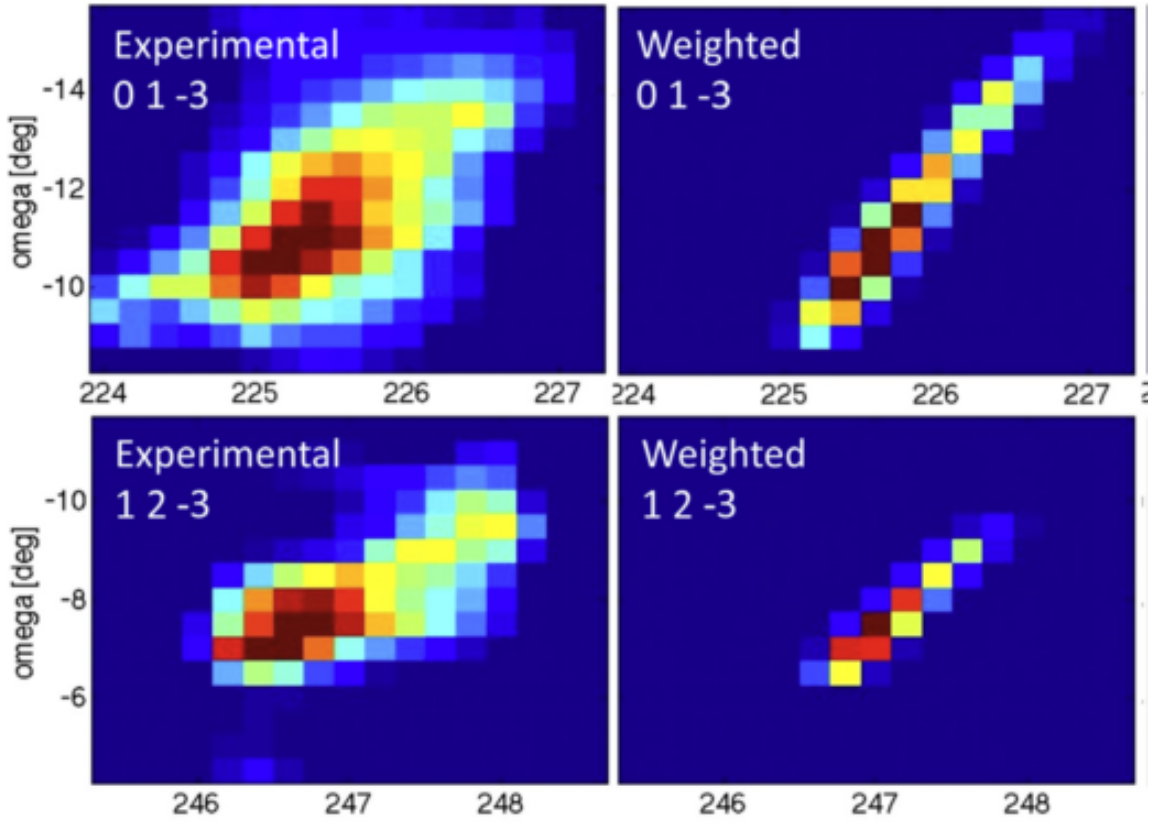

Figure 2.6 – *Comparison between experimental and simulated diffraction spots coming from an IF steel after 9% tensile deformation. The intensity of the reflections is integrated over 2θ and projected onto the ω-η plane [52].*

It is well known that plastic deformation bends the crystal, causing a spread of the diffraction vector distribution whether it is illuminated by a X-Ray beam. This

phenomenon is reflected on the observation of the broadening of diffraction spots along both ω and η directions. Consequently, spots projection onto the ω-η plane provides a direct information about crystals bending or splitting. Poulsen et al. [53] measured the rocking curves of 88 diffraction spots coming from an Aluminium specimen after 4% tensile deformation. The obtained FWHM distribution matched very well with the misorientation angles across dislocation boundaries obtained by TEM on the same material.

2.3 The experimental setup

2.3.1 Sample preparation

The tailored microstructure of the material is very important for the success of the experiment. The grain size should be large enough in order to avoid the overlap of diffraction spots coming from different grains onto the detector. Moreover, since we were interested in the study of the dislocation walls induced by a tensile deformation, the original microstructure should have very low intragranular misorientation gradients, that ensures the absence of pre-existing geometrically necessary boundaries.

The recrystallization treatment described in Section 2.1 was performed on a cold-rolled sample, with a final thickness of 3 mm. A flat dog-bone specimen with cross section of 1 X 1 mm and 14 mm in gauge length was prepared by spark erosion of the raw sample. Finally, a low-voltage electrolytic polishing was carried out on the specimen, in order to eliminate any eventual damage produced at its outer surface.

2.3.2 Test parameters

A good choice of the test parameters (X-Ray wavelength, detector distance etc.) is crucial to ensure the correct proceeding of the experiment. The intensity of diffraction spots plays a very important role for the correct post-treatment of the experimental data: it is well known that the intensity is proportional to the grain volume, hence the X-Ray beam energy should be high enough to reduce the absorption [54, 55]. On the other hand, a low energy leads to a better resolution and contrast, but the diffracted intensity will be low, due to the absorption coefficient of the material. Considering the specimen thickness and the absorption coefficient for Aluminium, a good compromise was found by setting the X-Ray energy to 60 keV, which corresponds to a wavelength $\lambda = 0.2072$ Å. In order to probe as many grains as possible within the gauge section at the same time, a wide beam was used, whose cross-section was 1 X 0.2 mm.

The following step was the choice of the distance between the specimen and the

two-dimensional detector. A large distance means that diffraction spots cover a larger number of pixels onto the detector, improving the angular resolution. On the other hand, this restricts the number of diffraction rings which can be analysed, since the diffraction cones of higher order can pass out of the detector perimeter. In order to have as many diffraction spots as possible, we calculated the radius of diffraction rings by means of the Bragg law (Eq. 2.1), fixing the specimen-detector distance to 257 mm, so as the 420 ring is visible at the corners of the detector.

The specimen was rotated over a complete ω turn, using an integration step size $\Delta\omega = 0.06°$, resulting in a total of 6000 diffraction images per scan. This represents a good compromise between the angular resolution of the rocking curves and the time duration of the acquisition.

Four scans were performed, corresponding to four strain levels in the plastic domain of the material, plus a reference scan at the undeformed state. The first two scans were made at zero load and at the yield stress ($\approx 11MPa$), respectively. Diffraction spots of single grains could be identified and followed through the other deformation states corresponding to the stress levels of 20, 30 and 41 MPa. Basd on the stress-strain curve of Fig. 2.7, these correspond to strain levels of $\epsilon = 1\%$, $\epsilon = 3\%$ and $\epsilon = 6.6\%$.

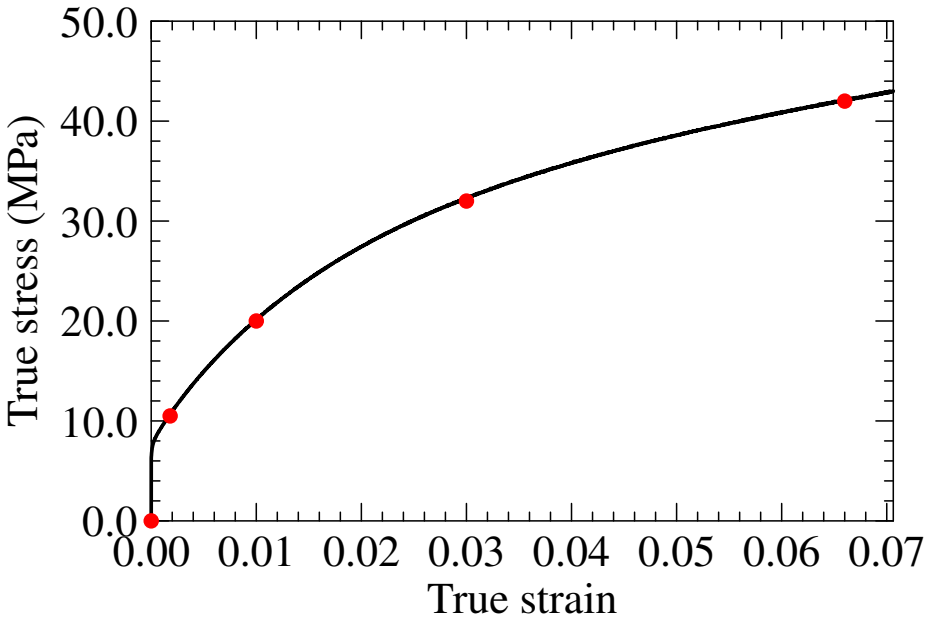

Figure 2.7 – *Macroscopic stress levels applied onto the specimen, indicated by the red dots onto the stress-strain curve. These correspond to the strain levels* $\epsilon = 0\%$, $\epsilon = 0.2\%$, $\epsilon = 1\%$, $\epsilon = 3\%$, *and* $\epsilon = 6.6\%$.

2.4 The ImageD11 software

The data provided by a 3DXRD experiment consist of a number of diffraction frame images. An extensive data analysis is required in order to extract the desired information from these.

In this work, the software ImageD11 [47], developed at the ESRF, was used for setup calibration, peak searching and grain mapping. Some of the main packages used in our data analysis are described below.

2.4.1 Peak searching and setup calibration

ImageD11 allows to find all individual diffraction spots (i.e. peaksearching) through several diffraction frames above a given threshold; the output is a text file that contains all spots whose intensity is higher than the threshold. At this stage, the coordinates (2θ,η) of the diffraction spots on the detector are affected by calibration errors: one expects all spots with the same hkl indices to fall onto rings which have the same 2θ values, but this is not the case, as shown in Fig. 2.8(a). This is due to the unavoidable discrepancies between the ideal and the real experimental conditions. ImageD11 takes into account such difference, performing a calibration of the setup configuration, by means of an iterative optimization of the parameters listed below.

- χ: rotation angle of the ω axis (the z-axis of the laboratory coordinate system) around the beam, that should be zero in ideal conditions.
- *sample-detector distance*: the exact value of the distance between the specimen and the area detector.
- *detector tilts*: the tilts of the detector plane compared to the beam direction.
- *wavelength*: the exact value of the X-Ray beam wavelength.
- *Wedge*: angle between the Oz axis perpendicular to the X-Ray beam and the ω axis.
- *beam center*: beam position in the slow and fast pixel directions.

The calibration procedure provides the correct position of the diffraction spots on the detector. Fig. 2.8(b) shows the $(2\theta, \eta)$ plot of the diffraction rings, which appear as vertical lines.

2.4.2 Grain indexing procedure

Starting from diffraction frames, ImageD11 is able to provide a map of diffracting grains in terms of their center of mass position and orientation with respect to the sample coordinate system. By means of this indexing procedure, one associates diffraction spots to grains, making possible a grain-by-grain analysis.

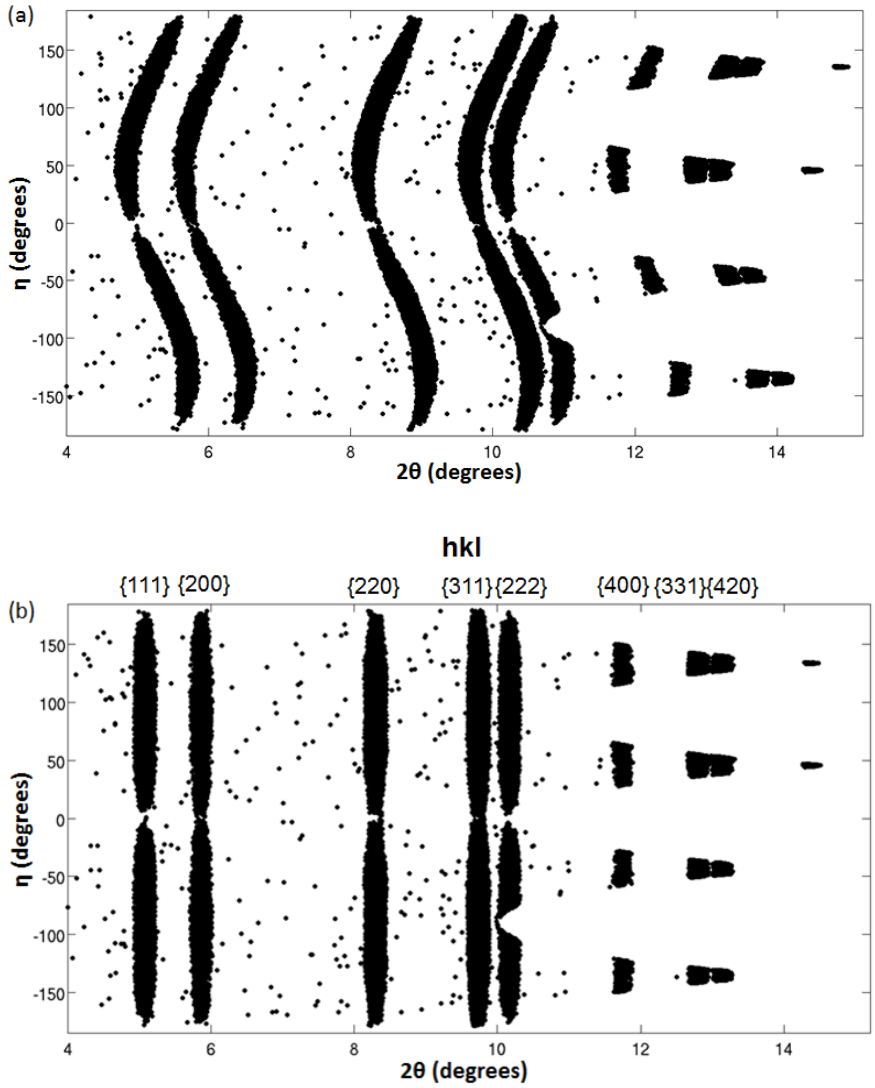

Figure 2.8 – *Comparison between the $(2\theta, \eta)$ plots of the diffraction rings before (a) and after (b) the calibration procedure. The background peaks that do not belong to the rings are not considered for the indexing procedure.*

The task of indexing diffraction data from polycrystalline materials corresponds to assigning a scattering vector to each diffraction spot found in the detector image. First of all, experimental diffraction spots are assigned to hkl rings within a tolerance value. The scattering vectors of two spots belonging to the selected diffraction ring are compared to those expected on the basis of the unit cell and the hkl indices. When the positions of the expected and real spots differ below an appropriate tolerance angle, the corresponding scattering vectors are used to compute an orientation matrix, which is then refined.

The choice of the tolerance angle is crucial: this value should be large enough to accept a correct peak, but small enough to discard a peak that is accidentally close to the expected position [56]. For each grain, a large number of orientation matrices is produced, retaining those that reproduce at least a given number of experimental diffraction spots, which is defined by the user. In this work, grains were accepted if

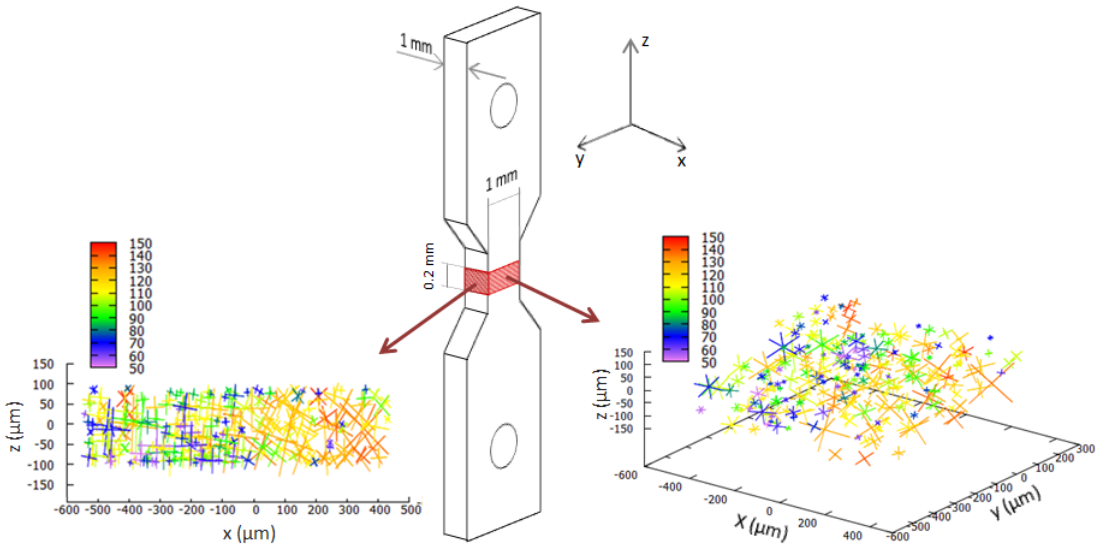

Figure 2.9 – *Results of the indexing procedure performed with ImageD11 software for the strain level ϵ=0.2%. A good reproduction of the illuminated volume is achieved. The 314 indexed grains are represented as crosses with different orientations with respect to the sample coordinate system. The colorbar shows the number of diffraction spots which were found belonging to each grain.*

they indexed at least 50 spots, and the tolerance angle was set to 1.5 degrees.

ImageD11 returns two output files:

- a list of diffraction spots appearing on the detector during the scan. For each peak, the software provides its integrated intensity value, its position in terms of $2\theta, \eta, \omega$ angles, its hkl indices and the corresponding scattering grain identified by an ID number.
- a list of indexed grains and the corresponding centre-of-mass position with respect to the laboratory coordinate system, as well as their orientation matrices.

Fig. 2.9 shows the grain map obtained for the specimen deformed at $\epsilon = 0.2\%$.

2.5 The EBSD technique

The EBSD technique provides a map of the grains at the surface of the sample, via their crystallographic orientations. In this section, we describe the physical principles of this technique and the experimental protocol used in this work.

2.5.1 Physical principle

The discovery of the fundamental diffraction phenomenon on which the EBSD technique is based can be traced back to the work of Kikuchi in 1928. Hereafter, the EBSD method showed a continuous development, and was completely automatized thanks to the production of the SEM.

The EBSD is based on the study of backscattered electrons and their diffraction after the interaction between the incident electron beam and the crystal lattice, forming *Kikuchi patterns* and allowing the determination of grains orientation. The sample surface is tilted, usually at 70°, with regard to the beam direction, in order to increase the rate of backscattered electrons of about 2.5 times. As in the case of X-Ray diffraction, the electrons diffract following the Bragg's law (Eq. 2.1). Because the electrons are scattered elastically in all directions, the diffracted electrons will form a cone, called *Kossel cone*,whose semi-apex angle is $90° - \theta_B$ and its axis blends with the normal of the hkl diffracting plane. The usual values of the wavelength and the diffracting plane distances lead to small values of θ_B, so that the Kossel cones are almost flat and their intersection with the EBSD phosphorus detector screen gives almost straight lines, called *Kikuchi bands*, as shown in Fig. 2.10. The ensemble of such lines forms a *Kikuchi diagram*. The number of the Kikuchi lines forming the diagram depends on the solid angle covered by the camera, that must be close enough to the sample. The analysis of the Kikuchi diagrams provides a full characterisation of the crystalline orientation of the analysed volume.

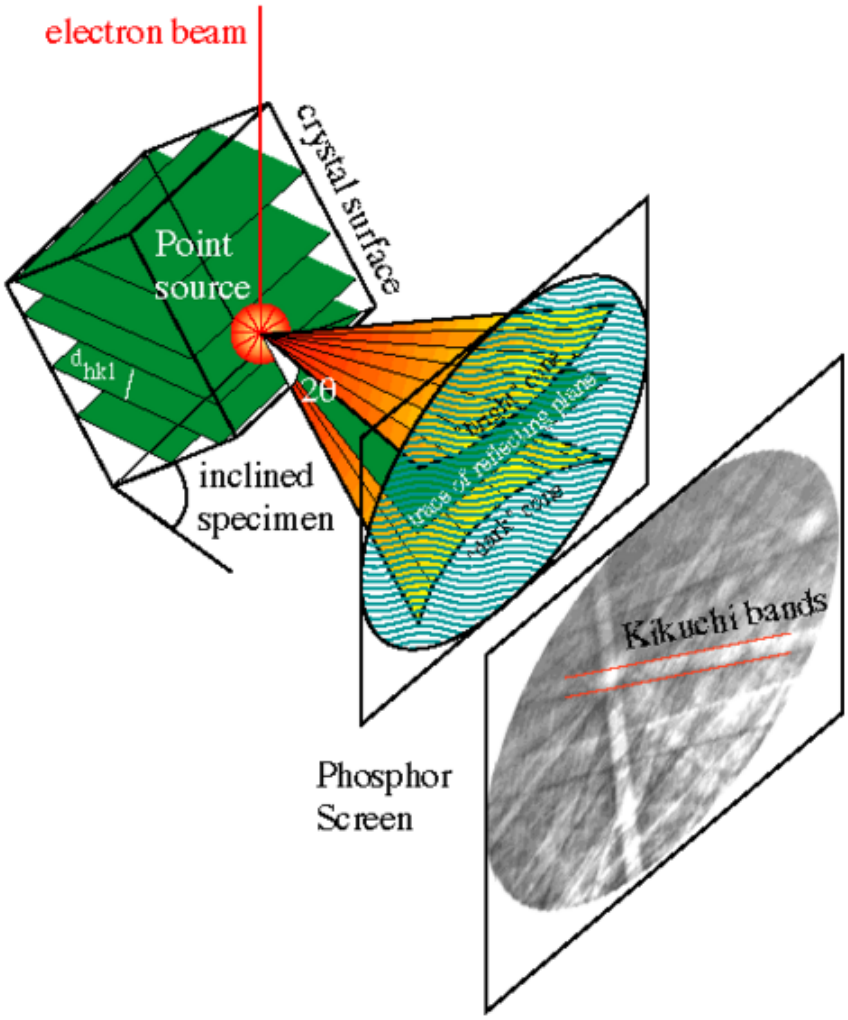

Figure 2.10 – *EBSD method - Formation of a Kikuchi diagram.*

Indexing

The indexing procedure is the determination of the crystalline orientation from the Kikuchi diagrams. The Kikuchi lines are considered as straight, and the Kikuchi diagram is transformed into the *Hough space* (ρ,θ). The *Hough transform* is a technique concerned with the identification of lines in the image. In general, a straight line on the Kikuchi diagram can be represented as a point (ρ,θ) in the Hough space, through the equation:

$$\rho = \mathrm{x} \cdot \cos(\theta) + \mathrm{y} \cdot \sin(\theta) \tag{2.2}$$

where ρ is the distance from the origin to the closest point of the Kikuchi line, and θ is the angle between the x axis with that closest point. This transformation converts each line in the image space into a point in the Hough space.

The intensity of the pixels (ρ_j,θ_j) are augmented by the intensity of the corresponding pixel (x_i,y_i) in the image space. The accumulation of the intensities gives rise to peaks in the Hough space, which correspond to the position of the Kikuchi bands in the image space (Fig. 2.11). The study of their position leads to the determination of the crystalline orientation, provided that the algorithm has information about the crystalline structure. After the indexing, the evaluation software returns an estimation of the error of the orientation calculation (MAD). A small value ensures a good precision of the orientation calculation.

2.5.2 Experimental device

The EBSD system we used for this study, produced by the HKL society, is installed within a ZEISS Scanning Electron Microscope. The acquisition parameters were chosen (Acceleration voltage: 20 kV, Working distance: 15 mm, Diaphragm opening: 6), and the usual optical settings were performed. The backscattered electrons are captured by a phosphorous screen, and the Kikuchi lines are recorded by a CCD camera that sends them to the indexation software. In order to have good quality diagrams, the static background, which is recorded increasing the scanning velocity over an extended area of the sample, is subtracted from the image. With the actual device, we obtained orientation maps of size 1 X 1 mm after about 16 hours, with a step size of 1 μm.

The angular resolution is the most important parameter for our work, since we are interested in studying the intragranular orientation gradients rising during plastic deformation. According to previous works [57], the most reasonable value was 0.4°, which was good enough for the study of grains rotation and fragmentation. Recent developments of the EBSD devices allowed a huge improvement of the angular resolution, which is now close to 0.1°, without any meaningful increase of the acquisition

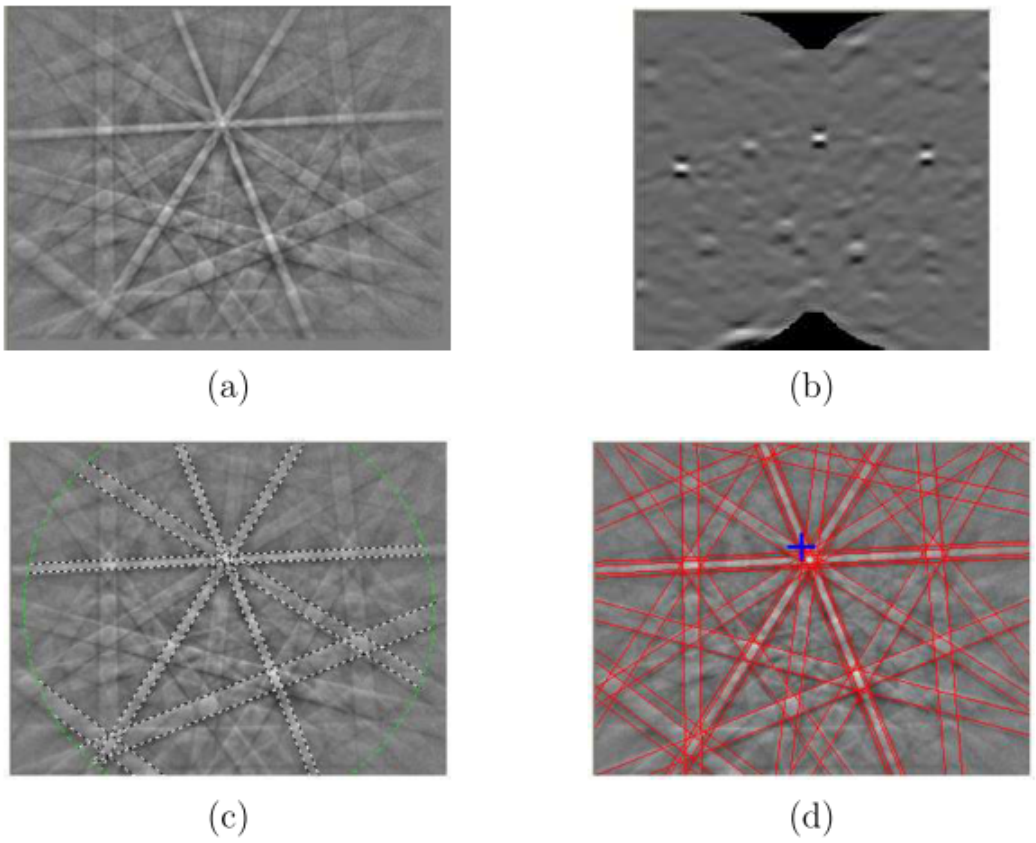

Figure 2.11 – *Determination of an orientation. (a) Kikuchi diagram, (b) Hough transform, (c) Kikuchi bands detection, (d) orientation indexation [57].*

time.

2.5.3 EBSD sample preparation

The choice of the size of the dog-bone specimen substantially depends on the maximum applicable load and the vise width of the tensile machine (see Section 2.5.4). Considering these limitations, a specimen with a transverse section of 3 X 3 mm and a gauge length of 20 mm was cut from a cold rolled sheet: subsequently, the heat treatment described in Section 2.1 was applied, in order to have the same microstructure of the specimen which was analysed by 3DXRD.

Specimens surface must be adequately prepared before the EBSD acquisition: first of all, a mechanical polishing must be carried out. This step is completely manual, rubbing the specimen onto some abrasive papers of different roughness, until reaching a mirror polishing of the surface, with a value of roughness which should be below 1 μm.

The achievement of a good indexing rate for the EBSD analysis requires to perform an electrolytic polishing of the sample surface. Also known as *anodic dissolution*, this technique is probably the best one to polish very soft materials, with the only requirement that specimens must be electrically conductive. Electrolytic polishing

dissolves the higher potential sites of the specimen surface, by smoothing the rough ridges or peaks, making the surface almost planar. Moreover, this technique allows to remove the hardened layer of the sample, caused by the mechanical polishing. This is accomplished by setting the sample surface as anode in an electrolytic cell, as shown in Fig. 2.12.

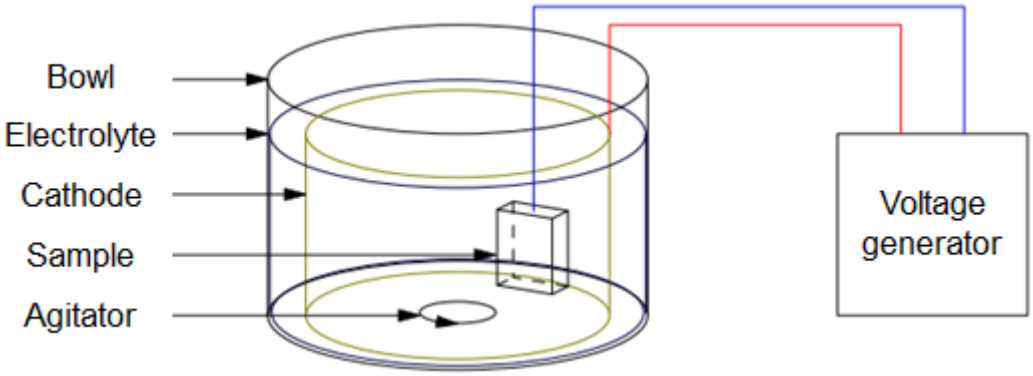

Figure 2.12 – *Sketch of the electropolishing machine. [57].*

A good choice of the electropolishing parameters (voltage, polishing time, temperature) is crucial and the optimal values are different for each material. For this study, for an Al-0.1% Mn, we have chosen a polishing solution A II produced by Struers, the applied voltage was 20 V for 40 seconds, and the temperature was 20°C. The specimen was subsequently rinsed with water and dried on air.

2.5.4 Ex-situ tensile test

The analysis of grain subdivision and comparison with the results deriving from the 3DXRD analysis requires the observation by EBSD of grains misorientation evolution under the application of an uniaxial tensile stress. The specimen must be small enough to fit into the SEM chamber, that makes the use of standard dog-bone specimens and tensile machines impossible. For this reason, the specimen was deformed by means of a special tensile machine (Kammrath, showed in Fig. 2.13) normally used for in-situ observations within the SEM, which is able to apply a maximum tensile load of 10 kN. The specimen is fixed to the machine by means of screws, whose thickness is chosen so that the middle plane of the specimen includes the tensile axis. The machine works under displacement control: once the strain rate is imposed (80 μm/s in this work), an endless screw controlled by a step motor allows the displacement of the vises in tension or compression.

A single grain analysis of the onset and the evolution of orientation gradients was carried out, making EBSD cartography of the same grains of different average orientations at the surface of the sample. Three strain levels were chosen: the reference or undeformed state $\varepsilon = 0\%$, $\varepsilon = 1\%$ and $\varepsilon = 5\%$. Since the material is easily

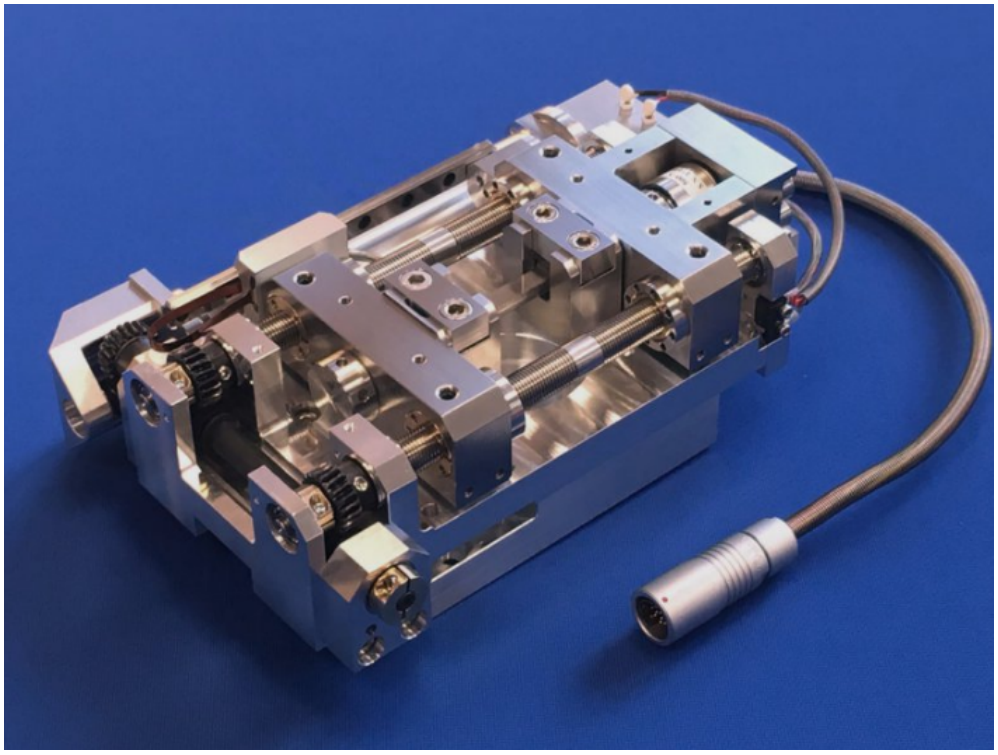

Figure 2.13 – *Tensile/compression module Kammrath, maximum load 10 kN.*

deformable, we decided to make sure that deformation did not occur during fixing the specimen in the machine. Fig. 2.14 shows that the misorientation histograms for the same specimen before and after fixing are similar, excluding any influence of specimen fixing procedure.

2.5.5 Marking of the observed area

The goal of the EBSD analysis was to understand the formation mechanisms and the evolution of intragranular misorientation under the application of a tensile load. For this reason, we needed to mark the observation area, in order to facilitate the grain spotting through different EBSD acquisitions. Such marks were generated by a Vickers microindenter, using a weight of 20 g. A L-shaped grid of 100 μm spaced marks was created on the gauge surface of the specimen, in order to maintain the same orientation of the specimen while putting it into the SEM chamber. All grains being close to the marks are excluded from further analysis, because of the plastic strain field induced by the indentation operation.

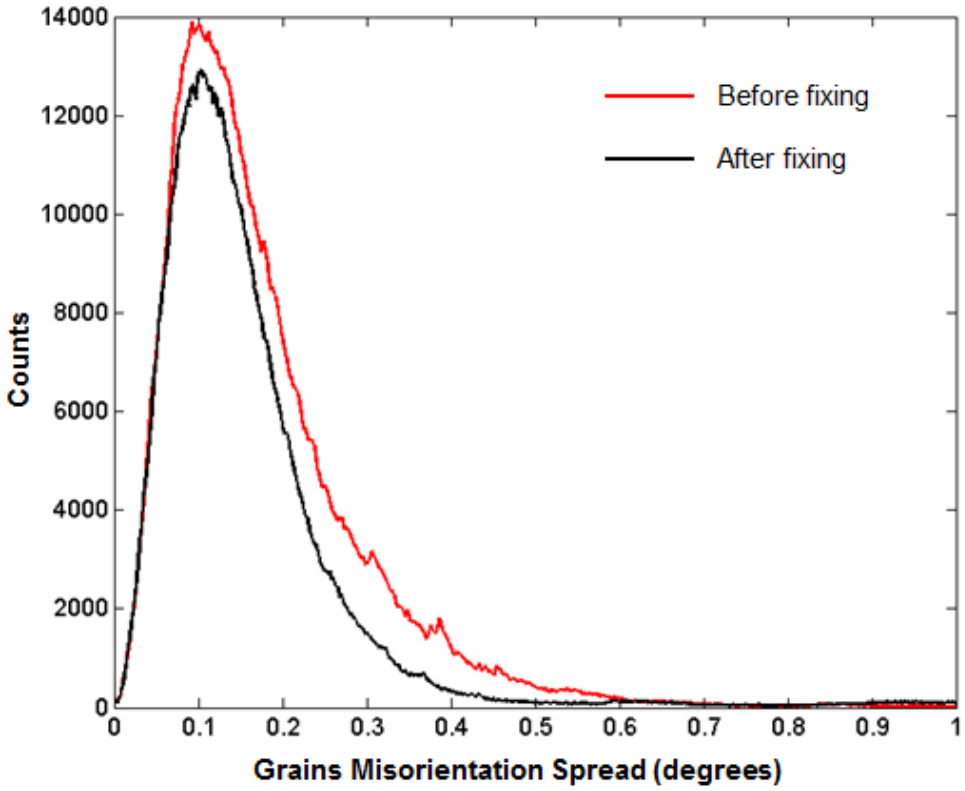

Figure 2.14 – *Grains mean orientation spread histogram of an Al-0.1% Mn specimen before (red curve) and after (black curve) being fixed into the Kammrath tensile machine. The observed area is the same in the two cases. The mounting procedure does not introduce any deformation into the grains, since the modal and the standard deviation of the two curves are within the accuracy of the technique of about 0.4°.*

2.6 The K-map scanning

2.6.1 The experimental setup

In this section, we present the K-map technique developed at the beamline ID01 of the European Syncrothron Radiation Facility (ESRF). The main components of this system are a two-dimensional detector MAXIPIX, with a pixel size of 55 μm, a piezoelectric stage (P-563 PIMars XYZ Piezo System) and a hardware setup (MUSST card) that synchronizes the detector and the scanning stage. The test parameters are defined by the user by means of a *SPEC control program*. The basic set-up is shown in Fig. 2.15 and Fig. 2.16.

Fig. 2.17 is a schematic representation of the whole acquisition process. The SPEC control program prepares the motors controlling the sample stage and the 2D detector to take instructions from the MUSST card, and at the same time sends the acquisition parameters (the scanning points coordinates, the number of points per scan and the acquisition time per point) to the hardware module. When a scanning point (x,y) is localized, the piezoelectric stage sends a signal to the MUSST card that activates the detector, making possible the acquisition of the diffraction frame.

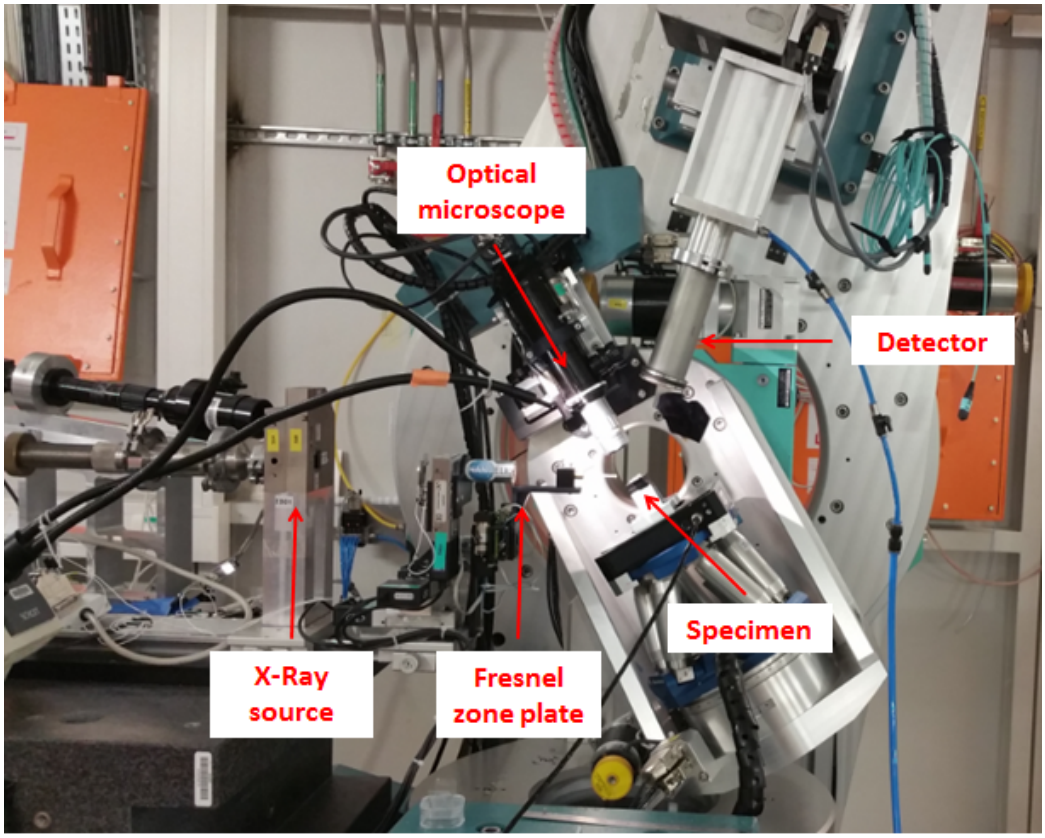

Figure 2.15 – *Experimental setup of the K-map goniometer at the ID01 beamline of the ESRF.*

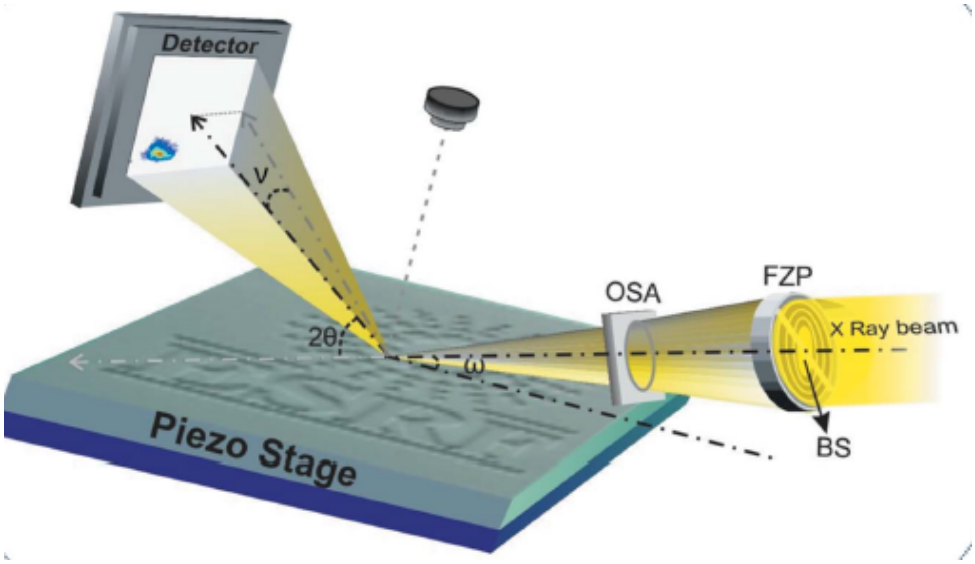

Figure 2.16 – *Sketch of the experimental setup used for the K-map scanning. The X-Ray beam is focused onto the sample, and the rocking angle ω and the scattering angle 2θ are shown. ν is the deviation angle of the signal from the coplanar geometry. A microscope is positioned above the sample [58].*

During the scan, the motor positions and the acquisition time for each scanning point are stored into the MUSST card. Once the region of interest (ROI) is scanned, the acquisition data and the detector images are merged into a *SPECFILE*.

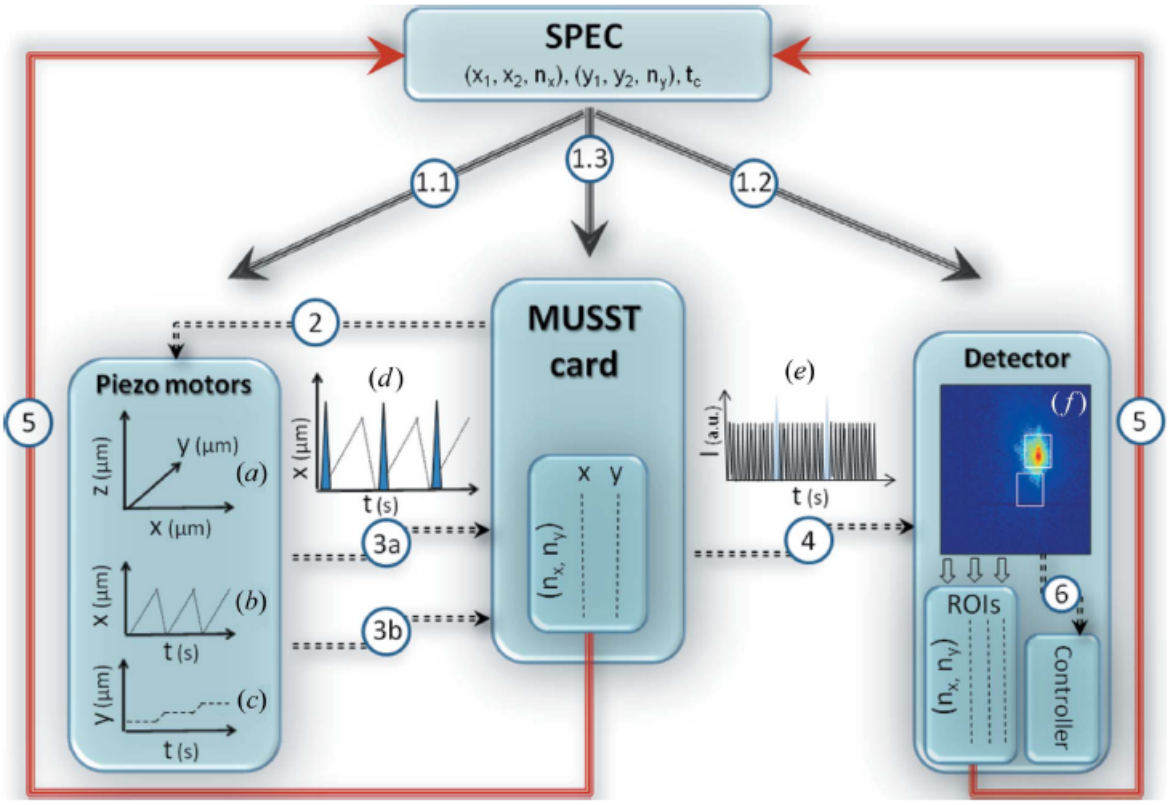

Figure 2.17 – *Schematic representation of the K-map technique [58]. Numbers indicate the operation sequence of the acquisition process.*

The spatial resolution of this technique is defined by the beam size, while the beam divergence controls the resolution in reciprocal space. Using a two-dimensional detector and performing a real space map at every point on a rocking curve, a three dimensional reciprocal space map is obtained for every point of the scanned area. The acquisition procedure leads to five-dimensional data providing information about lattice strains, with a sensitivity below $\Delta d/d = 10^{-5}$, where d is the interplanar distance.

2.6.2 Post-treatment of the detector images

The information about tilts and strain of the scanned area of the sample can be extracted by analysing the acquired images of diffraction peaks at each position of the sample in the reciprocal space.

The software XSOCS (https://sourceforge.net/projects/xsocs/files/), developed at the ESRF, performs this task. The basic operating principle envisages the reading of the specfile in order to extract the motor position (x, y, z, ω, 2θ and η) for each diffraction frame, analysing the Bragg peaks in the reciprocal space. The software converts the scattering angles into reciprocal space coordinates, providing a three-dimensional reciprocal space map at each sample position. To achieve this goal, a preliminary calibration procedure is needed: the user must record the pixel position

corresponding to the origin of the reciprocal space by imaging the direct beam onto the detector. After that, the unit scattering angle corresponding to one pixel of the detector can be calculated by imaging the direct beam for three different positions of the arm motors.

For each value of the rocking angle ω, each illuminated pixel is converted into detector angles and to the corresponding scattering vector Q, calculated as the difference between the wavevector of the incident beam and the wavevector of the diffracted beam for each pixel position. The XSOCS software performs a numerical Gaussian fitting to locate the Q_x, Q_y and Q_z coordinates in the reciprocal space, providing a three dimensional reciprocal space map for each position of the sample, as shown in Fig. 2.18.

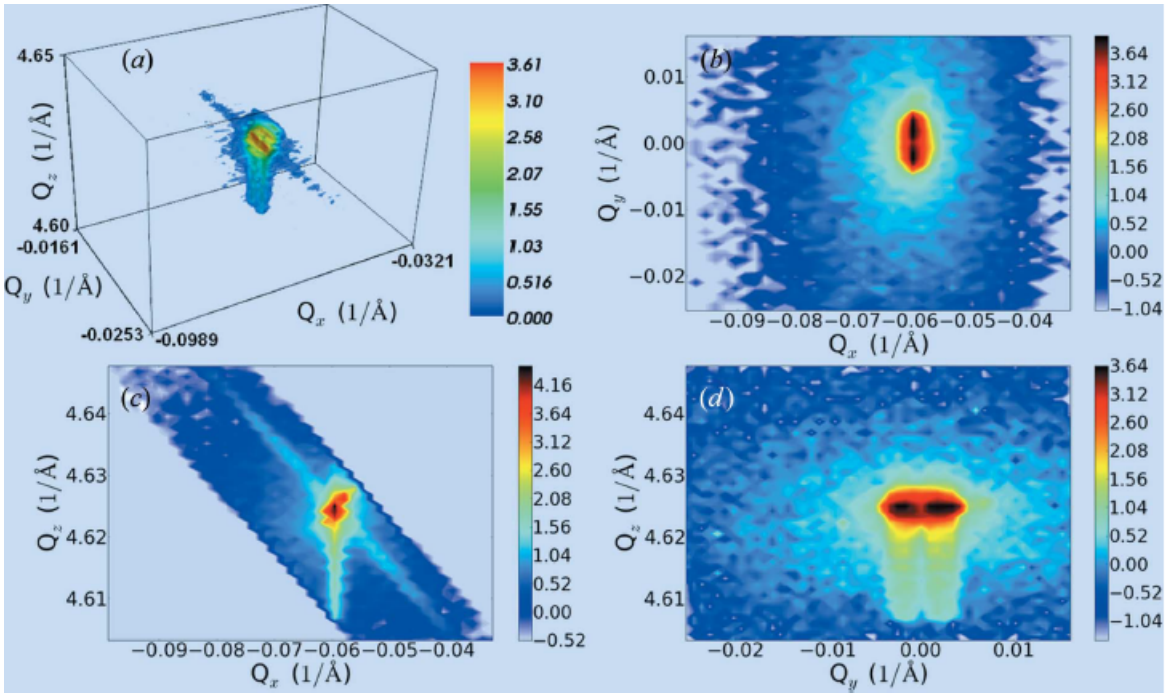

Figure 2.18 – *(a) Example of three-dimensional reciprocal space map of a Bragg peak, for a given position of the sample. Cuts of the 3D representation as a function of Q_x and Q_y (b), Q_x and Q_z (c) and Q_y and Q_z (d) [58].*

2.7 Experimental settings and parameters

The K-map scanning was carried out on a slightly deformed Al-0.1wt.%Mn polycrystal. A dog-bone specimen with a gauge length of 3 mm and square cross section of 1 X 1 mm^2 was deformed in tension by means of the Kammrath load frame (see Section 2.5.4). The tensile test was interrupted to 0.5% strain, in order to produce a relatively simple dislocation arrangement. The specimen was previously recrystallised by a heat treatment as described in Section 2.1, resulting in an average grain size of about 100 μm. An EBSD acquisition was carried out using a JEOL 2000FX

scanning electron microscope equipped with a NordlysNano camera, with a step size of 1.2 μm. The specimen surface was prepared by the polishing procedure described in Section 2.5.3.

Based on the resulting map, a grain with orientation defined by the Miller indices (17, 24, $5\bar{9}$)[35, 44, 28] (where the crystallographic direction and plane normal are parallel to the tensile axis and to the normal of the scanned surface, respectively) was selected for XRD analysis. The choice of this grain has a practical reason: the diffraction vector $11\bar{3}$ lies at an angle of 4.4° with respect to the normal of the specimen surface, that allows an easy determination of the average diffraction angle once the specimen is positioned in the X-Ray goniometer. The Kikuchi lines characterizing the grain had band contrast values in the 185–225 range (on a scale from 0 to 255), qualitatively indicating the presence of moderate strains (2.19).

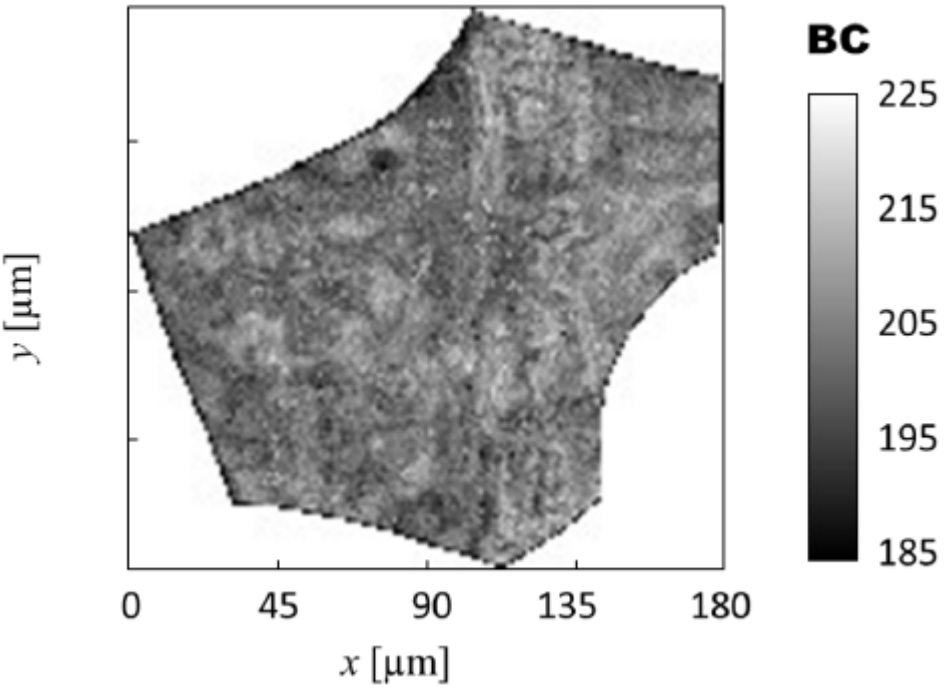

Figure 2.19 – *Band Contrast map for the analysed grain obtained with HKL Channel5 commercial EBSD software ([59]).*

For the K-map scanning, the grain was located using an optical microscope situated above the specimen, as shown in Fig. 2.15. The grain was scanned on a rectangular grid with a step size of 0.55 μm, with a monochromatic X-Ray beam of 8 keV and resolution of $\Delta E/E = 10^{-4}$ resulting from a Si(111) double crystal monochromator. The beam focused by a tungsten Fresnel zone plate had a vertical size of about 120 nm at the sample position. A Maxipix fast readout photon counting detector of 516 X 516 pixels and 55 μm pixel size was placed at a distance of 479 mm downstream of the sample.

The beam focused by a Fresnel zone plate had vertical and horizontal sizes of about 120 and 200 nm, respectively. The measurement consisted in collecting with

the Maxipix detector diffraction images of the $11\bar{3}$ Bragg reflection while translating the sample in front of the beam. An area of 200 X 200 μm around the selected grain was scanned, covering the whole ω range for which a diffraction signal was recorded by the detector. This resulted in a total acquisition time of about 15 h.

2.8 Conclusions

In this chapter we presented the experimental devices used in this thesis work to characterize the intragranular orientation gradients, caused by the formation of geometrically necessary boundaries during deformation.

- *The material* used in this work is a binary alloy Al 0.1% Mn, with an average grain size of about 100 μm, obtained after a static recrystallization treatment at 500°C for 9 minutes. Due to its low yield stress, this alloy is easy to deform plastically, without the formation of stacking faults and partial Shockley dislocations.
- *The 3DXRD technique* was used to characterize the dislocation wall formation and evolution during a tensile deformation by illuminating the specimen by hard X-Rays from synchrotron source. Contrarily to classical X-Ray investigations, the 3DXRD allows to carry out a grain by grain analysis of the predominant misorientation axes within single grains, through the study of the three dimensional intensity profiles of diffraction spots in the reciprocal space. Moreover, diffraction spots can be followed through several strain levels, providing information about the evolution of grain orientation gradients.
- *The indexing procedure* was performed by means of the ImageD11 software, developed at the European Synchrotron Radiation Facility in Grenoble. This step is particularly important, because it provides the knowledge of the average orientation of diffracting grains, as well as their center of mass position and which diffraction spots they give rise to. The calibration of the 3DXRD setup is also taken into account, avoiding any wrong interpretation of diffraction peak intensity profiles due to detector distortions, background noise and specimen misalignments.
- *The EBSD technique.* This device, installed in a SEM, provides the orientation maps of the investigated microstructure. The technique was used to cross check the 3DXRD results and to better understand grains fragmentation mechanisms and dynamics, by means of disorientation maps of single grains with respect to their initial orientation. Considering an average grain size of 100 μm, one can cover about half a hundred grains with an angular resolution of 0.1° and a spatial resolution of 1 μm in about 10 hours.

– *The K-map* was applied to study grain subdivision by a scanning X-Ray technique, whose results were compared to those obtained by EBSD. The determination of the magnitude of the scattering vector of Bragg peaks allowed the determination of intragranular strains as well as the average dislocation density within the selected grain.

In this section we showed the experimental protocol followed in this study. In the next chapter, we present the results obtained by 3DXRD, as well as the post-treatment method of diffraction images.

3 Grain orientation spread characterization by 3DXRD

Contents

The formation of geometrically necessary boundaries during the application of tensile deformation was characterized by analysing the azimuthal maps of the three dimensional intensity distributions. As previously mentioned, the 3DXRD technique provides the advantage of tracking diffraction spots, generated by single grains of a polycrystal, *in situ* through different strain levels. Nevertheless, it is important to underline that the 3DXRD analysis leads to the knowledge of the total misorientation angle and the predominant misorientation axis over the whole grain.

This chapter is divided into three parts: first, the investigation of the grains being indexed and "followed" through different strain levels is presented. The experimental average orientation evolution with deformation is compared with the theoretical predictions of the Taylor model. In the second part, we present the projection method of the resulting three dimensional intensity distributions of diffraction spots on the azimuthal plane, through which a grain by grain characterization of the predominant misorientation axes and angles, caused by the presence of dislocation walls, is possible. In the last part, azimuthal reciprocal space maps were built for the same diffraction spots tracked through four strain levels, observing a change of their shape, which indicates a change of the dislocation walls structure within the grain.

3.1 Investigation of indexed grains

The first step consisted in the identification of the grains within the illuminated volume of the polycrystal. Starting from diffraction frame images, whether the diffraction spots position in terms of the angles (2θ, η, ω) is known, it is possible to index diffracting grains (in terms of their orientation matrices) as well as their center of mass position with respect to the sample coordinate system. Moreover, a list of the diffraction spots generated by the considered diffracting grain is provided by ImageD11, that makes possible a grain-by-grain analysis of geometrically necessary boundaries.

3.1.1 Experimental diffraction frames

As previously mentioned, diffraction occurs from lattice planes set at an angle θ_B, defined by the Bragg law, with respect to the incident beam. The resulting diffracted beam leads to the appearance of a diffraction spot on the two dimensional detector. The radial position of the spot is dependent on the angle $2\theta_B$ as shown in Figure 2.2. For a given family of (hkl) lattice planes, the value of $2\theta_B$ is constant, hence all diffraction spots coming from these (hkl) planes define a circular pattern, known as Debye ring. An experimental diffraction image is therefore composed of different diffraction spots positioned on concentric Debye rings related to different (hkl) lattice planes. The Table 3.1 shows the values of the angle $2\theta_B$ for different (hkl) planes of an Al 0.1% Mn considering the experimental conditions presented in the previous chapter. Spots position in terms of the azimuthal angle η and the rocking angle ω are exclusively dependent on grain orientation.

Table 3.1 – *Values of the angle $2\theta_B$ for different (hkl) families of an Al 0.1% Mn, considering the experimental wavelength of the incident X-Ray beam (60 keV).*

Ring number	hkl family	$2\theta_B$ (degrees)
1	(111)	5.08
2	(200)	5.87
3	(220)	8.30
4	(311)	9.74
5	(222)	10.17
6	(400)	11.75
7	(331)	12.80
8	(420)	13.14
9	(422)	14.40

Diffraction spots shape was found to change abruptly during deformation. If we

consider an undeformed sample, the intragrain misorientations are very low and consequently, diffraction spots appear as quite sharp and narrow. When the sample is deformed, the formation of geometrically necessary boundaries causes lattice planes bending, resulting in a spread of the diffracted intensity distribution. In this case, diffraction spots are broader along the azimuthal direction η and spread out on the detector over a larger $\Delta\omega$ interval. This effect can be observed by comparing two diffraction frames recorded for the same rocking angle at two different strain levels 3.1.

If elastic strains are present in the material, broadening of diffraction spots takes also place along the 2θ direction due to variations in lattice planes spacing in different regions of the grain.

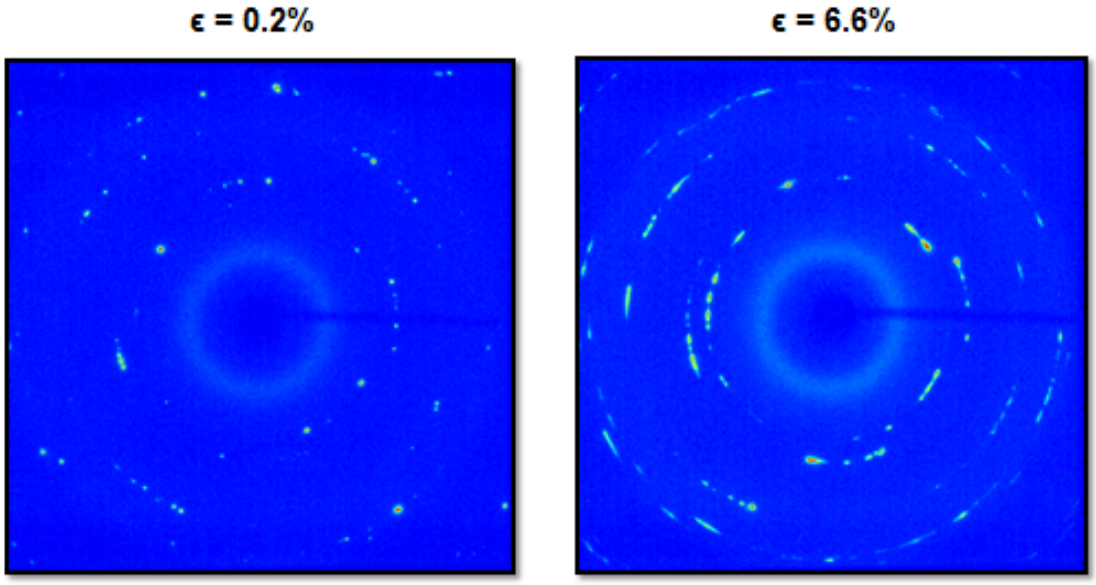

Figure 3.1 – *Comparison between two diffraction frames recorded at the strain levels of* $\varepsilon = 0.2\%$ *and* $\varepsilon = 6.6\%$ *and at the same rocking angle* $\omega = 0°$*. Diffraction spots are very narrow at* $\varepsilon = 0.2\%$ *and broaden along the* η *direction when increasing the strain.*

3.1.2 Grains tracking through different strain levels

The in-situ investigation of the orientation gradients arising from plastic deformation requires the tracking of the same grains through the different scans, corresponding to the strain levels listed in Section 2.3.2. This operation was carried out by comparing the center of mass positions, provided by the software ImageD11, of the indexed grains for each scan: the variation of grains position between two consecutive scans must be very small. A further confirmation was provided by the comparison of the orientation matrices, since grain average orientation should not exhibit an important variation; the global rotation angle between two consecutive strain levels i and j α_{ij} was evaluated by means of the Equation 3.1.

$$\alpha_{ij} = \cos^{-1} \frac{\mathrm{tr}(U_i (S U_j)^{-1}) - 1}{2} \tag{3.1}$$

where U_i and U_j are the orientation matrices of the grain at the scans i and j respectively, and S is the symmetry matrix, taking into account the cubic crystal symmetry. Grain total rotation angle values between the first and the final scan clearly depend on grain orientation, but it never exceeded 7°.

The first two scans were done at zero strain and at the yield stress ($\sigma \approx 11 MPa$). Unfortunately, loading the sample resulted in a significant rigid displacement, which made impossible to follow single grains between these two states. It is also important to underline that with higher applied strain, the indexing procedure is less efficient: this is because spots broadening can result in an overlap between spots being close on the detector, but diffracted by different grains. Another reason is represented by the loss of intensity caused by the bent crystals. Table 3.2 summarizes the number of indexed grains for each scan: one can observe that the number of indexed grains decreases by about 86% between the scan at zero strain and the scan at the strain $\varepsilon = 6.6\%$.

Table 3.2 – *Number of the indexed grains as a function of the macroscopic strain levels.*

Strain level (%)	Number of indexed grains
0	440
0.2	314
1	284
3	217
6.6	61

3.1.3 Evolution of grain average orientation and comparison with the visco-plastic self-consistent model

The 3DXRD technique offers the possibility of visualising the formation of deformation textures by the analysis of the evolution of grain average orientation. This was achieved by indexing and following single grains through several strain levels. Fig. 3.2 shows the stereographic triangle describing the experimental lattice rotations between the strain levels $\varepsilon = 0.2\%$ and $\varepsilon = 3\%$. In the case of uniaxial tension, lattice rotations can be described by considering the rotation of the tensile axis (the z axis of the sample coordinate system) in the crystallographic frame of the grains (inverse pole figure).

A first visual inspection of the inverse pole figure shows that grain rotational paths strongly depend on their initial orientation. In particular:

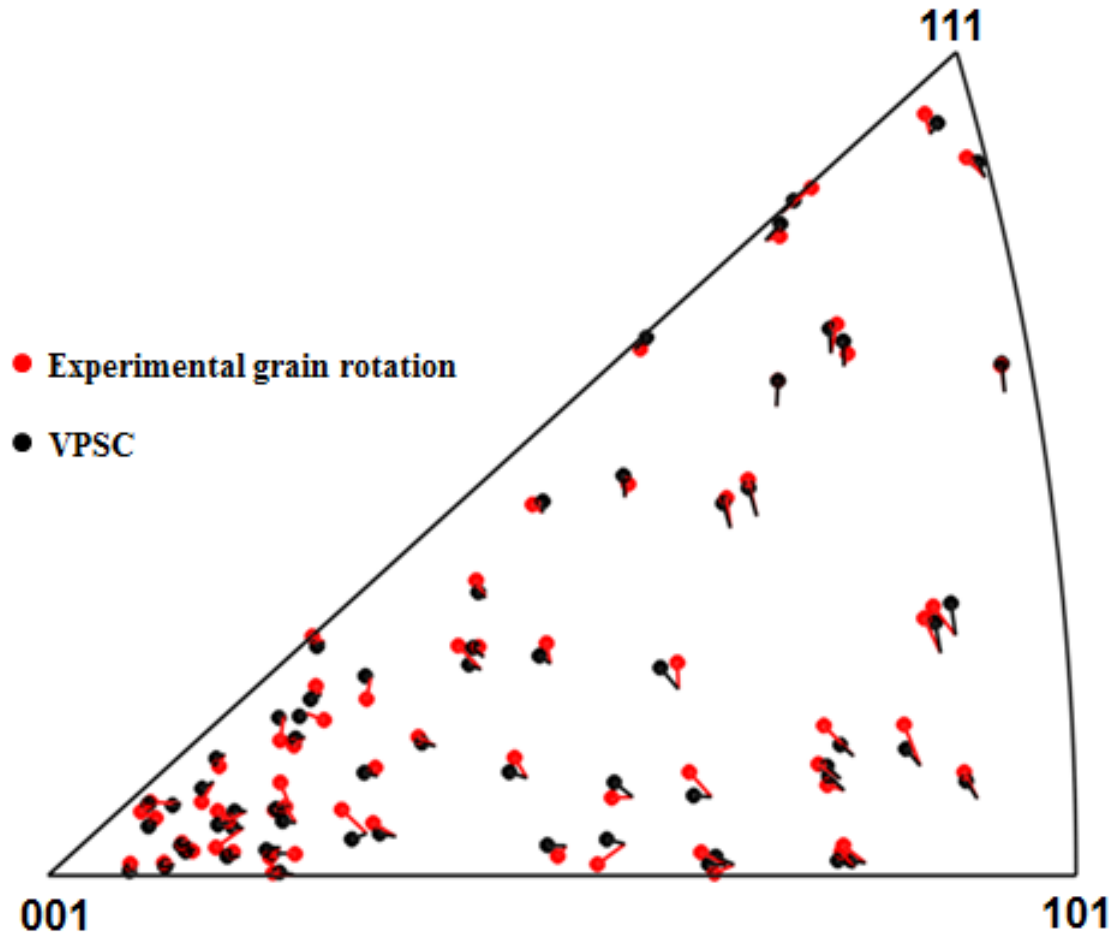

Figure 3.2 – *Stereographic triangle showing the rotational paths of 72 grains between the strain levels $\varepsilon = 0.2\%$ and $\varepsilon = 3\%$. The red lines represent the experimental grain rotations, while the theoretical predictions of the Viscoplastic Self Consistent (VPSC) model are showed by the black lines. The spots represent the final average orientation of the grains.*

- Grains near the <101> pole rotate towards the center of the stereographic triangle and the <111> pole.
- Grains at the <101> - <111> line rotate towards the <111> corner.
- Grains close to the <001> - <111> line rotate towards the <111> corner.
- Grains near the <001> pole rotate towards different directions.

For each grain, the slip amount on every slip system can be evaluated by means of the VPSC model [60], whether the comparison between the experimental rotational paths and the theoretical predictions match. Fig. 3.2 illustrates the predictions of grain rotations as black lines. These simulations were carried out by using the *VPSC7c* code [61]. The figure shows a good match between theory and experiment for the grains near the 111 corner and at the center of the stereographic triangle. For the grains near the 101 pole, the theoretical rotation is usually lower than that observed during the experiment. The trends are comparable: these results agree with previous findings in the literature [22], resulting from the comparison with the Tylor-Bishop model. Predictions of the rotation of the tensile direction near the 001

corner are very different from the experimental trends, showing a large variation of the rotation directions, even for grains with similar orientation.

3.1.4 Determination of the grain size distribution from experimental diffraction spots

The investigation of the experimental diffraction spots allows to carry out a quantitative analysis of the grain size distribution within the illuminated volume. Since the integrated intensity of diffraction spots in the $(2\theta, \eta, \omega)$ space is proportional to the volume of the grain they are scattered from, the idea was to compare the integrated intensity of all diffraction spots of one grain with the total intensity which was measured during a scan.

In order to perform a correct calculation, the measured intensity of each *hkl* reflection was corrected by considering two parameters:

– The Lorentz polarization factor L_{hkl}. When a crystal is rotated while illuminated by a monochromatic X-Ray beam, lattice planes will satisfy the Bragg law and diffraction occurs. In general, the different lattice planes do not occupy this position for equal lengths of time, and the total amount of the reflected intensity is proportional to this time. The Lorentz factor is essentially this time factor, and it is proportional to the time of reflection permitted to each hkl plane, or inversely proportional to the velocity with which the plane passes through the diffraction position. Considering the reciprocal space point of view, a reflection with a high value of the Lorentz factor appears over a larger ω interval onto the detector, since its corresponding reciprocal space point lies longer onto the surface of the Ewald sphere during the rotation of the illuminated sample. The Lorentz factor of a hkl reflection can be calculated by the formula:

$$\mathrm{L_{hkl}} = \frac{1}{\sin(2\theta) \mid \sin(\eta) \mid} \tag{3.2}$$

It is evident that the value of L_{hkl} depends both on the Debye ring and on the position of the reflection along the ring. In general, the more a diffraction spot is situated at an η position closer to the vertical symmetry axis of the area detector, the higher is its L_{hkl} value.

– The structure factor F_{hkl}. This is a mathematical function which describes the amplitude and the phase of a wave diffracted from crystal lattice planes characterized by Miller indices hkl. It represents the sum of the individual scattering powers of the atoms of the unit cell. The total scattering power of the whole unit cell can be expressed by the equation:

$$\mathrm{F_{hkl}} = \sum_{\mathrm{j}} \mathrm{f_j exp}[2\pi \mathrm{i}(\mathrm{hu_j} + \mathrm{kv_j} + \mathrm{zw_j})] \tag{3.3}$$

where f_j is the scattering factor of the atom j in the unit cell and u_j, v_j and w_j are its coordinates. The intensity of a reflection is related to the structure factor as shown by Eq. 3.4 and depends on the Miller indices of the diffracting lattice plane.

$$\mathrm{I_{hkl}} \sim \mid \mathrm{F_{hkl}} \mid^2 \tag{3.4}$$

The correct value of the intensity of the hkl reflection I_{hkl} can be evaluated by the Equation:

$$\mathrm{I_{hkl}} = \frac{\mathrm{I^m}}{\mathrm{L_{hkl}} \cdot \mathrm{F^2_{hkl}}} \tag{3.5}$$

where I^m is the integrated intensity of the reflection in the $(2\theta, \eta, \omega)$ space. The total intensity scattered by a grain was calculated by the sum of the corrected intensities of all the reflections it generated (3.6 [55]). The list of the diffraction spots produced by the considered grain is provided by the software ImageD11.

$$\mathrm{I_{grain}} = \sum \mathrm{I_{hkl}} \tag{3.6}$$

The ratio between the volume of the grain and the illuminated volume of the sample can be related to the ratio between the intensity scattered by the grain and the total intensity acquired during a scan (Eq. 3.7). The grain size was determined as the diameter of a sphere of equal volume.

$$\mathrm{V_{grain}} = \mathrm{V_{scan}} \frac{\mathrm{I_{grain}}}{\mathrm{I_{scan}}} \tag{3.7}$$

Where V_{scan} is the volume of the illuminated sample (1000 X 1000 X 200 μm^3) This calculation was carried out with the assumption that there is not any unindexed diffraction spot: this approximation is acceptable for the scan of the undeformed state, since the amount of unindexed reflections is equal to the 2% of the total number. Fig. 3.3 is the histogram of the resulting distribution of the grain size within the illuminated volume for the undeformed sample. The average value of the grain size equals 92 μm which is close to the average grain size measured by EBSD (100 μm).

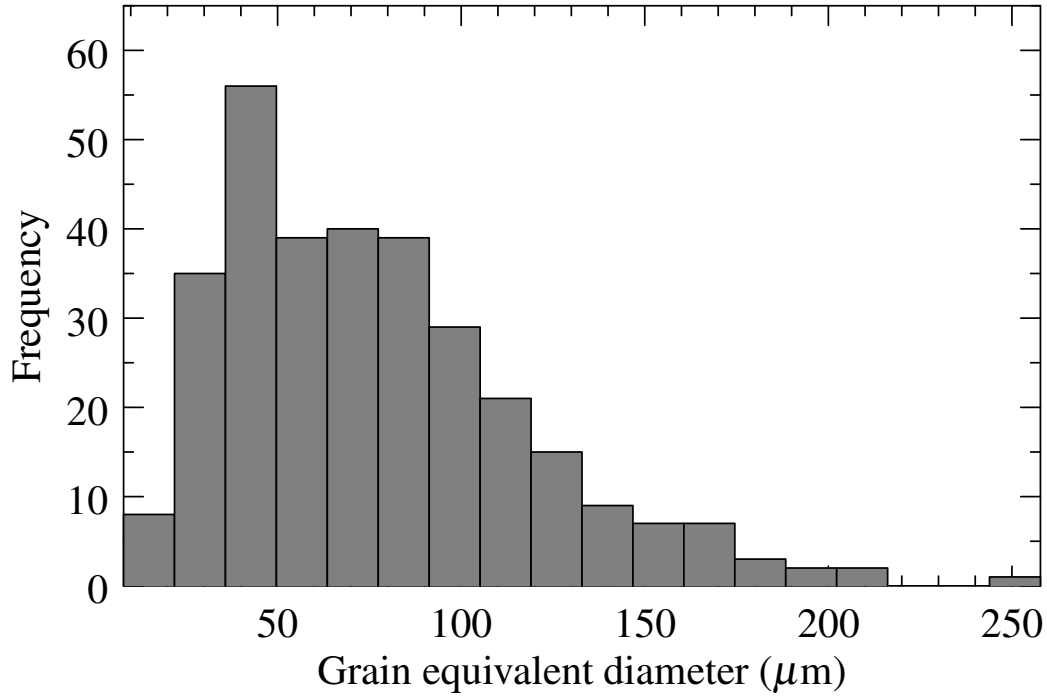

Figure 3.3 – *Grain size distribution of the illuminated volume for the undeformed state of the specimen, obtained from diffraction spots intensities.*

3.2 Determination of the orientation spread within single grains

The deformation induced orientation gradients within the grains leads to the broadening of the diffracted intensity along both the radial and the azimuthal directions in the reciprocal space. Normally, plastic deformation produces only small broadening in the radial direction. Contrary to this, azimuthal broadening is much more significant, and is related to the rotation of the crystal lattice induced by the presence of dislocation boundaries. For this reason, the characterization of the global misorientation axes and angles arising, requires the projection of the experimental diffraction spots on the *azimuthal plane*, perpendicular to the mean diffraction vector of the reflection. In this section, we first describe the methodology for calculating azimuthal intensity distributions in the reciprocal space of single grains, which is then applied to evaluate the broadening of the rocking curves.

3.2.1 Projection of diffraction spots on the azimuthal plane

Given the orientation matrix of a grain U, the position of the spot center position of a hkl peak can be predicted based on the basic diffractometer equation:

$$\vec{H} = (\Omega \mathrm{U}^{-1}\mathrm{B})^{-1}\vec{G}^{\mathrm{L}}_{\mathrm{hkl}} = (\mathrm{U}^{-1}\mathrm{B})^{-1}\Omega^{-1}\vec{G}^{\mathrm{L}}_{\mathrm{hkl}} \tag{3.8}$$

where $\vec{G}^{L}_{hkl}$ is the diffraction vector in the laboratory frame, Ω is the rotation matrix describing crystal rotation around Oz and $\vec{H} = (h,k,l)^T$ is the recipro-

cal lattice vector. B is the orthonormalization matrix transforming the rectilinear reciprocal lattice frame of the crystal to a Cartesian frame attached to the same reciprocal lattice [62]. For cubic systems, the orthonormalization matrix is reduced to the form:

$$B = \begin{pmatrix} \frac{1}{a} & 0 & 0 \\ 0 & \frac{1}{a} & 0 \\ 0 & 0 & \frac{1}{a} \end{pmatrix}$$

where a is the lattice parameter. Since the ImageD11 software provides the UBI matrix ($(U^{-1}B)^{-1}$ in Eq. 3.8) for every grain, U and B were obtained by means of a *QR decomposition* following the Householder method [63]. Equation 3.8 is the result of the composition of three transformations:

- Diffraction vectors are expressed in the *sample coordinate system* by the Ω rotation matrix. In particular, diffraction spots are brought back to the rocking angle $\omega = 0$.
- The orientation matrix of the grain U allows the transformation from the sample frame to the *crystal coordinate system* which is attached to the crystal lattice.
- The orthonormalization matrix B provides the final transformation to the reciprocal space.

The peak center position on the detector is obtained in a second step as the intersection between the diffracted wave vector $\vec{k}$ and the detector plane, where $\vec{k}$ satisfies the Bragg condition

$$\vec{k} = \vec{k}_1 + \vec{G}^{\mathrm{L}}_{\mathrm{hkl}} \tag{3.9}$$

and $\vec{k}_1$ coincides with the direction of the incident beam aligned with the Ox axis of the laboratory frame. To map the experimental intensity distribution in the reciprocal space, a diffracted wave vector $\vec{k}_n$ is associated to each detector pixel at each rotation step ω, and equations (3.9) and (3.8) are applied to calculate $\vec{G}^L_{hkl,n}$ and $\vec{H}_n$, respectively. It is evident that the components of $\vec{H}_n$ will be now real numbers, but due to the limited orientation spread in the grains they will be close to the integers h, k, l. The reciprocal space maps of three dimensional diffraction spots are then obtained by associating the intensity values to each diffraction vector $\vec{H}_n$. The azimuthal intensity distribution in reciprocal space is then obtained by projecting the vectors $\vec{H}_n$ on the plane perpendicular to their average defined as:

$$\vec{H} = \frac{\sum_{\mathrm{n}} \mathrm{I_n} \vec{H}_{\mathrm{n}}}{\sum_{\mathrm{n}} \mathrm{I_n}} \tag{3.10}$$

where I_n is the intensity of pixel n. To perform the projection we introduced a local coordinate system with origin at the center of the intensity distribution and defined by the orthonormal basis ($\vec{e}_\xi$, $\vec{e}_\zeta$, $\vec{e}_H$) (see Fig. 3.4). The unit vector $\vec{e}_\zeta$ is perpendicular to $\vec{H}$ being defined as the cross product between average wave vector $\vec{k}$ and $\vec{k}_1$ (both transformed to the reciprocal frame):

$$\vec{e}_\zeta = \frac{\vec{k} \times \vec{k}_1}{||\vec{k} \times \vec{k}_1||} \tag{3.11}$$

$$\vec{e}_\xi = \vec{e}_\zeta \times \vec{e}_\mathrm{H} \tag{3.12}$$

$$\vec{e}_\mathrm{h} = \frac{\vec{H}}{||\vec{H}||} \tag{3.13}$$

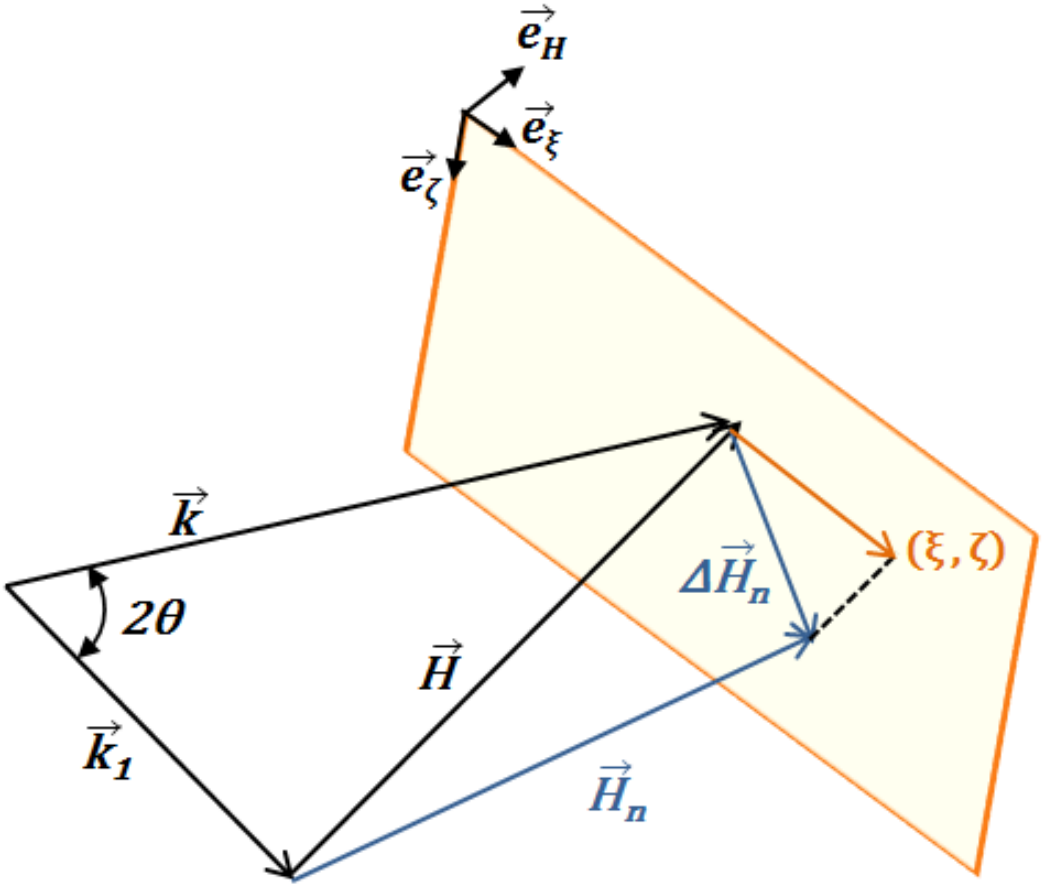

Figure 3.4 – *Schematic drawing of the azimuthal plane (perpendicular to the mean diffraction vector $\vec{H}$) in the reciprocal space. The plane is defined by the unit vectors $\vec{e}_\zeta - \vec{e}_\xi$. The azimuthal broadening is due to the rotational part of the displacement field of geometrically necessary boundaries.*

The angular spread around the mean diffraction vector $\vec{H}$ can be now obtained by projecting the difference vector $\Delta\vec{H}_n = \vec{H}_n - \vec{H}$ on the azimuthal plane. Its coordinates (ξ, ζ) are obtained as:

$$\xi = \vec{e}_{\xi} \cdot \frac{\Delta \vec{H}_{\mathrm{n}}}{||\vec{H}||} \cdot \frac{180}{\pi} \tag{3.14}$$

$$\zeta = \vec{e}_{\zeta} \cdot \frac{\Delta \vec{H}_{\mathrm{n}}}{||\vec{H}||} \cdot \frac{180}{\pi} \tag{3.15}$$

The described procedure projects the three dimensional diffraction spot in the reciprocal space on the azimuthal plane by integrating intensities along the $\vec{e}_H$ unit vector. Fig. 3.5 shows an example of the azimuthal intensity distribution obtained by projecting the corresponding 3D distribution.

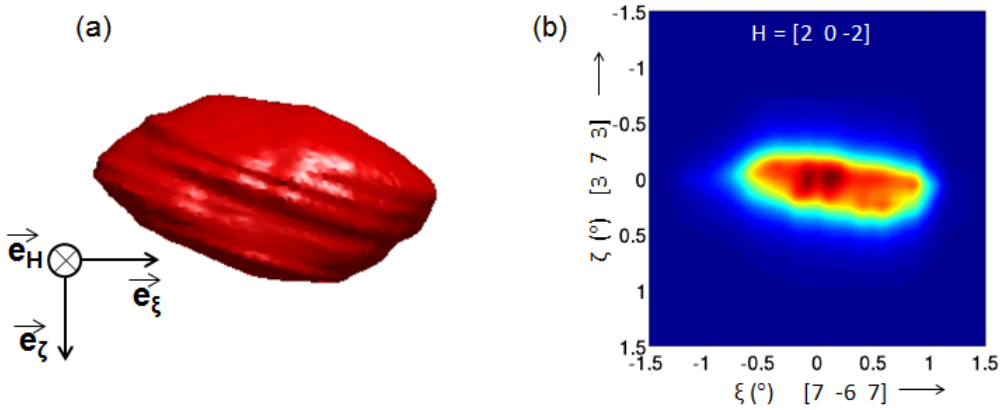

Figure 3.5 – *Example of a three dimensional reciprocal space iso-intensity contour of a* $[20\bar{2}]$ *reflection (a) and the corresponding azimuthal intensity distribution (b), obtained by integrating intensities along* $\vec{e}_H$ *(strain level* $\varepsilon = 0.2\%$*). The coordinates* (ξ, ζ) *quantify the azimuthal broadening along the crystallographic directions corresponding to the unit vectors* $\vec{e}_{\zeta}$ *and* $\vec{e}_{\xi}$*)*

3.2.2 FWHM of the azimuthal intensity distributions

The characterization of the plastic deformation of polycrystals by soft X-Rays is actually carried out by recording the intensity profile as a function of the rocking angle of the sample (*rocking curve*), whose shape is in most cases close to a Gaussian function. The amount of GNDs is related to the Full Width at Half Maximum (*FWHM*) of this function, which is defined as the width of the intensity curve measured between those points which are half the maximum amplitude. The azimuthal broadening of diffraction spots was measured by fitting the corresponding distribution by a two dimensional Gaussian function (Fig. 3.6) and measuring the FWHM along the direction of maximum broadening. The fitting function has the form:

$$\mathrm{f}(\xi, \zeta) = \mathrm{A} \cdot \exp\left(-\left(\frac{(\xi' - \xi_0)^2}{2\sigma_{\xi}^2} + \frac{(\zeta' - \zeta_0)^2}{2\sigma_{\zeta}^2}\right)\right) \tag{3.16}$$

$$\begin{pmatrix} \xi' \\ \zeta' \end{pmatrix} = \begin{pmatrix} cos(\alpha) & -sin(\alpha) \\ sin(\alpha) & cos(\alpha) \end{pmatrix} \begin{pmatrix} \xi \\ \zeta \end{pmatrix}$$

here the coefficient A is the amplitude, ξ_0 and ζ_0 is the center and σ_ξ and σ_ζ are the ξ and ζ standard deviations. The angle α is the rotation angle of the principal axes of the azimuthal intensity distribution with respect to the axes ξ and ζ. The fitting procedure involves therefore 5 parameters, and it was achieved by a least square minimization method between the experimental intensity values and the Gaussian function.

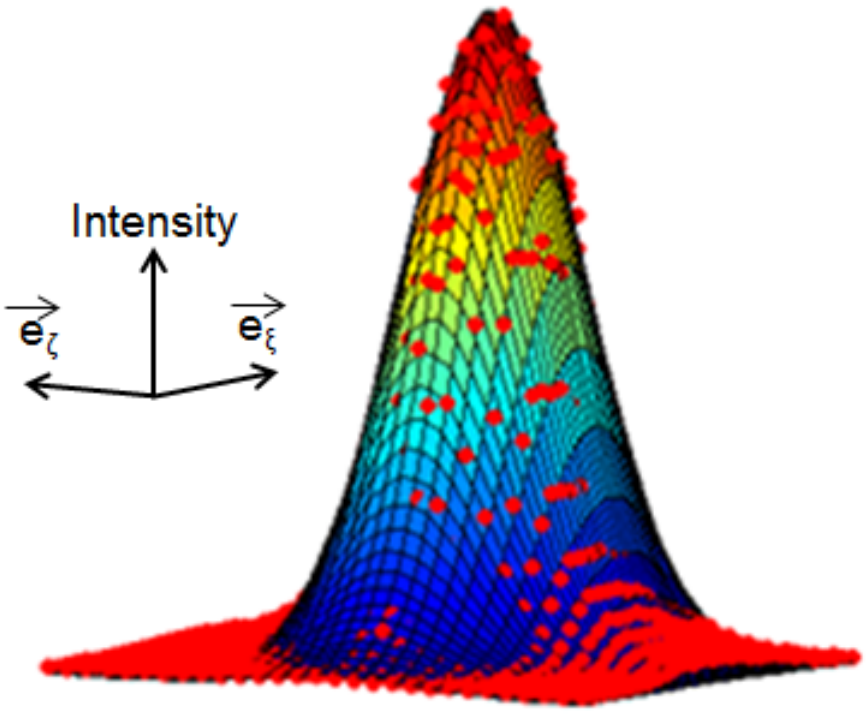

Figure 3.6 – *Example of azimuthal intensity distribution fitting by a 2D Gaussian function. Red points represent experimental intensity values at every* (ξ, ζ) *point.*

A statistical study was carried out by comparing the FWHM values of the azimuthal intensity distributions of diffraction spots recorded during the scans at $\varepsilon = 0\%$ and $\varepsilon = 0.2\%$ (Fig. 3.7). It is important to point out that we retained only those values for which the fit error was below 10%. It can be stated that the measured reflections present an azimuthal broadening above 0.2°, that represents the *instrumental broadening*. It is clear that the application of the macroscopic strain $\varepsilon = 0.2\%$ causes already an increase of the broadening; such meaningful change is the result of the formation of geometrically necessary boundaries, which are found to be present already at the *beginning of the macroscopic plastic deformation*.

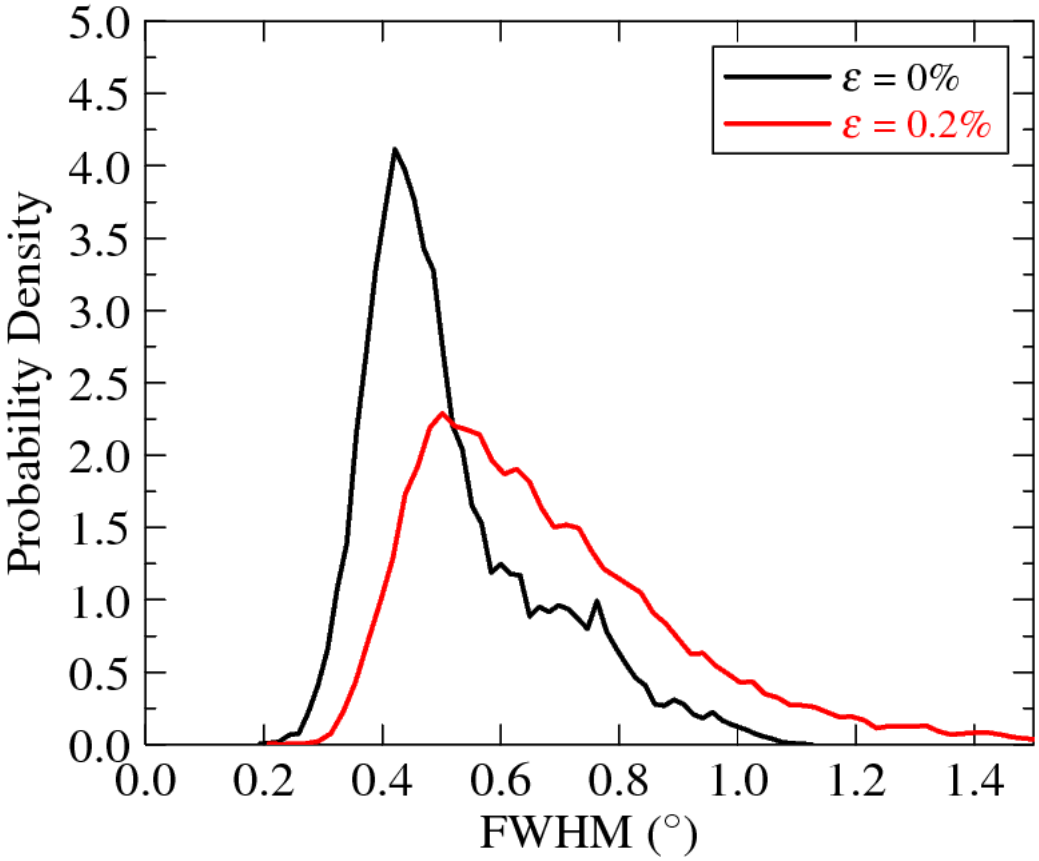

Figure 3.7 – *Distribution of the FWHM of spots belonging to the recrystallized state (black line) and to the strain level $\varepsilon = 0.2\%$ (red line). The higher broadening registered just after the beginning of plastic deformation is due to the formation of GNBs.*

3.3 Evaluation of the predominant misorientation axes within single grains

In this section we present the evaluation of the global rotation axis arising at the beginning of plastic deformation ($\varepsilon = 0.2\%$) in four grains with different orientations by means of the analysis of reciprocal space maps of diffraction spots. The analysis was subsequently extended to 72 grains, in order to check an eventual dependence on grain average orientation. The investigation of the active slip systems based on the calculation of the Schmid factor allowed to hypothesize the most probable arrangement of dislocations forming the geometrically necessary boundaries.

3.3.1 Experimental evaluation

The analysis of the 2D rocking curves of 3DXRD diffraction spots permitted a global characterization of lattice rotations induced by the dislocation boundaries formed during plastic deformation. Sometimes, these boundaries have a very simple structure. Here we present the results for four grains with different orientations, marked with letters in Fig. 3.8. For each reflection scattered by the grain, we built the

corresponding azimuthal intensity distribution, calculating the global misorientation axis by applying Eq. 1.28 to the most broadened reflections. We remark here again that the analysis assumes that dislocation boundaries are made up by one single dislocation type only.

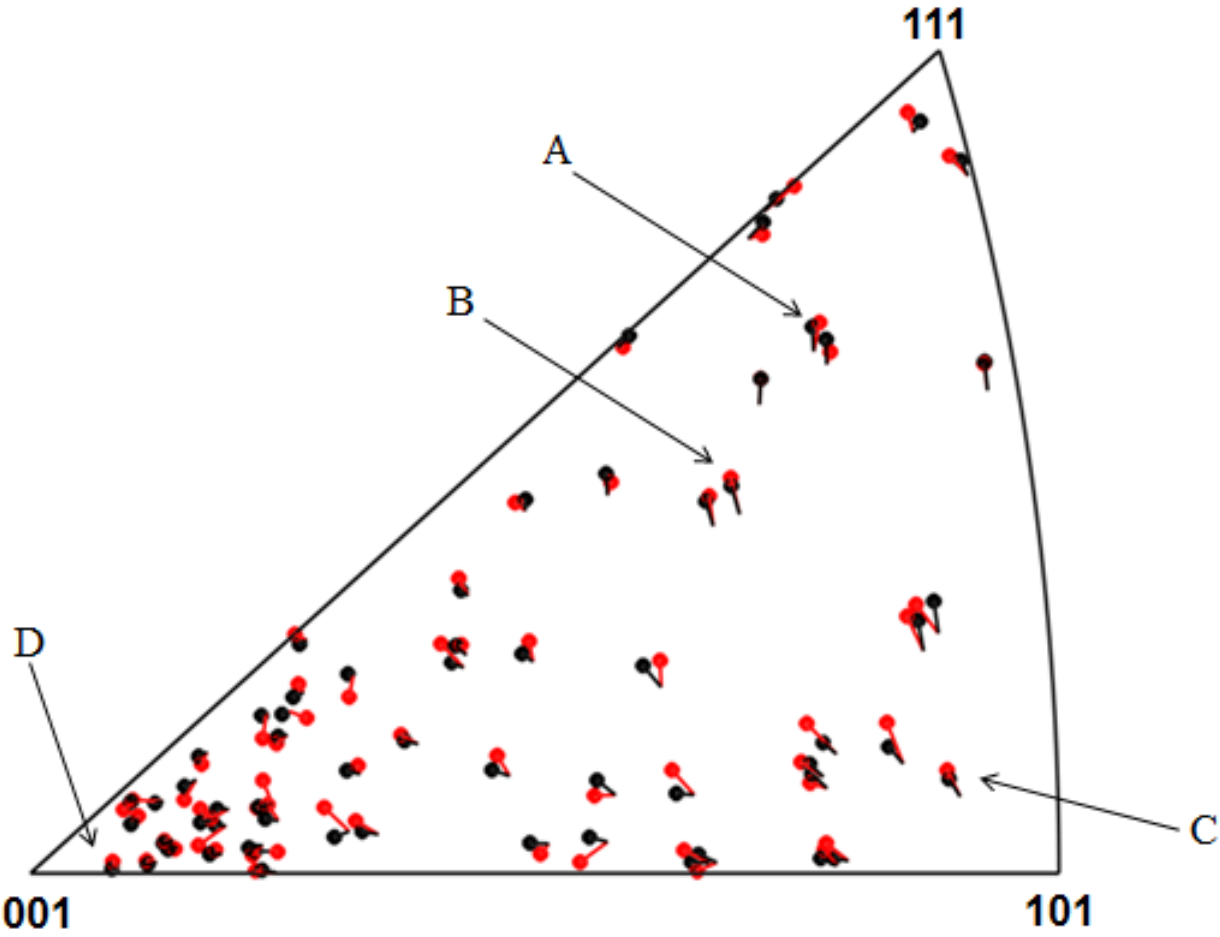

Figure 3.8 – *Stereographic triangle representing indexed grains orientation evolution between the states* $\varepsilon = 0.2\%$ *and* $\varepsilon = 3\%$*. The letters show the grains for which the determination of the misorientation axis is presented.*

Grain A

The analysis of the azimuthal broadening of the spots which come from the Grain A (shown in Fig. 3.8) is presented in Fig. 3.9. The four spots with different diffraction vectors present an elongated shape which points along a crystallographic direction $\vec{h}$. In all cases, if Eq. 1.28 is applied, the misorientation axis direction is found to be the same, e.g. ω_α=[121], which coincides with dislocations line direction in fcc crystals.

It could be noted that only two broadened spots are needed to calculate ω_α. If they are elongated along the crystallographic directions $\vec{h}_1$ and $\vec{h}_2$ respectively, the misorientation axis direction must be perpendicular to both of them:

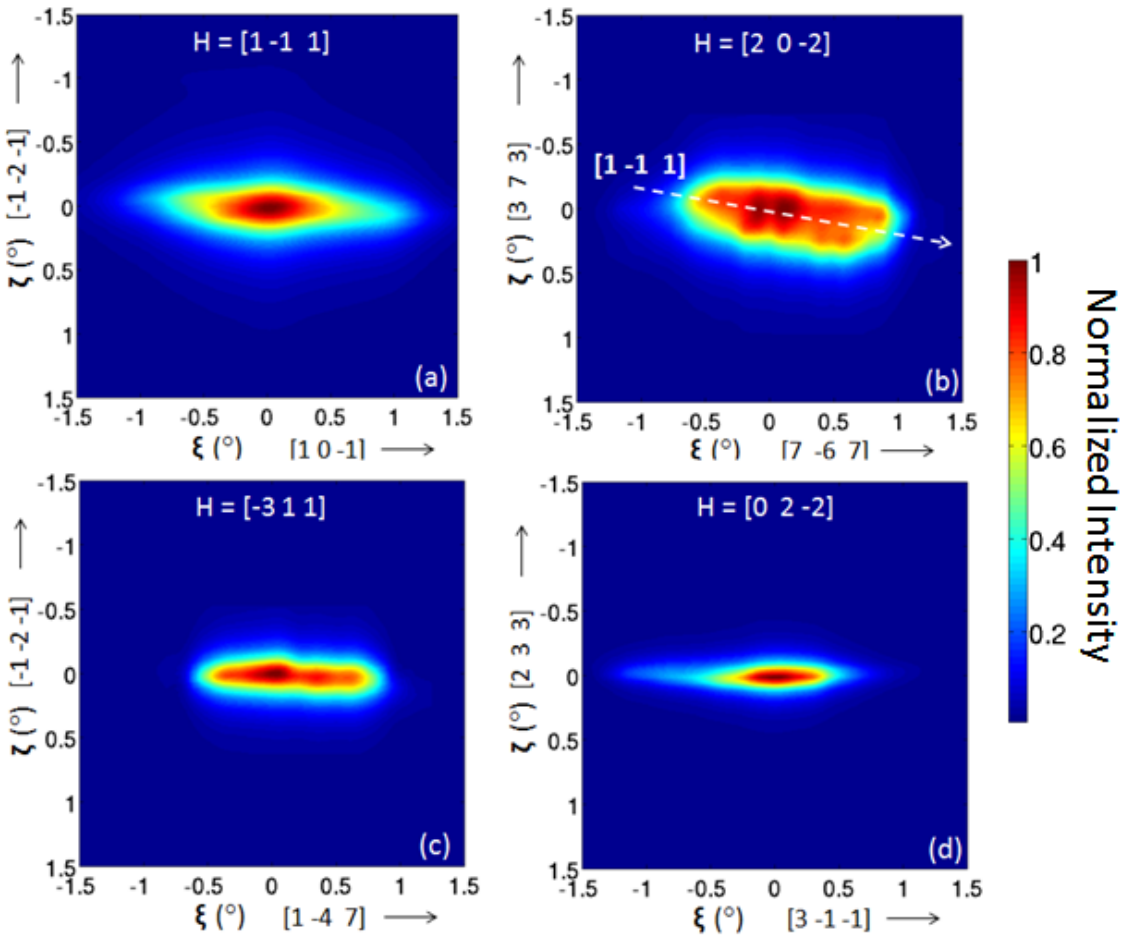

Figure 3.9 – *Broadened spots projected onto the azimuthal plane with different diffraction vectors. The elongated shape is caused by a boundary with misorientation axis along the [1 2 1]. The colorbar shows the normalized intensity scale.*

$$\overrightarrow{\omega_\alpha} = \overrightarrow{h}_1 \times \overrightarrow{h}_2 \tag{3.17}$$

The Schmid factor allows to know the active slip systems, through which the probable dislocation content of the boundary can be deduced. For this case, the most active slip systems were found to be $(1\bar{1}1)[0\bar{1}\bar{1}]$, $(1\bar{1}1)[110]$. This boundary could be therefore formed by a majority of edge dislocations with Burgers vector which belongs to the slip plane $(1\bar{1}1)$ and a lower quantity of dislocations coming from the other active slip planes. This can be observed by looking at the scalar product $\overrightarrow{H} \cdot \overrightarrow{b}$ for every diffraction spot as a function of the corresponding value of FWHM. In fact, the resulting curve should present a minimum when $\overrightarrow{H} \cdot \overrightarrow{b} = 0$ [34] if the predominant Burgers vector is considered. Fig. (3.10) illustrates the calculated $(\overrightarrow{H} \cdot \overrightarrow{b}, FWHM)$ points for the three possible Burgers vectors lying on the slip plane $(1\bar{1}1)$.

One can conclude that the boundary is mainly formed by dislocations with a Burgers vector $\overrightarrow{b} = [10\bar{1}]$, since the corresponding graph shows a minimum in corres-

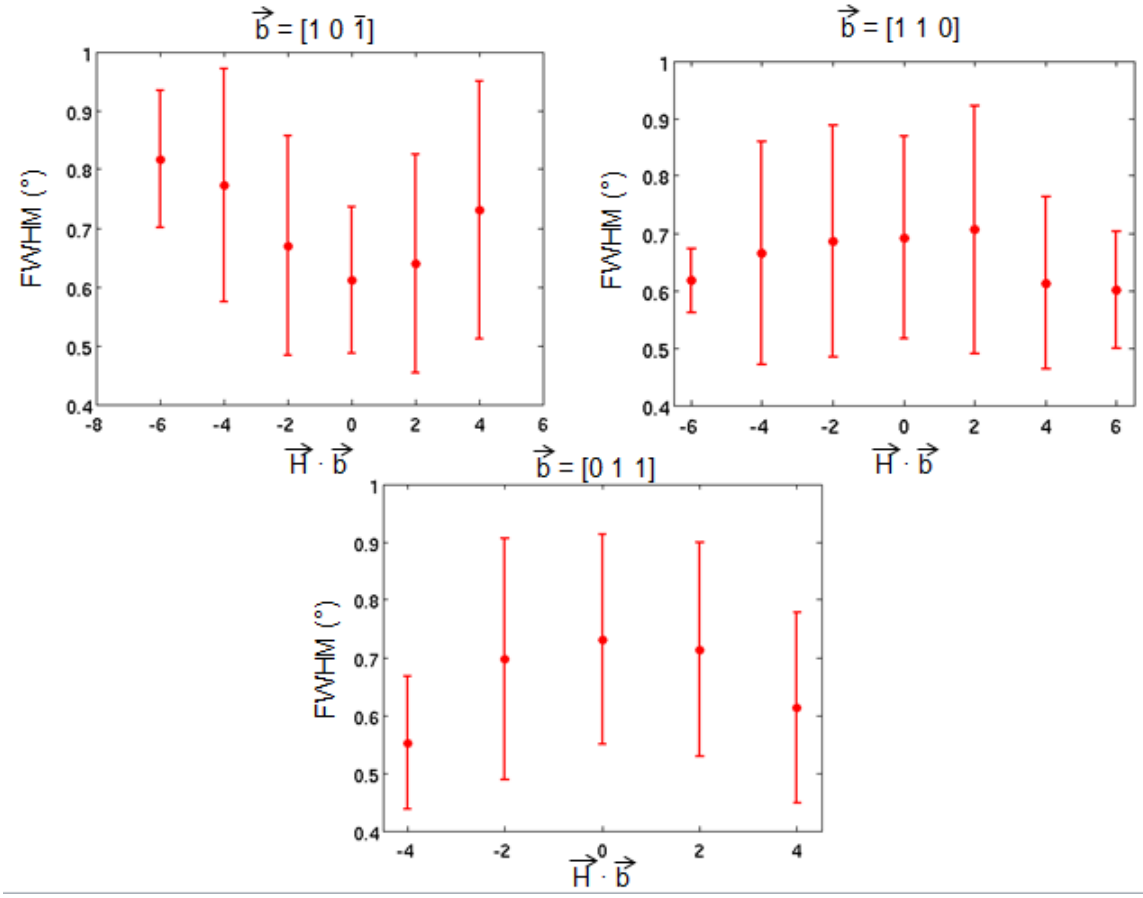

Figure 3.10 – *Evolution of the FWHM of azimuthal intensity distribution of grain A as a function of the scalar product* $\vec{H} \cdot \vec{b}$ *for the three possible Burgers vectors lying in the most stressed slip plane* $(1\bar{1}1)$. *Red dots and red lines represent the mean values of the FWHM and the corresponding standard deviations, respectively.*

pondence of $\vec{H} \cdot \vec{b} = 0$. $\vec{b} = [10\bar{1}]$ can be the result of dislocation reactions between the two most stressed slip systems $(1\bar{1}1)[0\bar{1}\bar{1}]$ and $(1\bar{1}1)[110]$. The non-zero value of broadening is due both to the instrumental broadening and to other geometrically necessary dislocations present in smaller proportions.

Grain B

In the majority of the indexed grains, the structure of geometrically necessary boundaries is very complicated, which made impossible a complete analysis able to predict the dislocation content. This is the case of the Grain B of Fig 3.8. Fig. 3.11 shows two reciprocal space maps of the most broadened spots. Their broadening directions are h_1=$[3\bar{1}0]$ and h_2=$[3\bar{1}\ \bar{1}0]$, respectively, and the application of Eq. 3.17 returns the misorientation axis ω_α=[130]. $(\bar{1}\bar{1}1)[0\bar{1}\bar{1}]$ is the most activated slip system, but slip activity is also present in the $(\bar{1}\bar{1}1)[\bar{1}10]$ and $(111)[1\bar{1}0]$ slip systems. The boundary is probably composed of several sets of dislocations of different type, coming from different slip systems which react or re-arrange in ordered structures, such as square networks of screw dislocations and Lomer locks [23, 25].

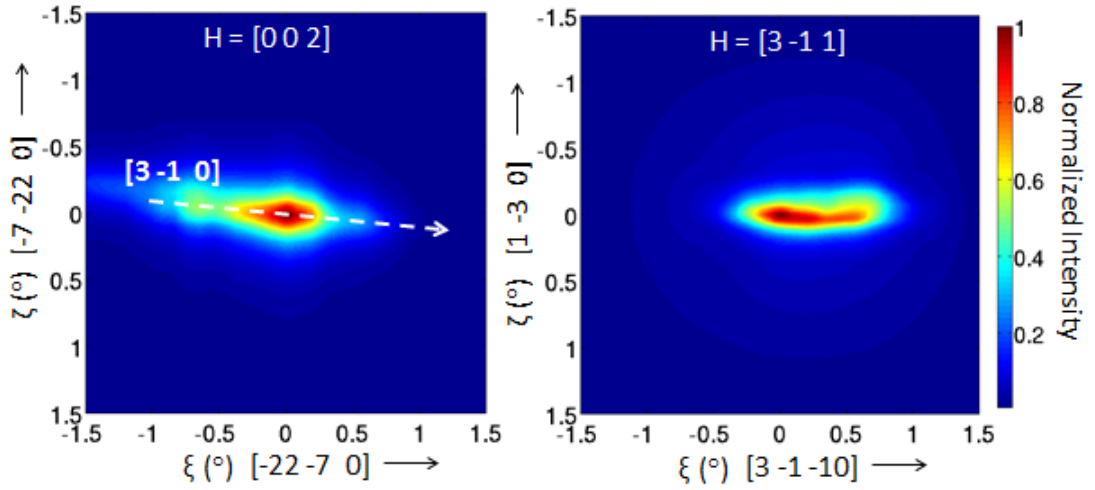

Figure 3.11 – *Azimuthal intensity distribution of the two most broadened spots of grain B.*

Grain C

As before, two broadening directions in the azimuthal plane were found (Fig. 3.12). The resulting misorientation axis is ω_α=[$\bar{1}$11]. This direction is perpendicular to the plane where the highest amount of slip activity is represented by the slip systems ($\bar{1}$11)[01$\bar{1}$] and ($\bar{1}$11)[$\bar{1}\bar{1}$0]. In this case, the boundary could be composed of an hexagonal network of screw dislocations, all having Burgers vectors belonging to the ($\bar{1}$11) plane. This kind of arrangement is commonly observed in deformed Al [25].

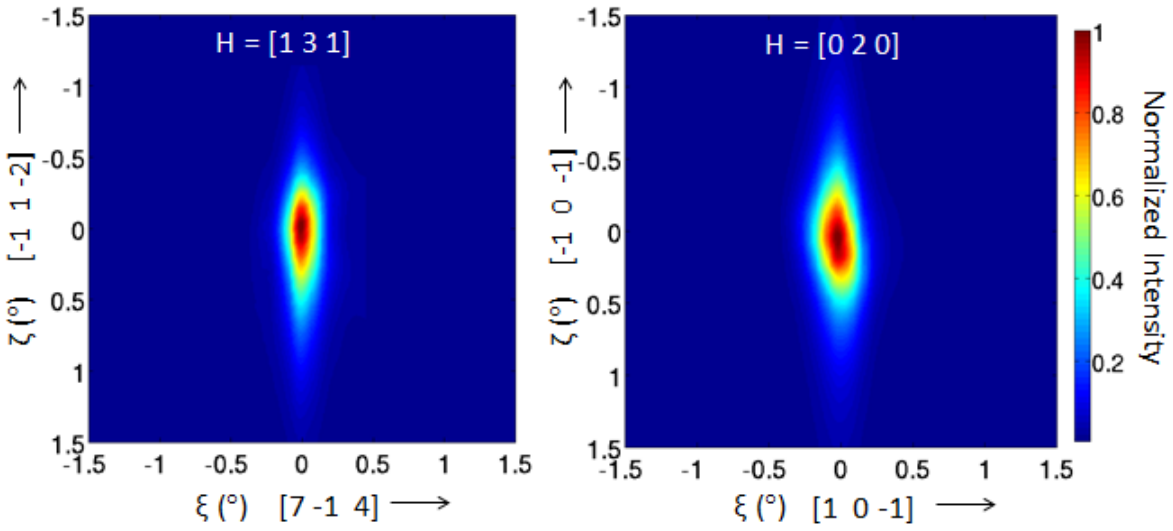

Figure 3.12 – *Azimuthal broadening of the most broadened diffraction spots belonging to the grain C, indicating the presence of a global misorientation axis* ω_α=[$\bar{1}$11].

Grain D

No geometrically necessary boundaries were detected in grains for which the tensile axis is close to the 001 direction. This is very evident from the azimuthal projections relative to the Grain D. The azimuthal projections of diffraction spots show an almost perfect circular shape, without any broadening along preferred directions (Fig. 3.13). The lack of the azimuthal broadening is probably due to the low orientation gradient which occurs in the adjacent regions of a cell boundary, the most observed structure in these grains.

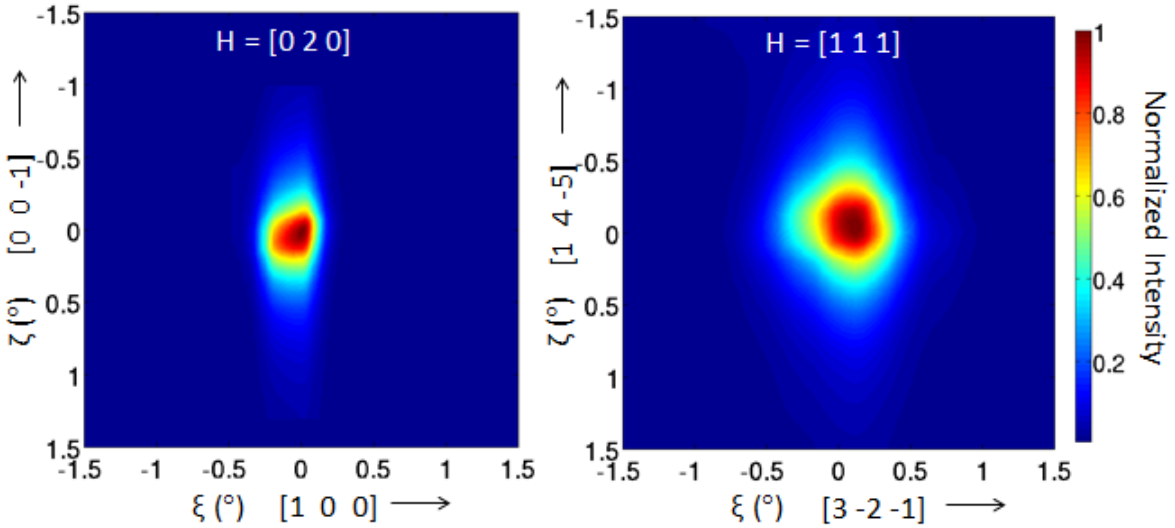

Figure 3.13 – *Circular shape of projected spots of a grain near the 001 corner of the stereographic triangle (grain D). The lack of large and anisotropic broadening is due to the absence of geometrically necessary boundaries.*

3.3.2 Dependence on grain average orientation

The described approach was applied to find the intragranular misorientation axes in 72 grains with different orientations, by finding the most broadened azimuthal projections grain-by-grain, considering the strain level $\varepsilon = 0.2\%$. It was found that the crystallographic direction of the global misorientation axis is strongly dependent on grain average orientation, as illustrated in Fig. 3.14.

We observed a high presence of boundaries with misorientation axes of <121> and <110> type near the 111 corner of the IPF, while some <111> boundaries are detected in grains for which the tensile axis is near their 101 direction. In the other zones of the stereographic triangle, complex boundaries with ω_α = <130> an <133> were detected, probably having a mixed tilt and twist character. However no GNDs were found in grains whose 001 direction is close to the tensile axis, this agrees with previous TEM studies [20] showing that only dislocation cells are present in grains with this crystallographic orientation. This result was confirmed by finding

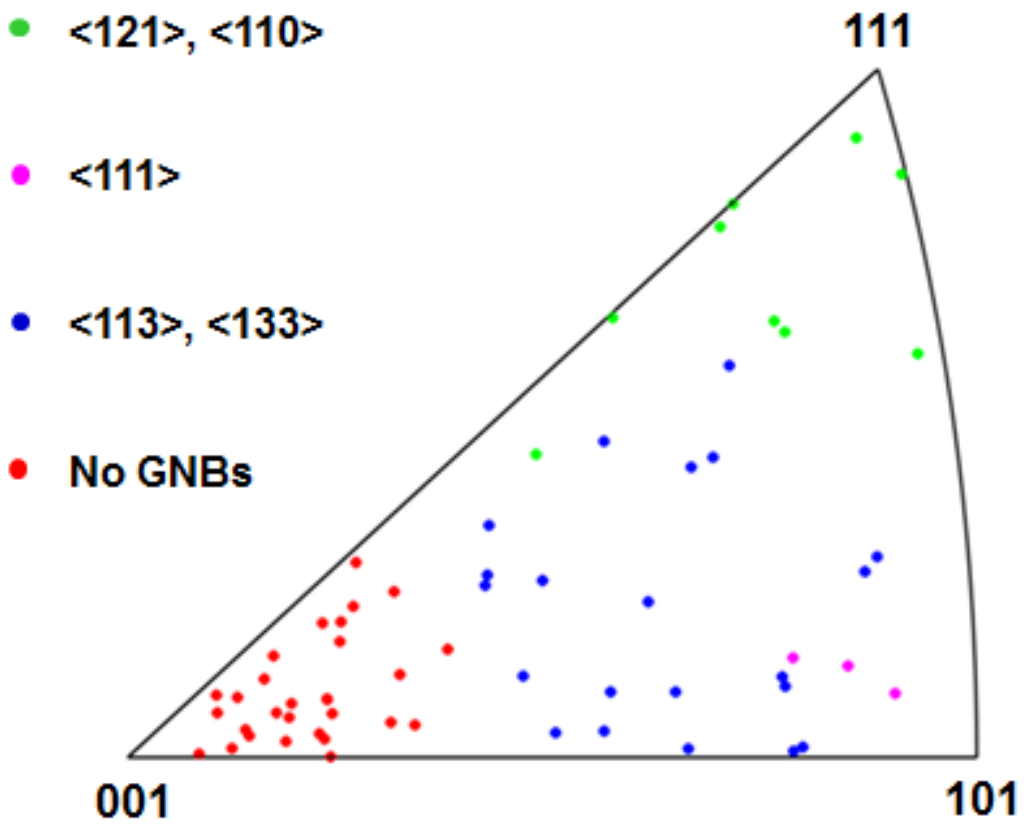

Figure 3.14 – *Stereographic triangle showing the dependence between the average orientation of 72 grains and the corresponding detected boundaries at the strain level $\varepsilon = 0.2\%$. Colours indicate the family of the crystallographic directions of the intragranular misorientation axes.*

a dependence between grain average orientation and broadening of the azimuthal projections of diffraction spots. Fig. 3.15 represents the inverse pole figure of the indexed grains of the scan corresponding to the strain $\varepsilon = 0.2\%$. Colours represent the value of the FWHM of the most broadened azimuthal projections for each grain, indicating that GNDs preferentially form near the 111 and 110 poles.

3.4 Evolution of the azimuthal intensity distribution with strain

By the 3DXRD technique, it is possible to track all diffraction spots at different scans, offering the opportunity to better understand the mechanisms that control the transformation of geometrically necessary boundary structures within grains.

3.4.1 Experimental observations

Analysing the change of the azimuthal intensity distribution through different strain levels can explain the evolution of GNBs under loading. In Fig. 3.16, the azimuthal projection of Grain A spot with reciprocal lattice vector $[\bar{3}11]$ is considered.

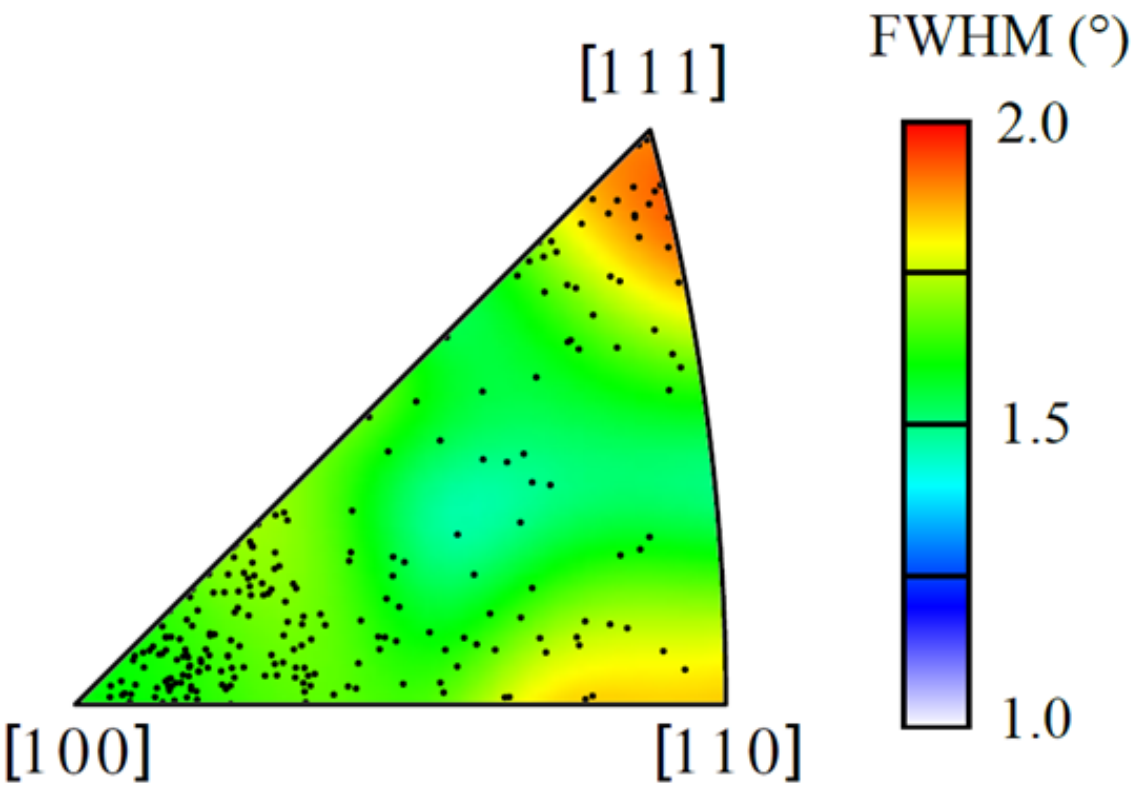

Figure 3.15 – *Stereographic triangle showing the dependence between the maximum FWHM value of the azimuthal projections for each grain and its average orientation (black dots), for the scan corresponding to the strain $\varepsilon = 0.2\%$. The FWHM values of this figure have a Gaussian smoothing of 4°.*

It can be seen that an elongated shape is preserved up to an applied strain value included between 1% and 3%, and the orientation spread increases, as the FWHM value increases. This is due to the increase of the number of geometrically necessary dislocations which form the wall, or to the creation of more boundaries. With further plastic deformation, the shape of the spot becomes more and more circular. Probably this represents the global effect due to the formation of new GNBs from other slip systems having a lower Schmid factor (activation of the multislip mechanism).

3.4.2 Evolution of the FWHM values

Geometrically necessary dislocation density variation is strictly linked to the evolution of FWHM values measured at different strain levels [64].It is quite interesting to analyse the FWHM evolution of the most broadened spots that come from the grains indicated in Fig. 3.8 (Grain A, Grain B, Grain C). Fig. 3.17 shows that the half-width broadening of azimuthal projections grows linearly with the highest resolved shear stress, which agrees with previous findings by Mughrabi et al. [64]. Physically, this means that geometrically necessary dislocations density increases linearly with the applied stress.

An unexpected result is that the FWHM has a non-zero value when the resolved

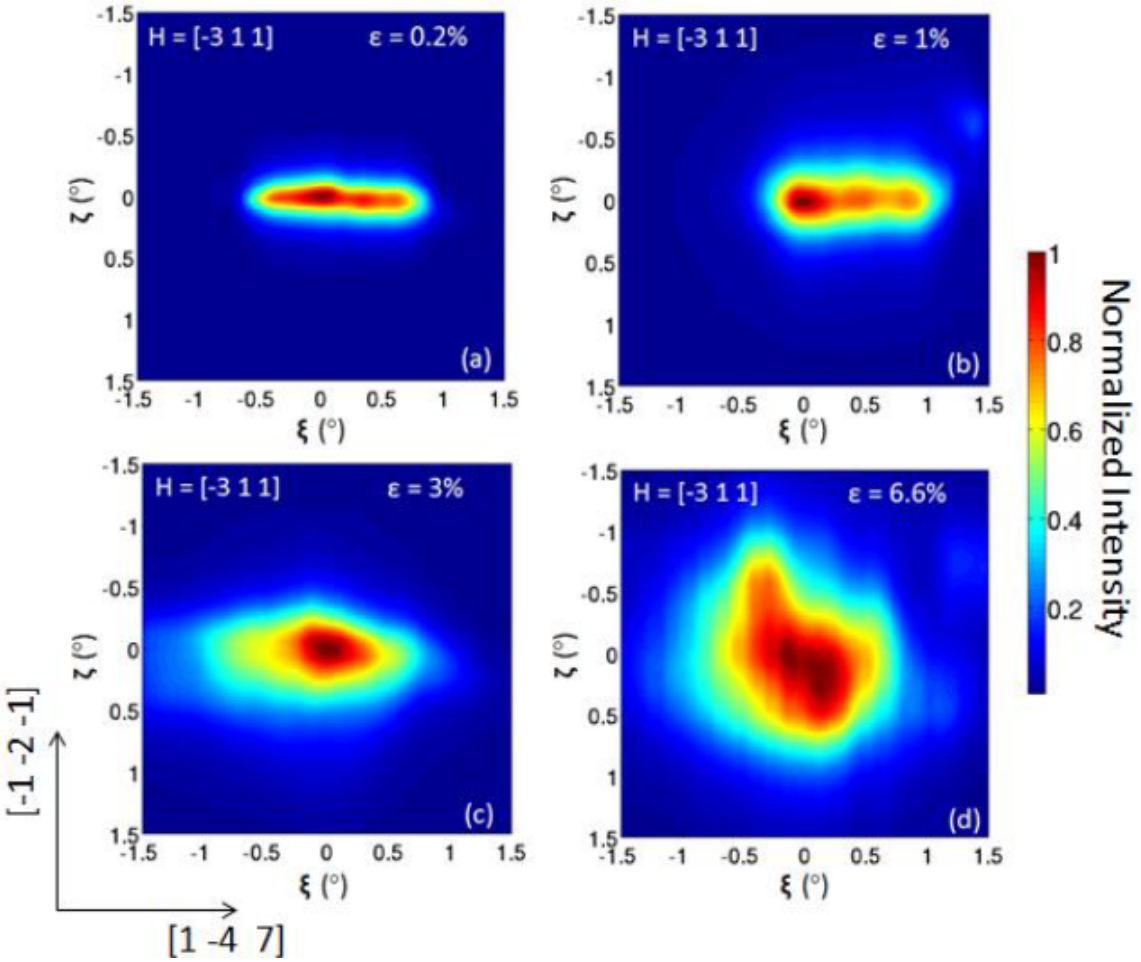

Figure 3.16 – *Evolution of the azimuthal intensity distribution of the spot $H = [\bar{3}11]$ belonging to the Grain A through different deformation levels. An elongated shape is conserved up to the strain $\varepsilon = 3\%$ (c). With further deformation, the shape becomes circular (d), indicating the activation of a multislip mechanism.*

shear stress is equal to zero. This can be attributed to a sudden increase of the geometrically necessary dislocation density at low stresses ($\tau \approx 3$ MPa), corresponding to the transition from stage I to stage II work hardening of single crystals [64].

3.5 Conclusions

A new method for in situ investigation of geometrically necessary boundaries in a polycrystalline Aluminium alloy is presented, which is based on the 3D X-Ray Diffraction technique. A stereographic triangle showing the rotational paths of 72 grains was shown, comparing the orientation paths with the predictions of the VPSC model and previous experimental data [65], obtaining satisfactory results with the exception of the area close to the 001 corner and near the 001-101 line. Poulsen and co-workers [66] tried to investigate the orientation spread within grains by means of a statistical analysis of FWHM values of diffraction spots in a ω-η plane, from which

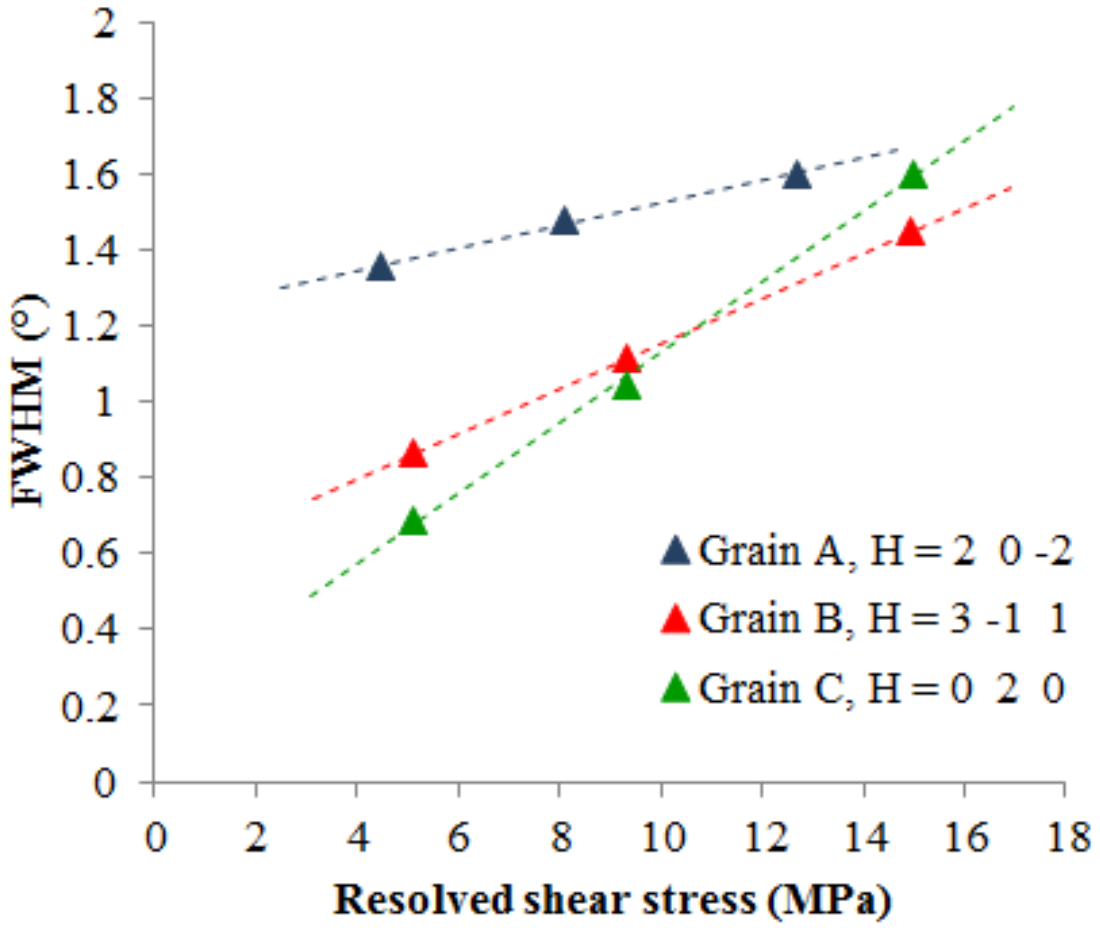

Figure 3.17 – *Azimuthal spread of the most broadened spots belonging to the grains A, B and C. FWHM evolution with the resolved shear stress was found to be linear between* $\varepsilon = 0.2\%$ *and* $\varepsilon = 3\%$*. FWHM values were corrected from the instrumental broadening.*

the presence of dislocation walls was deduced. Nevertheless, this approach does not provide the comprehension of the boundary structure: more adequate seems to be using a reference system fixed to the reciprocal space. The analysis of the reciprocal space maps of diffraction spots allows a grain-by-grain determination of the crystallographic rotation axis within single grains of a deformed polycrystal.

In this chapter, a full characterization of the misorientation axis and dislocation content of geometrically necessary boundaries was presented. This was possible through a coupled analysis of the intensity distributions in the azimuthal plane and Schmid factors to find the most stressed slip systems, which are supposed to be the sources of the dislocations forming the boundary. The reciprocal space maps of diffraction spots allow a full characterization of dislocation boundaries, provided that they are mainly composed of one type of dislocations. In this case, the broadening of the azimuthal projections of diffraction spots is maximal when the diffraction vector is perpendicular to the misorientation axis of the boundary [34], that agrees with our results of the grain A (Fig. 3.9). This effect was not observed in other grains, since the structure of dislocation boundaries is quite complicated even at

low strain. Nevertheless, the predominant misorientation axis arising in these grains can be correctly determined by analysing the two most broadened azimuthal intensity distributions. Dislocation wall type strongly depends on grain orientation, as the dislocation content is dependent on the active slip systems. GNBs were found to form at the early stages of plastic deformation (0.2% strain). Finally, the evolution of boundary structure under loading conditions was investigated, demonstrating that the dislocation content varies linearly with the applied strain and that other slip systems contribute to form new boundaries after a certain amount of plastic deformation. This kind of analysis overcomes the main disadvantage of the most traditional characterization tools, such as TEM and EBSD represented by their destructive nature.

Moreover, the 3DXRD analysis can be carried out for all grains belonging to the illuminated volume, which will representative for the bulk material. All these considerations are valid for Aluminium alloys, dislocation arrangements in other materials should be object of further investigations.

4 Study of grain subdivision by EBSD

Contents

In this chapter we present the evaluation of the predominant misorientation axes in single grains by EBSD, which has two purposes: a) cross check the results obtained by 3DXRD (see Section 3.3), by comparing grains with similar initial orientation, and b) describe the mechanisms of grain fragmentation, by evaluating the evolution of local misorientations within single grains, as a function of the imposed strain. For this purpose three specimens were used: the microstructure of the *Specimen A* was mapped at three deformation levels (0%, 1% and 5%), the *Specimen B* and the *Specimen C* were deformed at $\varepsilon = 5\%$ and $\varepsilon = 10\%$ respectively. The orientation maps of the regions of interest of the three samples are shown in Appendix A. Sample preparation and the acquisition parameters were described in Section 2.5.2.

4.1 Local misorientation measurements by EBSD

Previous studies showed that it is possible to correlate the magnitude of the plastic strain as well as the density of geometrically necessary dislocations with the spatial distribution of local misorientations, calculated as the angle between the local orientation and the average orientation of the grain [67–69]. Therefore, the determination of this disorientation distribution within a grain can provide a satisfactory understanding of the occurring deformation mechanisms and grain fragmentation.

An interesting question we want to answer is related to the dynamics of the formation of orientation gradients, by performing an EBSD scan over the same region of the sample deformed at different strains.

4.1.1 Onset of deformation-induced orientation gradients

As we saw in the previous chapter, geometrically necessary boundaries form at the beginning of macroscopic plastic deformation. By means of the disorientation maps of single grains at different strain levels, we expected to visualize the onset of intragranular orientation gradients at the early stages of plastic deformation, while finding out where grain subdivision starts and how it evolves. Disorientation maps of single grains, showing the misorientation angle between the local orientation and the average orientation of the grain, were obtained by using the Matlab Toolbox *MTEX* (http://mtex-toolbox.github.io).

Fig. 4.1 illustrates the disorientation maps of a grain of the Specimen A for different applied macroscopic strains (0%, 1% and 5%). The average orientation of the considered grain is defined by the Euler angles (86.14, 150.11, 205.15), following the Bunge convention, at the non-deformed state. The results that are presented for this grain can be extended to all grains of the Specimen A and Specimen B. The distribution of the disorientation angles of the considered grain for the three strain levels is shown in Fig. 4.2.

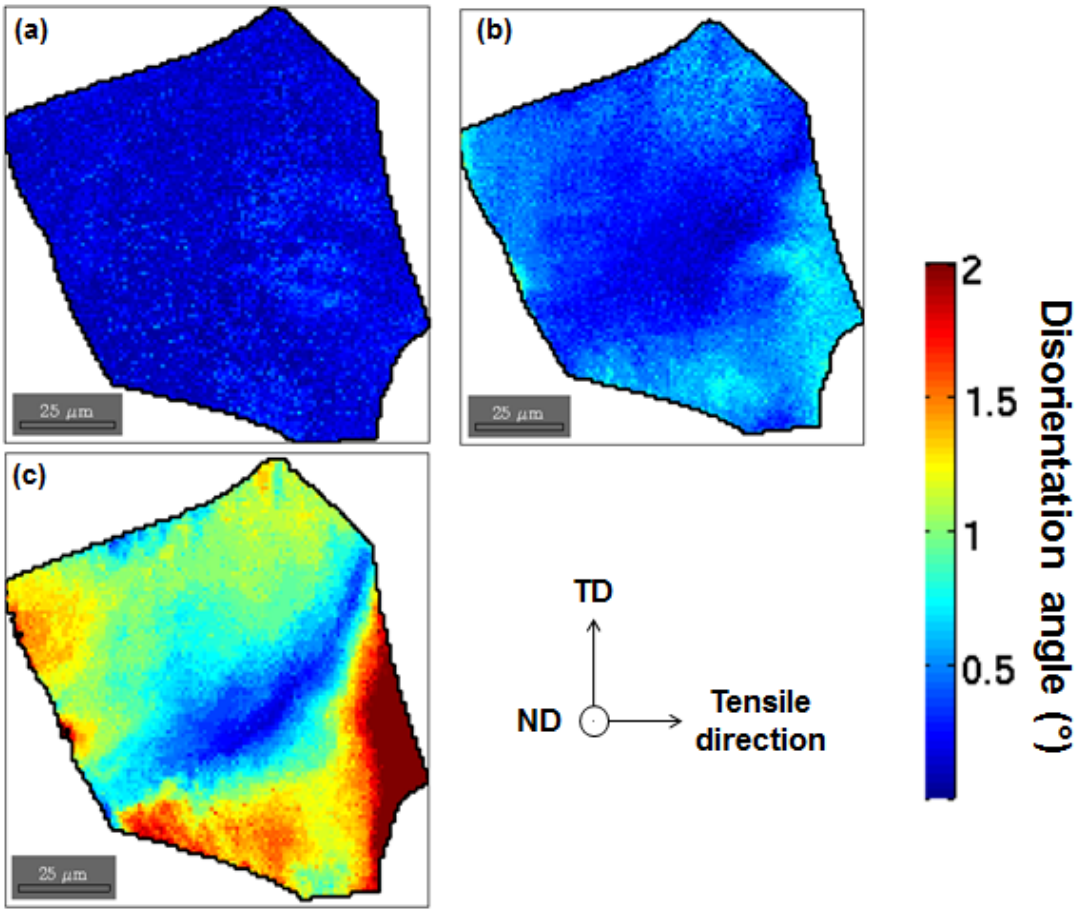

Figure 4.1 – *Local disorientation angle with respect to the average orientation of a grain of the Specimen A, at the non deformed state (a), and at the strain levels $\varepsilon = 1\%$ (b) and $\varepsilon = 5\%$ (c).*

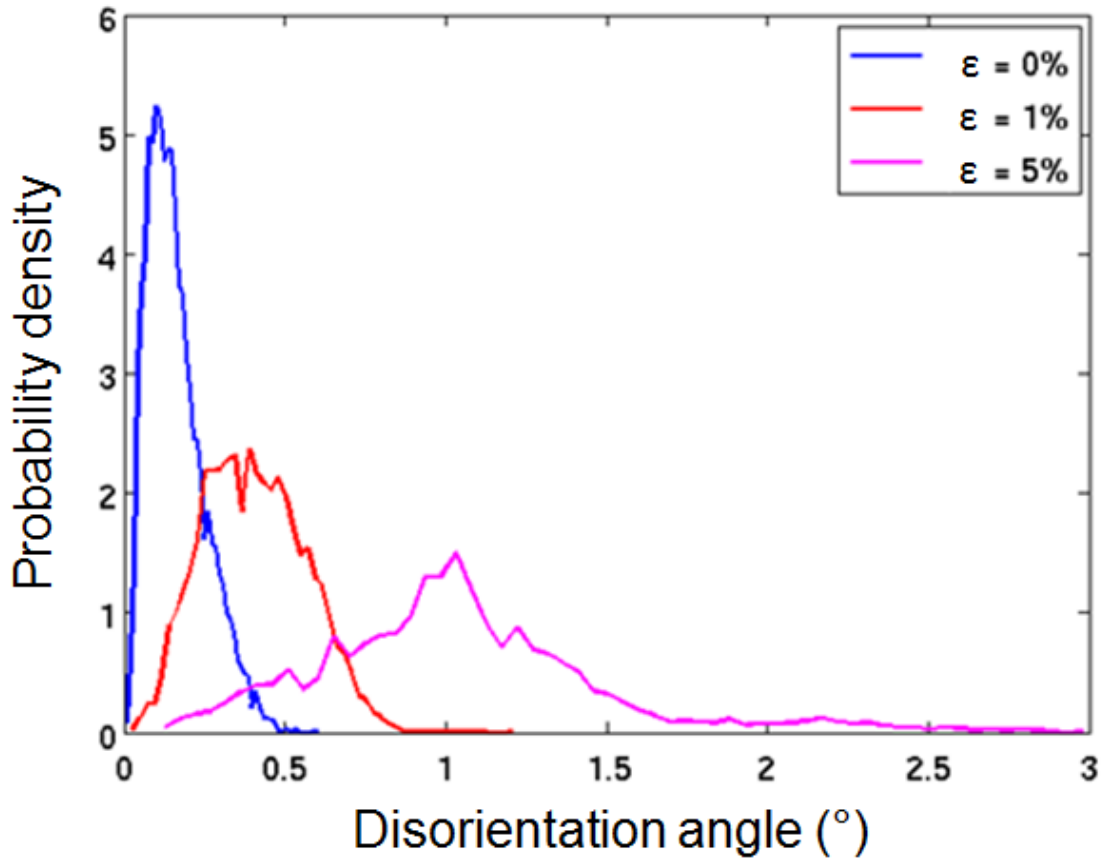

Figure 4.2 – *Distribution of the misorientation angles of the grain shown in Fig. 4.1 for each level of macroscopic deformation.*

In the recrystallized state the grain shows an uniform orientation, without any geometrically necessary boundary. At 1% deformation, gliding dislocations start to accumulate first near grain boundaries, giving rise to orientation spread. Grain boundaries were found to be the site where grain fragmentation starts, spreading out towards the centre of the crystal at 5% deformation, where a marked border between two disoriented regions forms.

4.1.2 Heterogeneity of local rotations within single grains

Disorientation maps only provide the scalar value of the misorientation angle between pixels orientation and grain average orientation. In order to visualize the directions of grain local rotations, single grain maps were built showing pixel disorientations as Rodrigues vectors. Such Rodrigues map can be shown as an image by assigning an *rgb* colour made of three variables for the red, green an blue channels, ranging from 0 to 255, according to the formula [57]:

$$\mathrm{RGB} = \frac{255 \times (\mathrm{R_i} + 2^{(1/2)} - 1)}{2 \times (2^{(1/2)} - 1)} \tag{4.1}$$

where R is the Rodrigues vector representing the disorientation vector between

pixels and average orientation of the grain, and the index $i \in \{1,2,3\}$ indicates the colour level for the corresponding channel. Fig. 4.3 shows the Rodrigues map of the grain deformed at $\varepsilon = 5\%$.

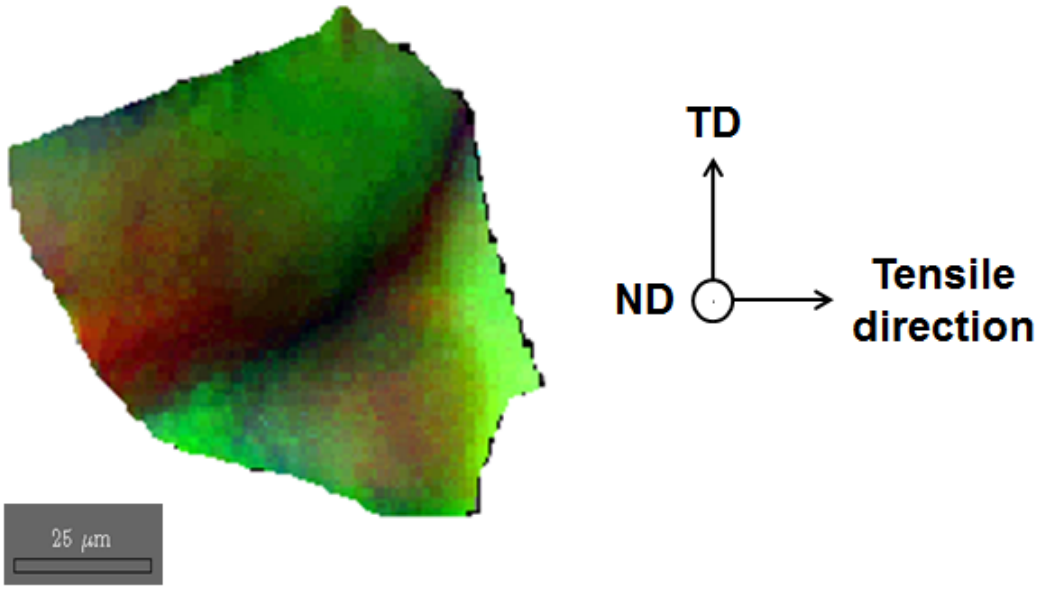

Figure 4.3 – *Rodrigues disorientation map of a grain belonging to the Specimen A, deformed at $\varepsilon = 5\%$. Colours represent the Rodrigues vector describing the disorientation between pixels and the average orientation of the grain.*

On the basis of Eq. 4.1, the red, green and blue colours represent local rotations around the [1 0 0], [0 1 0] and [0 0 1] directions in the crystal coordinate system, respectively. Fig. 4.3 clearly shows the formation of a low angle boundary separating two regions rotating around different axes.

A Rodrigues map of the investigated region of the Specimen B was built to verify the formation of marked subgrain structures at $\varepsilon = 5\%$ 4.4.

At a first sight, the image shows the presence of a great heterogeneity of disorientation axes within single grains. Rotations around different directions are present near grain boundaries. The change of the disorientation axis reveals a grain interaction phenomenon. This map also reveals the formation of regions with the same rotation axis inclined at about 45° with respect to the tensile direction.

4.2 Influence of the grain boundaries

The goal of this study is to understand the subdivision mechanism within single grains and the influence of grain boundaries by means of EBSD orientation maps. The intra-granular misorientation angle is a microstructural parameter that quantifies the long range order/disorder within grains in terms of crystallographic orientation [67]. On the other hand, geometrically necessary dislocations are mainly associated with orientation gradients. The question we try to answer in this section

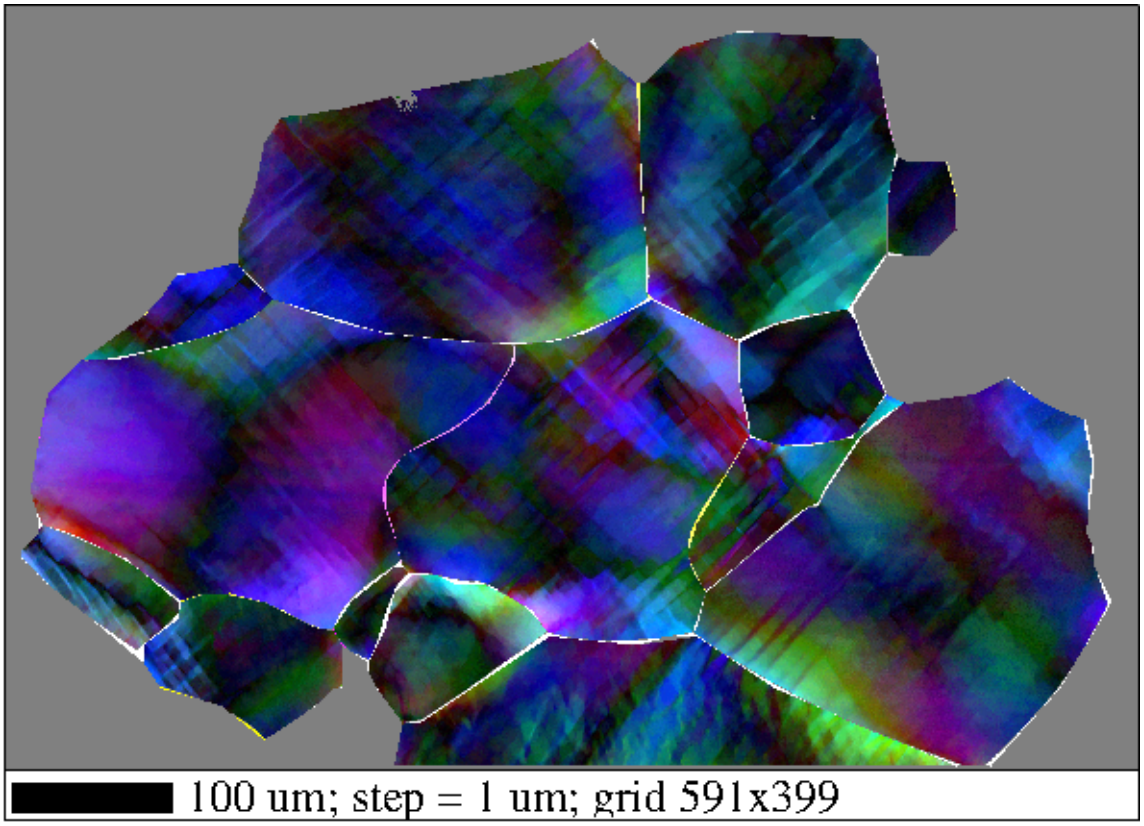

Figure 4.4 – *Rodrigues map of the investigated region of the Specimen B deformed by a tensile load along the horizontal direction. Colours represent the Rodrigues disorientation vector components between the local and the average orientation of grains in the crystal coordinate system.*

is related to the distribution of the orientation gradients arising in grains of the deformed polycrystal, that can be related to the spatial distribution of geometrically necessary dislocations.

4.2.1 Definition of the characteristic length

The disorientation maps of single grains of the Specimen A 4.1 showed that the orientation gradients within grains start from grain boundaries at low strains to gradually spread out towards the centre of the grain with further deformation. This reveals the accumulation of lattice defects near grains borders at low strains, an effect that was widely investigated in the literature.

To characterize it quantitatively, the dependence of local disorientation as a function of its distance from the nearest grain boundary has been studied. Fig. 4.5 shows the typical behaviour observed in all grains of the Specimen A and Specimen B, deformed at $\varepsilon = 5\%$. The graph shows the trend of the intragranular disorientation angle with respect to the distance from the grain boundary. The value of the distance was calculated as the *Euclidean distance* between each pixel belonging to the grain and the nearest grain boundary. Data are presented as the average value of

the intragranular disorientation angles, and the corresponding error bar represents the variability of the disorientation angle for equal distance from grain boundaries.

It is clear that the disorientation angle is higher for lower distances from the grain boundary, and both the average values and the corresponding standard deviations monotonically decrease for higher distances, towards the centre of the grain. This result agrees with previous findings by Pokharel and co-workers [67], who observed an increase of the disorder near grain boundaries of a tensile deformed copper polycrystal, by carrying out an in-situ experiment by the HEDM technique [70]. On the other hand, a numerical simulation based study [71], pointed out the link between such localised disorder and the density of geometrically necessary dislocations. Such association is logical, as grain boundaries act as obstacles to dislocation movement; therefore, gliding dislocations of the same sign tend to accumulate in these regions under form of pile-ups structures, causing local lattice rotations.

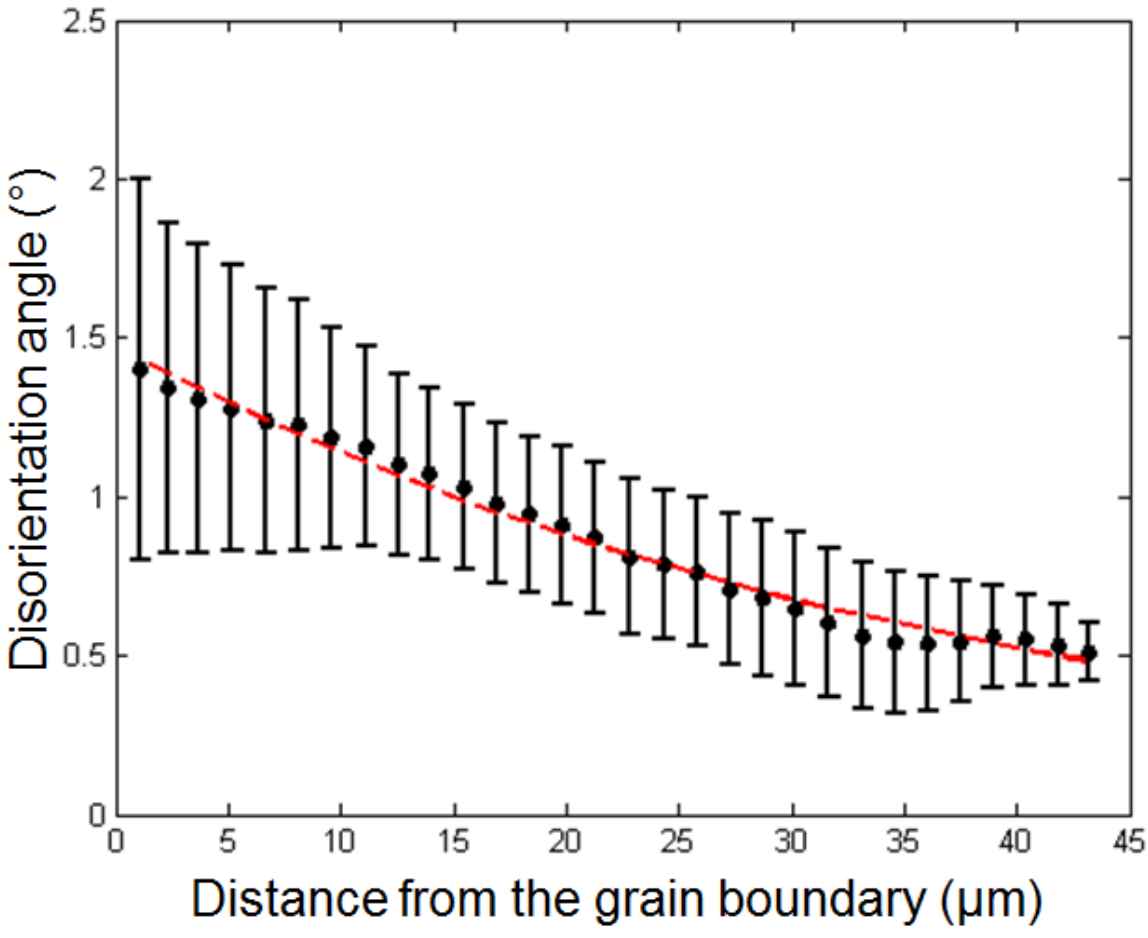

Figure 4.5 – *Trend of the misorientation angle with respect to the distance from the nearest grain boundary. Data are represented in terms of the mean value and the standard deviation. The dashed red line represents the exponential fitting curve of the average values.*

It is interesting to quantify the role that grain boundaries play in grain fragmentation, in order to investigate an eventual dependence on grain orientation and/or size. For this purpose, the disorientation angle average values shown in Fig. 4.5 were

fitted by an exponential function, marked as a red dashed line in the figure, having the form:

$$\Delta\Theta = \mathrm{A} \cdot \exp(-\mathrm{d}/\lambda) \tag{4.2}$$

where $\Delta\Theta$ is the disorientation angle, A the amplitude of the exponential function and d the euclidean distance between a pixel and the nearest grain boundary. In this expression, λ can be seen as the *decay rate* of the exponential function. From a physical point of view, this value represents a *characteristic length* of the influence of the grain boundary in grain subdivision.

All the investigated grains of the Specimen A and Specimen B, deformed up to $\varepsilon = 5\%$ show a behaviour which is well described by Fig. 4.5. When increasing the macroscopic deformation to $\varepsilon = 10\%$, the deformation mechanism of single grains is slightly different. Figures 4.6 and 4.7 illustrate the disorientation map and the trend of the disorientation angle with respect to the distance from the grain boundary for a grain of the Specimen C, respectively. Although the effect of the grain boundary is still visible, its influence is weaker if compared to the case of the two specimens deformed at $\varepsilon = 5\%$. Fig. 4.7 shows that the value of the disorientation angle suddenly decreases at a low distance from the boundary, giving a lower value of the characteristic length in comparison to the previous case. A few microns far from the boundary, the disorientation angle attains a constant value, that is a sign of the homogenisation of grain deformation.

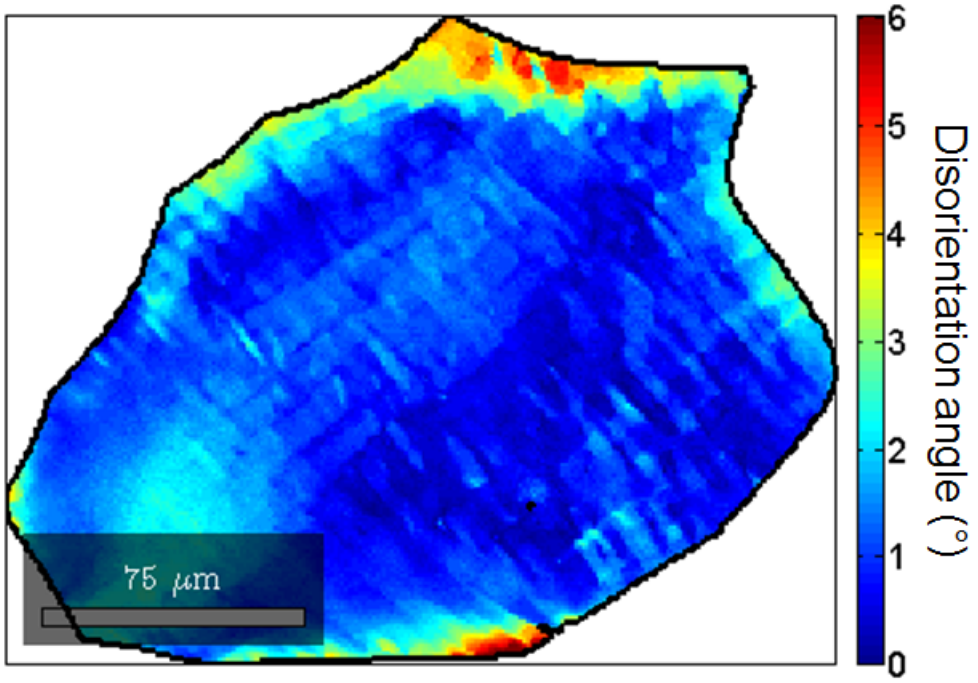

Figure 4.6 – *Grain orientation spread map of a grain of the Specimen C, deformed at* $\varepsilon = 10\%$.

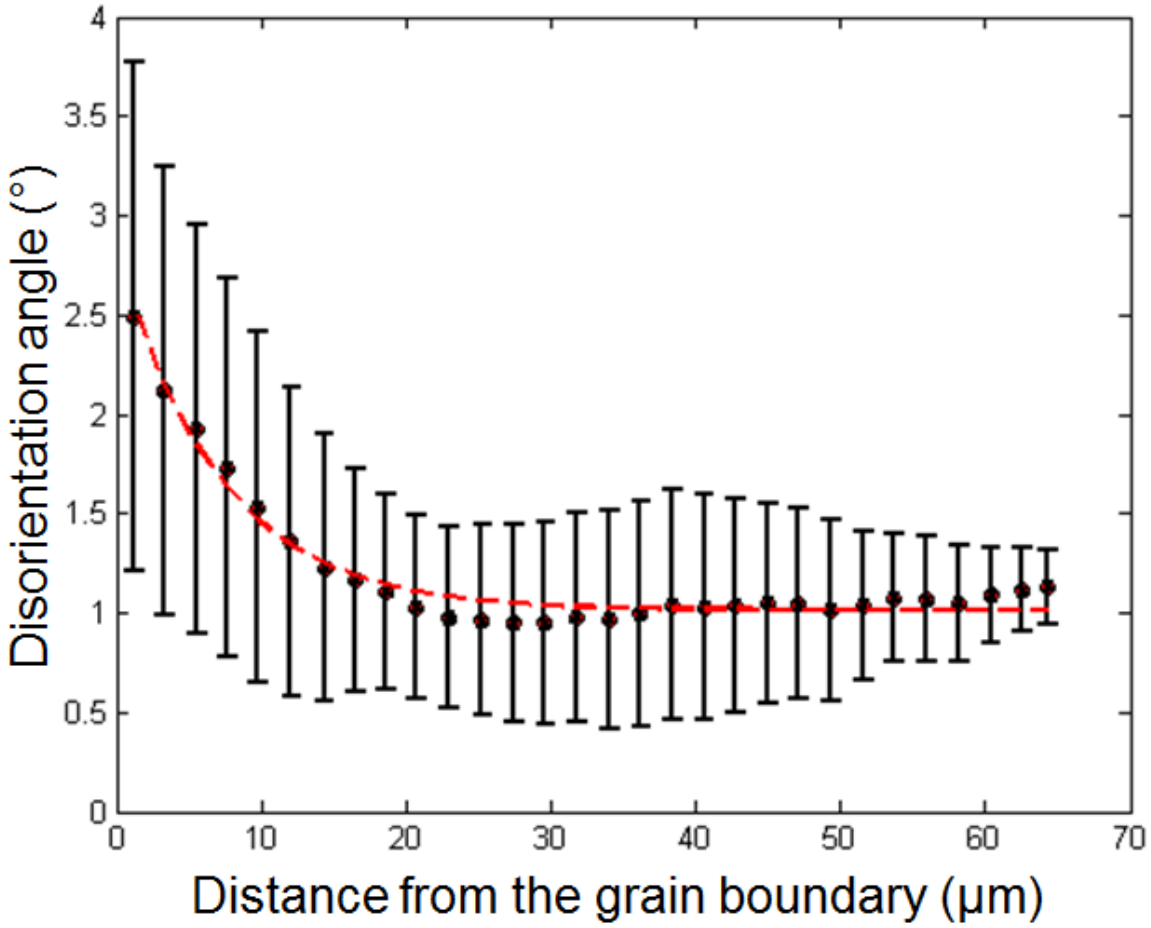

Figure 4.7 – *Trend of the misorientation angle as a function of the distance from the grain boundary calculated from the disorientation map of the grain shown in Fig. 4.6*

4.2.2 Influence of grain size and average orientation

The determination of the characteristic length by means of Eq. 4.2 allows to quantify the role played by grain boundaries in grain subdivision. For Specimen A and Specimen B, both deformed at $\varepsilon = 5\%$, it was found that grain boundary influence depends on grain size. Fig. 4.8 shows the trends of the characteristic length as a function of the square root of grain area (μm), for the two specimens. Only those grains for which the exponential fit gives a value of $R^2 > 80\%$ were considered for this analysis.

One can note that the global trend is linear: the characteristic length increases monotonically with grains area, with a smaller dispersion for smaller grains.

Although the correspondence between grain size and characteristic length seems quite logic, an interesting result to retain is related to the influence of grain boundaries on grain rotation is much more evident in small grains rather than in larger domains.

The eventual correlation between $\frac{\lambda}{D}$ and grain average orientation was also checked, where D represents grains equivalent diameter. Fig. 4.9 shows the average

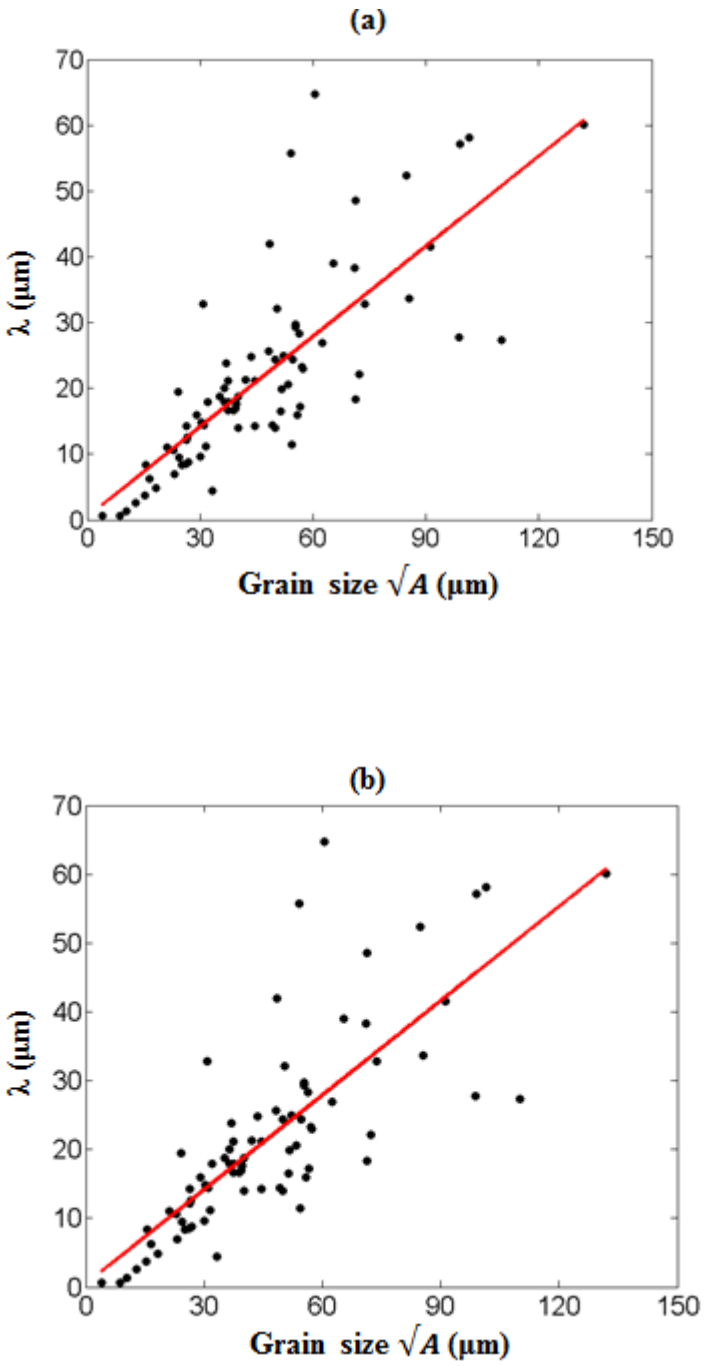

Figure 4.8 – *Correlation between the characteristic length and the grain area for (a) the Specimen A and (b) the Specimen B, both deformed at* $\varepsilon = 5\%$.

orientation of the grains of the Specimen A deformed at $\varepsilon = 5\%$ represented in a stereographic triangle. The colour map associates grain orientations with the calculated value of λ within a certain interval. One can note that no correspondence was found, revealing that the amount of deformation near grain boundaries is not controlled by the average orientation, but more probably by the interaction with neighbouring grains.

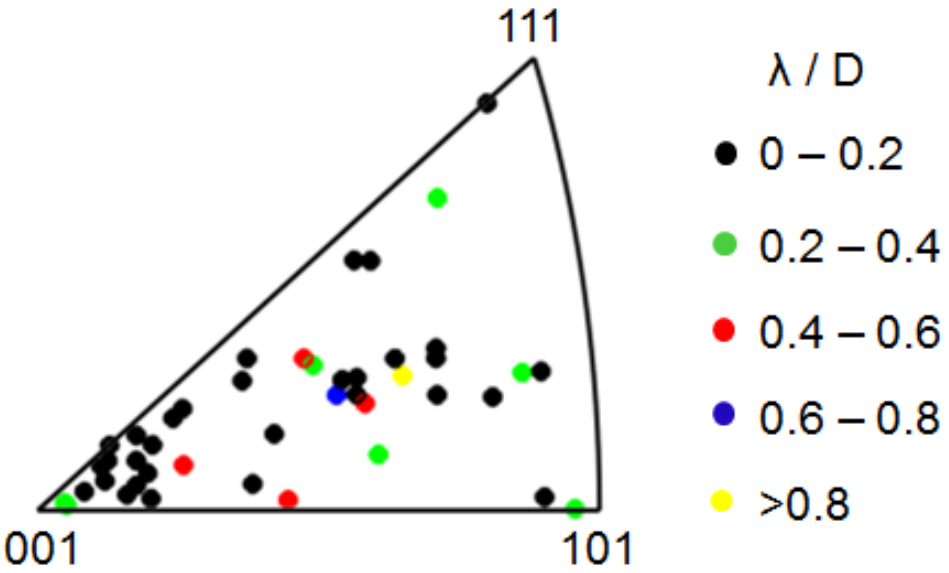

Figure 4.9 – *Correlation between the ratio* $\frac{\lambda}{D}$ *and grains average orientation for the Specimen B. To reduce the number of points within the IPF, only those grains giving a value of* $R^2 > 90\%$ *for the exponential fit were considered.*

4.3 Determination of the predominant misorientation axis in single grains

The knowledge of the local orientation of single grains leads to the characterization of local rotations induced by deformation. In particular, the evaluation of the predominant, or global, misorientation axis within grains through the procedure described below, gave us the opportunity to validate the results obtained by 3DXRD, pointed out in the previous chapter.

4.3.1 Local orientation analysis procedure

The characterization of grain orientation spread was carried out by calculating the pixel-by-pixel disorientation with respect to the average orientation of the considered grain. The 3X3 matrices representing these disorientations can be expressed as Rodrigues vectors, having the form:

$$\vec{R} = \tan(\theta/2)\vec{r} \tag{4.3}$$

where $\vec{r}$ is the unit vector of the rotation direction and θ is the rotation angle. The orientation manipulation formulae are listed in the *orilib* documentation [72].

The Rodrigues vector formulation allows the characterization of the predominant misorientation axis through the procedure described by Glez and Driver [73]. The approach consists in representing the Rodrigues disorientation vectors in the *Rodrigues fundamental zone* by considering crystal symmetries. Here, grain orienta-

tion spread results in an ellipsoidal shape, represented by a 3X3 covariance matrix. The eigenvectors give the principal directions of the ellipsoid, and the corresponding eigenvalues are proportional to the amplitude of the dispersion around these axes. The principal direction of maximum elongation of the ellipsoid coincides with the predominant misorientation axis within the grain, provided that the Rodrigues fundamental zone is related to the *crystal coordinate system*.

4.3.2 Comparison with the 3DXRD results

The determination of the principal axis of the orientation ellipsoid in the Rodrigues fundamental zone allows to cross check the predominant misorientation axes calculated by 3DXRD. Although the measurements were carried out on different samples, the comparison is applicable for grains with similar orientation with respect to the tensile direction, since the activated slip systems and the slip amounts are expected to be similar.

The Table 4.1 shows a comparison between eight pairs of grains with similar orientation chosen from Specimen A and the sample scanned by 3DXRD. For this comparison, we considered the acquisitions with an applied deformation of $\varepsilon = 1\%$ which was applied to both samples. One can note that the results obtained by the two techniques match for six pairs, the difference of sign is uniquely due to crystal symmetry.

For the pairs 4 and 8, the two techniques provide two completely different values of the predominant misorientation axis: for these grains, we observed a Rodrigues ellipsoid with a low eccentricity, which can reveal a multislip activity. This was not observed by 3DXRD, where the corresponding azimuthal intensity maps of diffraction spots were broadened along one crystallographic direction and not circular. This means that the mechanism of formation of geometrically necessary boundaries is not always controlled by the average orientation of these grains, but there is also an influence of neighbouring grains.

4.4 Conclusions

In this chapter we presented an EBSD characterization of the deformation mechanism of single grains in a tensile deformed Aluminium alloy. Through the construction of the disorientation maps of deformed grains, we observed that deformation starts from grain boundaries. The average local disorientation decays exponentially towards the centre of the grain, confirming that lattice planes bend more near grain boundaries, as supposed by the Toth model [46]. The definition of a characteristic length that quantifies the influence of grain boundaries in grain fragmentation allowed to point out that the deformed region of the grain around the boundary is

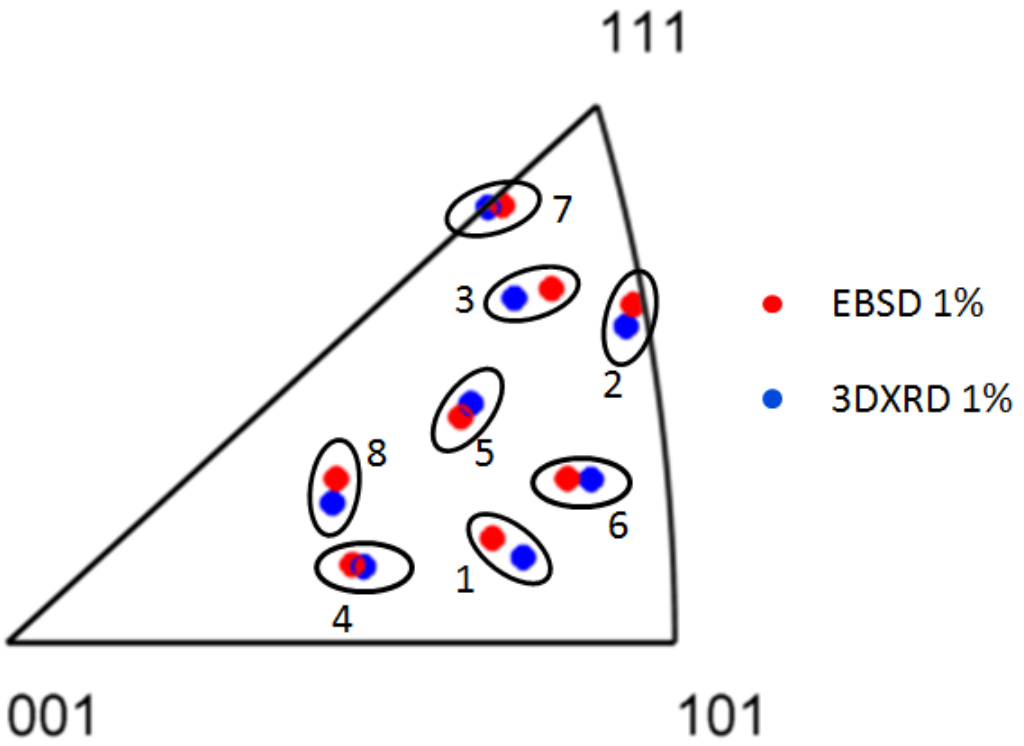

Table 4.1 – *Comparison between the predominant misorientation axes calculated for 8 pairs of grains with similar average orientations by EBSD and 3DXRD. The specimens were both deformed at* $\varepsilon = 1\%$.

Label	Misorientation axis EBSD	Misorientation axis 3DXRD
1	$[\bar{6}\bar{5}6]$	$[\bar{1}\bar{1}1]$
2	$[47\bar{7}\bar{4}]$	$[121]$
3	$[121]$	$[121]$
4	$[\bar{4}76]$	$[3\bar{1}1]$
5	$[\bar{1}\bar{3}0]$	$[\bar{1}\bar{3}0]$
6	$[321]$	$[331]$
7	$[485]$	$[\bar{1}21]$
8	$[010]$	$[31\bar{3}]$

larger for bigger grains and without any dependence on their average orientation. Moreover we found that when increasing the deformation, the value of the characteristic length decreases, showing that a distortion/strain homogenization mechanism takes place.

The grain-by-grain analysis allowed to cross check the results obtained by 3DXRD. The representation of local orientations in the Rodrigues fundamental zone allowed to calculate the predominant misorientation axis in single grains, that was compared to the calculation performed by 3DXRD for grains with a similar average

orientation, obtaining a satisfactory match. This is a supplementary confirmation that 3DXRD is a promising technique for the in-situ characterization of deformation induced orientation gradients of single grains of a polycrystal. Nevertheless, the spatial characterization of intragranular strains by EBSD is quite impossible; this can be achieved by the K-map technique [58] which is presented in the next chapter.

5 Evaluation of intragranular strain in single grains using K-map scanning

Contents

The critical parameter connected with the safe operation of engineering components is the stress, which by exceeding a given threshold can lead to damage. In single grains of polycrystalline materials, it was found that stress concentrates near grain boundaries, which become therefore preferential sites for damage initiation [74]. Hence, characterization of local strain/stress by diffraction methods is of high industrial and academic importance. In particular, X-Ray diffraction microscopy is a non-destructive technique which is sensitive to the variation of the lattice parameter of the microstructure, and can be used for *in situ* experiments.

In this chapter, we present a first attempt to investigate grain subdivision by the recently developed K-map technique [58]. This novel scanning X-Ray technique was applied to characterize intragranular strains in a single grain of an Al-0.1wt.%Mn polycrystal deformed in tension up to 0.5% strain.

The main questions we want to answer are related to the properties of the residual strain distribution and to its physical origin, which evidently should be related to the dislocations produced during the plastic deformation.

5.1 Cross correlation

The comparison between the EBSD and XRD data requires a careful analysis since, due to the higher penetration depth of X-Rays with respect to electrons, XRD also gives information about hidden regions of the scanned grain that can be located below the grain boundary shown by EBSD. The penetration of 8 keV X-

rays in Al corresponding to the $11\bar{3}$ reflection is in fact about 46 μm, that is much higher than the penetration of 20 keV electrons. A previous study [75] showed the similarity between the calculation of the lattice tilts by the two technique, which suggested the use of a cross correlation procedure to match the two datasets. The Pearson correlation algorithm was performed on a region of interest of 100 µm x 100 µm chosen at the centre of the EBSD image. The calculated tilt angles were normalized for the two datasets, and the region of interest of the EBSD map was displaced and rotated onto the XRD map in order to find the location giving the highest correlation coefficient, that is defined as:

$$\rho_{\mathrm{x,y}} = \frac{\mathrm{cov(X,Y)}}{\sigma_{\mathrm{x}}\sigma_{\mathrm{y}}} \tag{5.1}$$

where σ_x and σ_y are the standard deviations of the datasets X and Y. Only K-map data points having intensity higher than 0.7% of the maximum intensity were analysed.

5.2 Evaluation of lattice tilts and intragranular strain

The lattice tilt angles α_x and α_y (the angle between the average $\vec{Q}_{11\bar{3}}$ and the local Ox and Oy component respectively) where calculated for K-map and EBSD data. For the latter method, tilt angles were calculated following the algorithm presented by Borbély et al. [75].

Fig. 5.1 and 5.2 show the comparison between the resulting tilt maps. Concerning the α_y component, both images show vertical orientation bands with alternating opposite tilts. The tilt component α_x is completely different from α_y, but the similarity between K-map and EBSD results is still visible.

XRD and EBSD images have the same colour scale, this shows that the lattice tilts in surface near regions seen by EBSD is larger than the tilt obtained from XRD. This agrees with previous results obtained on single crystals [76], showing that lattice tilt is larger near the free surface.

The K-map images show that there is some signal coming from a region that is external to the grain boundaries observed by EBSD. It is important to remark that this signal comes from the same grain that extends below the thin surface film observed by the scanning electron microscope. Fig. 5.3 illustrates that the misorientation between the average orientations of the considered grain and the neighbours is higher than 10°, that is high enough to ensure the absence of diffracted X-Rays coming from these grains with the actual configuration.

The intragranular strain is related to the variation of the lattice parameter a and consequently to the variation of the interplanar spacing d_{hkl}. The directional strain $\epsilon_{11\bar{3}}$ was calculated by considering the local variation of the spacing between the

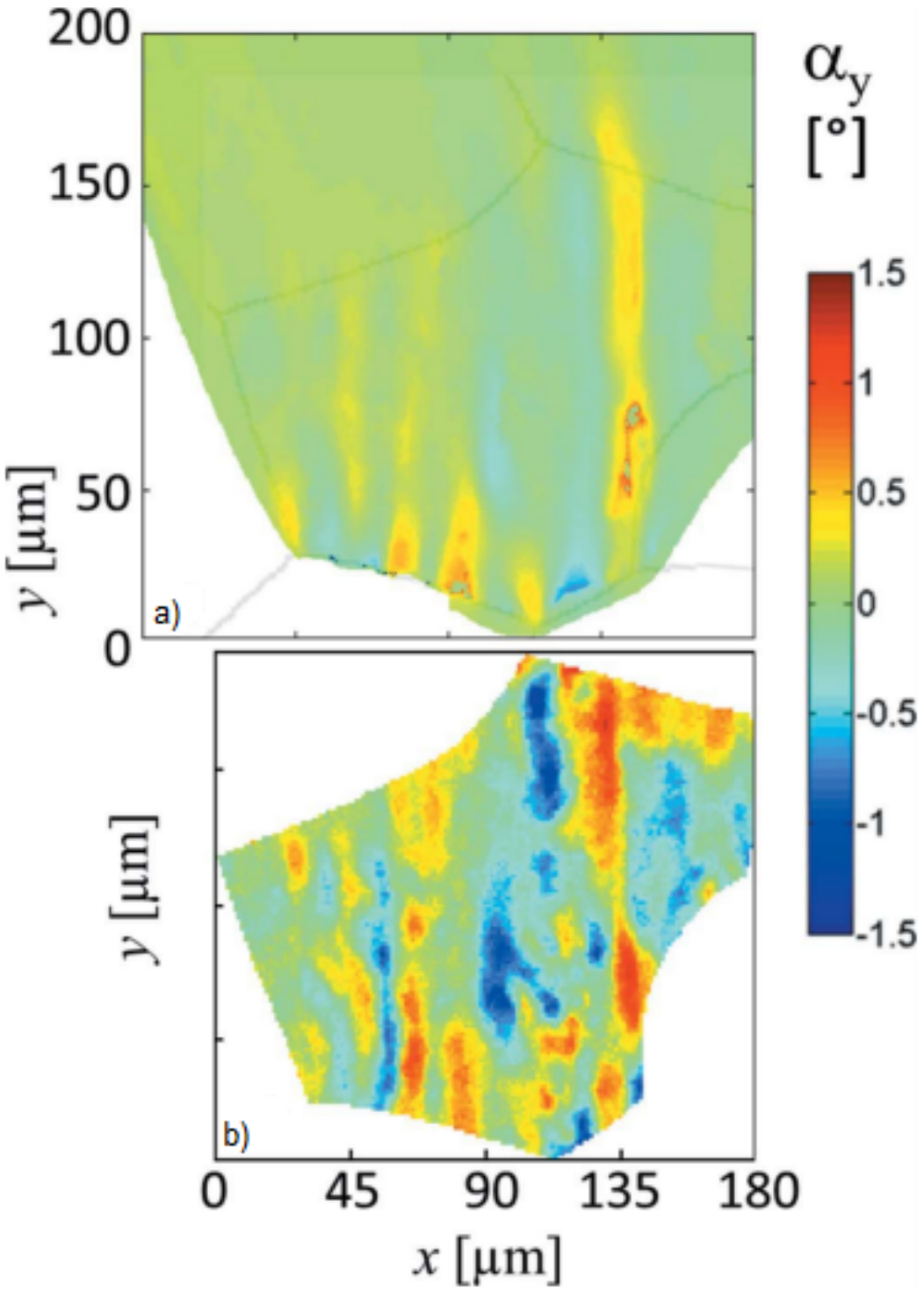

Figure 5.1 – *Distribution of the Oy component of lattice tilt α_y (the angle between the local Q_y component and the average value of $\vec{Q}_{11\bar{3}}$ over all pixels) calculated from a) K-map rocking curves and b) EBSD.*

$(11\bar{3})$ lattice planes, as shown by the Eq. 5.2:

$$\epsilon_{11\bar{3}} = \frac{\mathrm{d}_{11\bar{3}} - \mathrm{d}_{11\bar{3},\mathrm{mean}}}{\mathrm{d}_{11\bar{3},\mathrm{mean}}} \tag{5.2}$$

where $d_{11\bar{3},mean}$ is the reference value of the interplanar spacing, considered here as

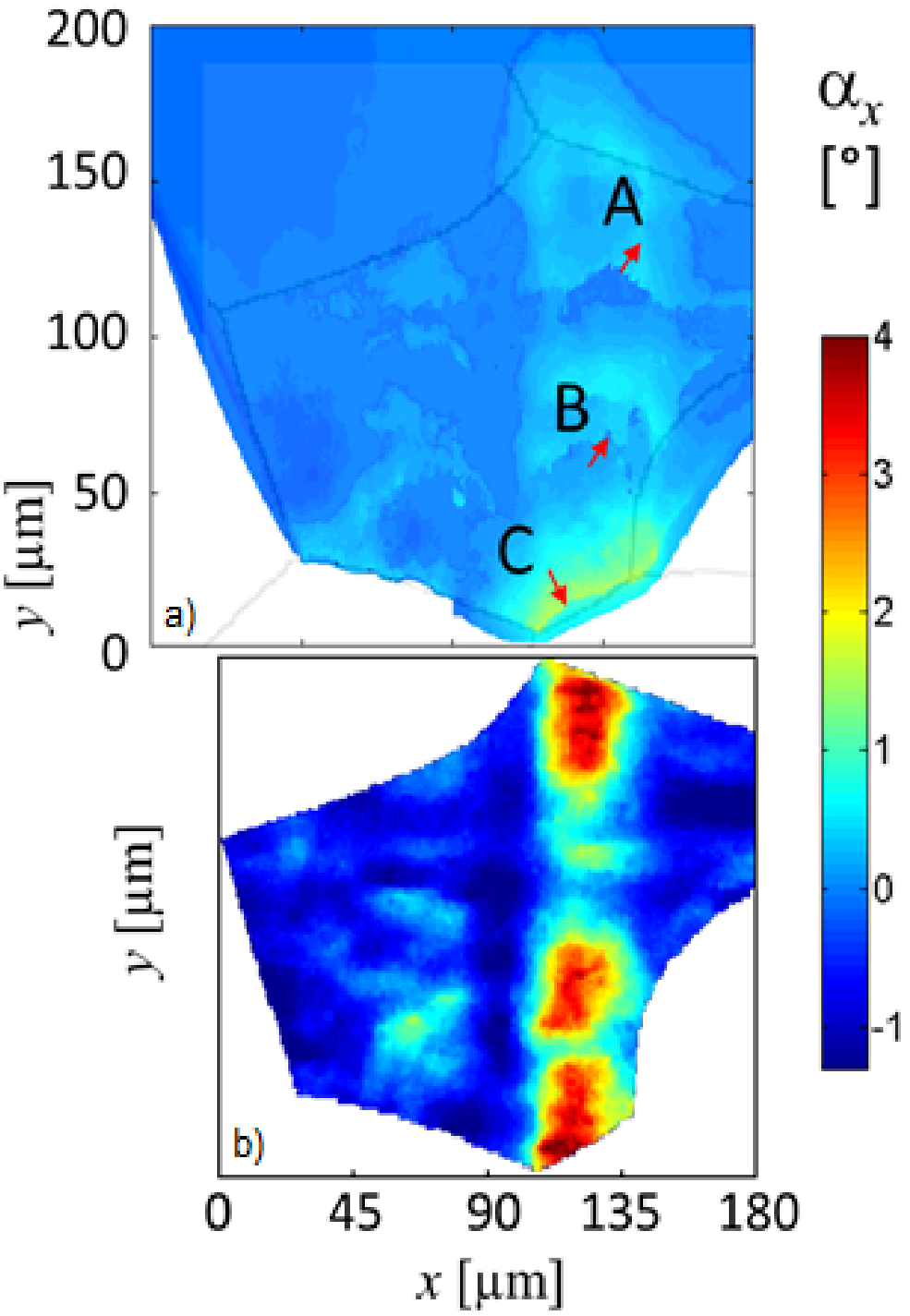

Figure 5.2 – *Distribution of the Ox component of lattice tilt α_x, (the angle between the local Q_x component and the average value of $\vec{Q}_{11\bar{3}}$ over all pixels) calculated from: a) K-map rocking curves and b) EBSD. The red arrows indicate the regions of high tilt gradient.*

the average calculated over the whole grain, and $d_{11\bar{3}}$ is the local interplanar spacing resulting from the measurement and calculated as:

$$\mathrm{d}_{11\bar{3}} = \frac{2\pi}{\mid \mathrm{Q}_{11\bar{3}} \mid} \tag{5.3}$$

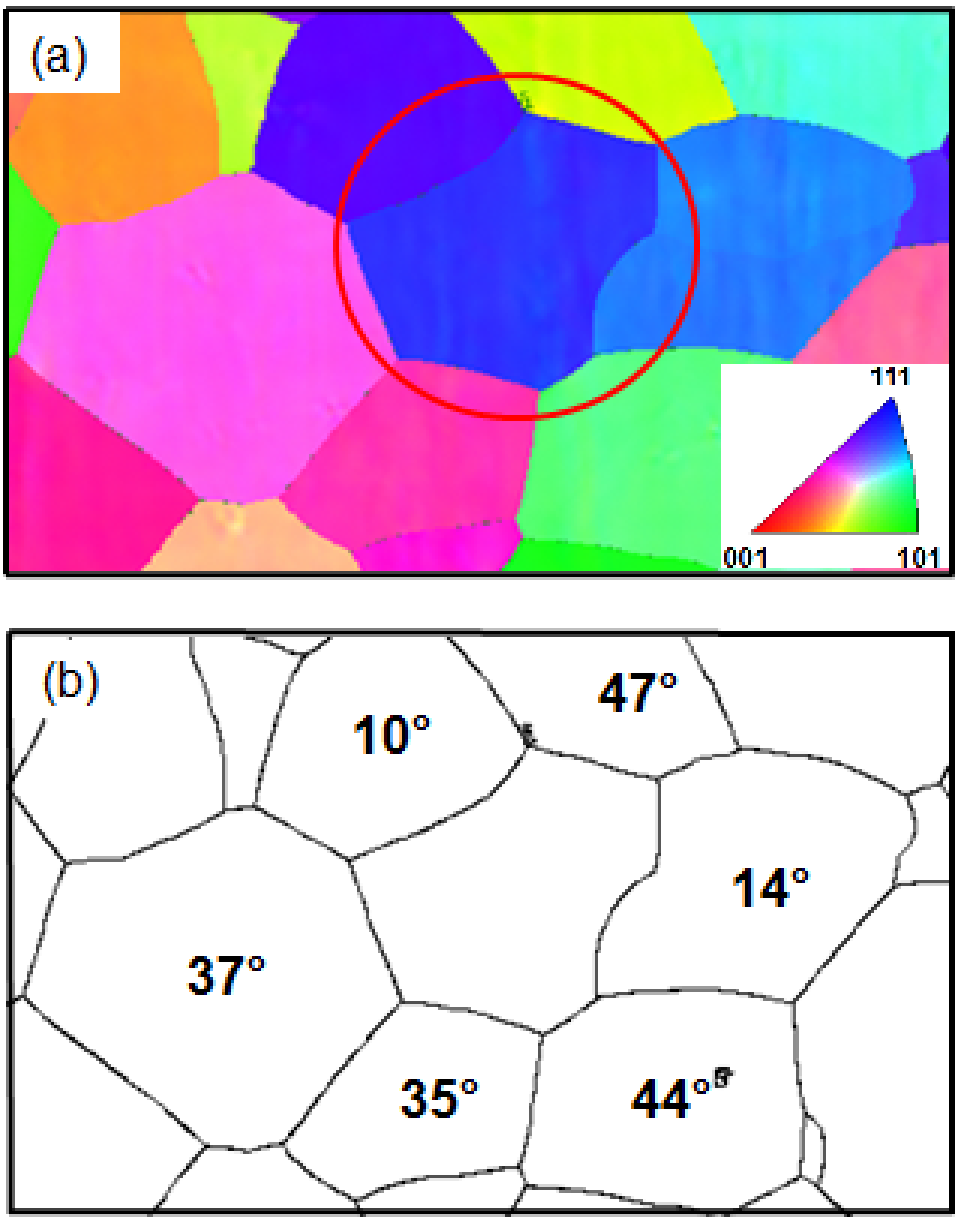

Figure 5.3 – *(a) IPF colour map of the region containing the scanned grain, and (b) misorientation angles between the average orientations of the investigated grain and the neighbouring grains. The selected grain is circled in red.*

Fig. 5.4 illustrates that the largest negative strains ($\sim -8x10^{-4}$) are located at the interior of the grain (region marked by A and B), while the largest positive strains ($\sim 7 \times 10^{-4}$) were found near grain boundaries (region marked by C). Regarding the stress field, if we consider an uniaxial tensile stress state and a Young modulus of 66 GPa, we obtain a maximum stress of 46 MPa, which is about three times the macroscopic flow stress at 0.5% strain. One can note the high strain gradients near the regions of large strain, which are marked by red arrows in Fig. 5.4. It is hypothesised that these large strains are caused by dislocation pile ups near grain boundaries and at obstacles at the interior. Nevertheless, since the tilt component

α_x shows high gradients in correspondence of such regions, we can assume that these obstacles are represented by polarized dislocation structures, such as geometrically necessary boundaries. A pertinent proof of this assumption can only be obtained by calculating the strain tensor, that would require at least five K-map scans with different diffraction vectors.

Complex strain distributions are visible near some triple junctions, for example at T_{12} where its sign changes form negative (in the vicinity of grain G1) to positive (close to G2). At T_{23} and T_{34} the strain is dominantly positive, while at T_{56} and T_{61} is close to zero.

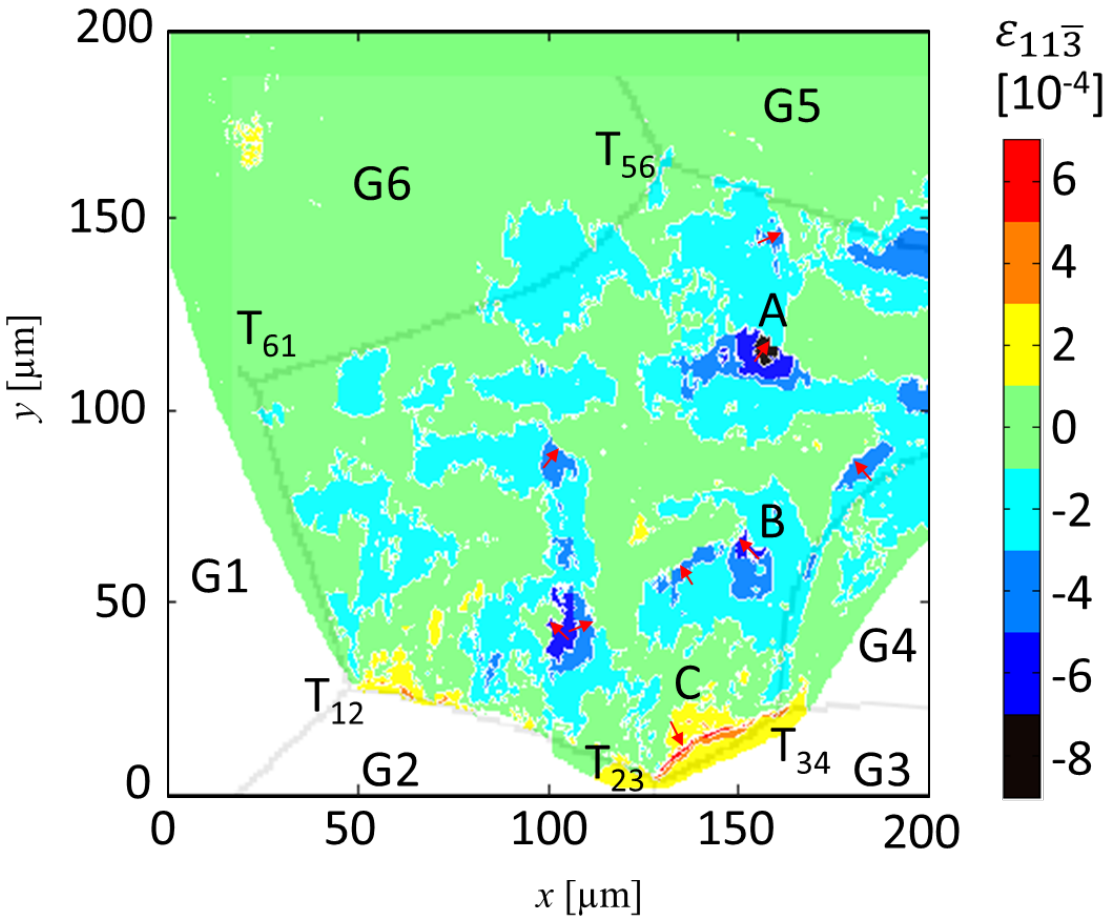

Figure 5.4 – *Distribution of the directional strain $\epsilon_{11\bar{3}}$ obtained from K-map with superposed EBSD grain boundaries*

5.3 Evaluation of the average dislocation density within the grain

The line-profile of the grain was obtained by plotting the histogram of the modulus of the diffraction vector $\vec{Q}_{11\bar{3}}$ in a logarithmic scale, as shown in Fig. 5.5. The resulting profile is asymmetric and shows typical cut-offs at small and large

magnitudes. The cut-offs, correspond to strains of about $\pm 7x10^{-4}$ and should be attributed to the finite size of the microbeam integrating over all d values in the irradiated volume of about 0.12 x 0.2 x 74 μm^3 (the penetration depth of the 8 keV X-rays at the diffraction angle $\Theta = 38°$ is of about 46 μm). The cut-off effect was also visible on the high-resolution EBSD results of Jiang et al., (2013) [77], where however, due to the smaller diameter of the electron beam a larger cut-off value in strain is expected. The physical origin of the residual strain can be deduced from the shape of the peak profile as shown by Groma [78]. The dislocation model of line-profile broadening assumes that the tails of the peak decay as a function of q^{-3}, where q is defined as the distance in the reciprocal space from the peak centre:

$$\mathrm{q} = 2(\sin(\theta) - \sin(\theta_0))/\lambda \tag{5.4}$$

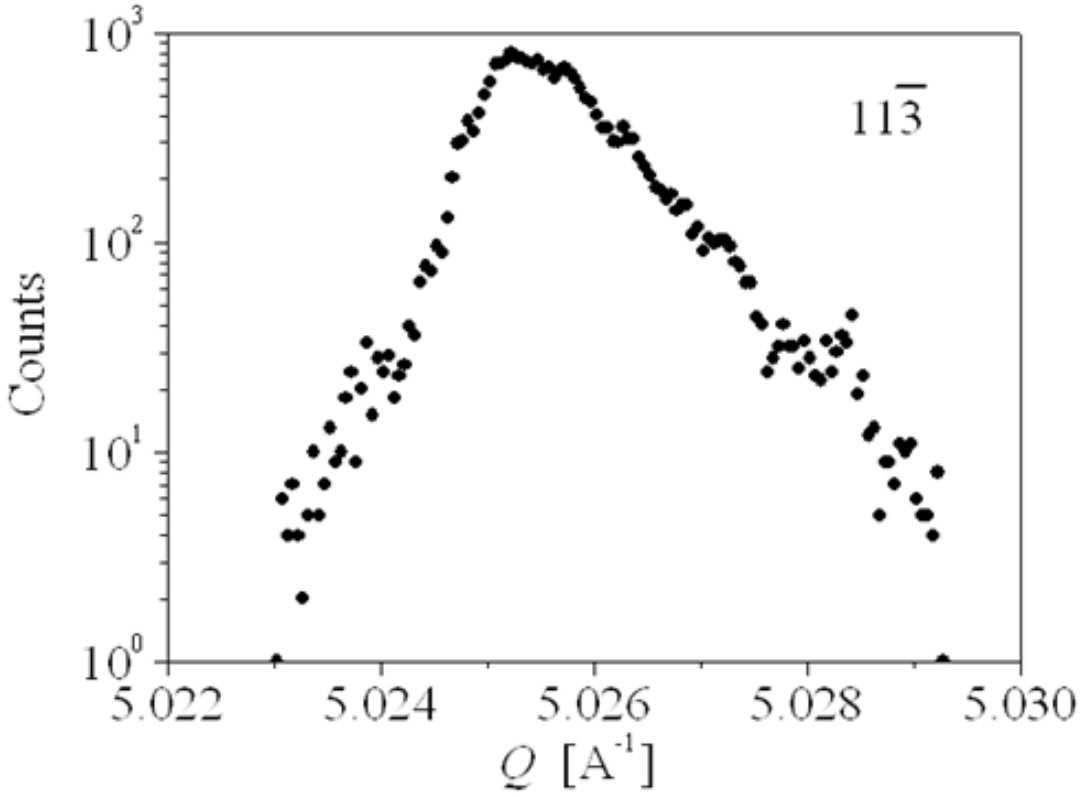

Figure 5.5 – *Distribution of diffraction vector lengths* $|\vec{Q}_{11\bar{3}}|$ *(line profile).*

This typical dependence has the consequence that the second and fourth order moments of the intensity distribution exhibit logarithmic and constant asymptotic behaviours, respectively [79]. The resulting slope of the second, the third and the fourth order moments as a function of q is shown in Fig. 5.6.

At large enough q values, before the cut-off introduced by the finite beam size, the second order moment behaves linearly as a function of $ln(q)$ with a slope that is proportional to the average dislocation density of the grain, as shown by the Equation 1.24. The calculation provided a relatively small dislocation density of

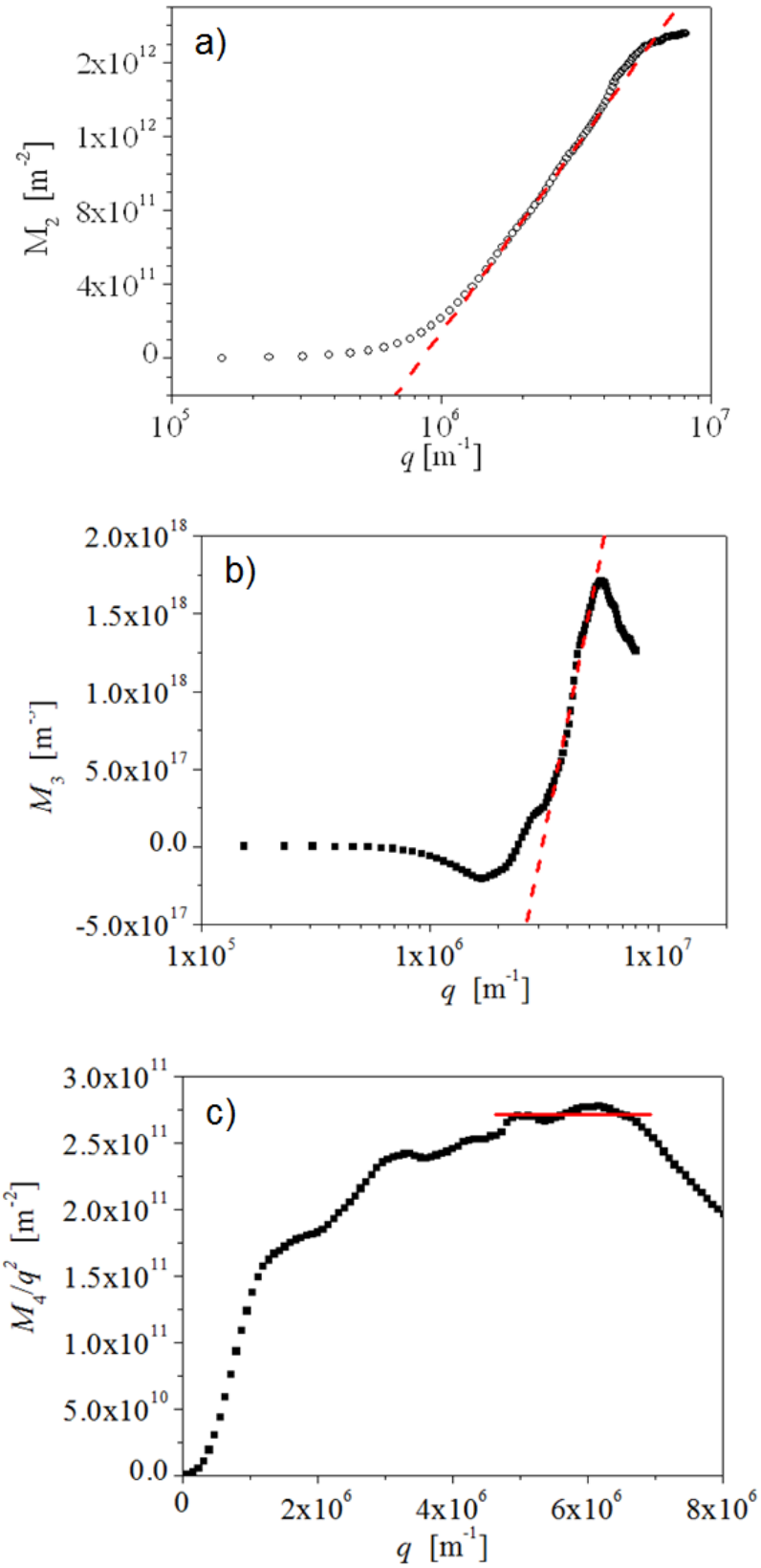

Figure 5.6 – *Variance (a), 3^{rd} (b) and 4^{th} (c) restricted moments of the line profile as a function of log(q) and q, respectively.*

$\rho = 1.8 \times 10^{13}$ m^{-2}, which is in good agreement with the Taylor equation $\tau = \tau_0 + \alpha G b \rho^{-1/2}$, where G is the shear modulus, α a geometrical constant of about 0.3,

and b the magnitude of the Burgers vector for aluminium. Considering τ_0 as negligible and considering that only the slip system $(11\bar{1})[101]$ with the highest Schmidt factor of 0.38 is activated, the Taylor equation provides $\tau = 8$ MPa, which is consistent with the value of the shear stress of 6 MPa, obtained from the flow stress of 15 MPa. A dislocation density value of $\rho = 1.7 \times 10^{13}$ m^{-2} was also obtained from the evaluation of the fourth order moment, which agrees well with the value obtained from the variance.

The third order moment is related to the asymmetry of the peak, and provides an information about the *polarization factor* of the dislocation structure, that is the excess dislocations with a positive or negative sign of the Burgers vector. Ungár et al., (1989) [80] showed that the polarization is directly related to the long-range residual stresses prevailing in the dislocation structure. Its anisotropic dependence can be exploited to analyse the structure of the dislocation walls [81].

5.4 Conclusions

In this chapter, it has been shown that the K-map method introduced by Chahine et al. (2014) [58] allows a full characterization of the crystallographic and elastic heterogeneities created during plastic deformation in single grains of polycrystalline specimens. The distribution of local lattice orientations evaluated by EBSD and XRD were found similar, however, the values got from EBSD are larger, indicating that lattice rotations near the surface of the grain are more important than in the bulk. For the analysed grain, negative strains were found to prevail at the grain interior and large positive strains near grain boundaries. Evidence for the existence of dislocation obstacles inside the grains was found. K-map can also be used for determining grain average properties such as dislocation density and polarization.

6 Conclusions and Perspectives

Contents

6.1 General conclusions

The goal of this thesis was the characterization of grain subdivision mechanisms induced by the formation of geometrically necessary boundaries during uniaxial tensile deformation. An Al-0.1% wt. Mn polycrystal was deformed in situ and illuminated by a monochromatic X-Ray beam in order to carry out a 3DXRD analysis. This kind of analysis overcomes the main disadvantage of the most traditional destructive methods. Moreover, the 3DXRD analysis was carried out for all grains belonging to the illuminated volume ($1000\times1000\times200$ μm^3), which is representative of the bulk material. The dislocation arrangements were characterized through the azimuthal broadening of diffraction spots and interpreted on the basis of the analytical model presented by Barabash et al. [34]. The experimental observations agree with the theoretical predictions when the dislocation content of the boundary is strongly dominated by the presence of one dislocation type. However, the structure of dislocation boundaries was found to be more complicated in the majority of the grains, even at the macroscopic yield stress. The intragranular misorientation axes determined through the analysis of the two most broadened diffraction spots gave very close results to those obtained from EBSD. A satisfactory match was observed: in most cases, a misorientation axis of the same type was found with the two techniques in grains with similar initial orientation.

A stereographic triangle describing the rotation evolution of 72 grains was built, comparing the orientation paths with Taylor model predictions and previous experimental data [65], obtaining satisfactory results with the exception of the area close to the 001 corner. It was found that dislocation wall type strongly depends on grains orientation, as the GND content is dependent on the active slip systems. Finally, the evolution of boundaries structure under loading conditions was investigated, demonstrating that their dislocation content varies linearly with the applied strain and

that other slip systems contribute to form new boundaries as plastic deformation increases.

In Chapter 4 we presented an EBSD based approach which enabled a global quantitative description of grain fragmentation. EBSD cartographies were realized over the same region, evaluating the disorientation between the local orientation and the average orientation of single grains. It was shown that large disorientations develop first near grain boundaries, because lattice planes bending is different in these regions with respect to the grain interior, confirming the results obtained by a previous analytical model [46]. The influence of grain boundaries in grain subdivision was quantified by introducing a characteristic length, which was found to be dependent on grain size but not on grain average orientation.

A new opportunity for a local evaluation of grain fragmentation is represented by a novel X-Ray scanning technique, the K-map scanning [58]. Intragranular disorientation and strain maps were obtained for a grain of an Al-0.1%wt.Mn polycrystal, as well as the average dislocation density arising after the application of a tensile load [59]. A comparison between the disorientation maps obtained by K-map and EBSD on the same grain was performed by means of the implementation of a cross-correlation algorithm. A common trend was observed, though the values of the disorientation angles obtained by K-map are lower than those obtained by EBSD. Considering the higher penetration depth of X-Rays the results show that disorientations are higher near the surface of the specimen than in the interior. The local variation of the lattice parameter with regard to its average value for the grain, allowed the construction of a strain map indicating high strain and orientation gradients caused by dislocations in the grain interior and at the boundary.

6.2 Perspectives

This work opens new insights for polycrystalline materials characterization, on the basis of X-Ray scanning techniques of macroscopic samples. The most logical continuation of this thesis is represented by the projection onto the radial direction of the three dimensional intensity profiles of diffraction spots, which can provide information about the dislocation density and dislocation population of the different slip systems of single grains of a deformed polycrystal. The potential of Line Profile Analysis was already evidenced by the work of Ungar et al. [82] for hexagonal crystals. The authors report on the Burgers vector population, dislocation type and dislocation densities in single grains of a titanium polycrystal of commercial-purity. This analysis was done based on the Wilkens model [83], mainly by considering the width of diffraction peaks recorded with a 2D Freelon detector. It is possible to extend such type of analysis to fcc crystals (which have a smaller number of slip

systems then the hexagonal titanium) by applying the general LPA theory, based on which more accurate results are expected. The key instrument for achieving this aim is the diffraction setup at the new ID31 beamline of the European Synchrotron Radiation Facility equipped with PILATUS detector and detector movement system making possible to record noise free, high resolution spots at high beam energies. This is very important since diffraction spots should cover a large number of pixels to have a good enough peak profile, and the absence of noise makes possible the application of the moments method for the evaluation of the dislocation density.

The application of the K-map technique to characterize strain distribution in one grain of a slightly deformed Al-0.1Mn polycrystal evidenced large strains and strain gradients in the grain interior as well as at grain boundaries. The result obtained is quite remarkable and very different from predictions of continuum models (ex. Finite Element Crystal Plasticity -FECP, which is considered as state of the art engineering tool for predicting plastic properties of polycrystals [84]). It emphasizes the need for developing multiscale plasticity models which better describe stress distribution at the sub-micrometre scale. For this purpose several K-map scans of an in situ deformed specimen can lead to the knowledge on the evolution of intragranular strains, with eventual dislocation cell formation in the initially perfect grains, which was never directly mapped.

Furthermore, this analysis could lead to new knowledge regarding the development of stress concentration at grain boundaries. The subject is highly important since grain boundaries are considered as the weakest regions in a polycrystal, where damage takes place first. For example in creep, cavities nucleate at grain boundaries, then grow and lead to the fracture of the component. An interesting aspect is related to the increased cavity nucleation rate of pre-deformed samples. Existing theories consider that the stress acting on a grain boundary is equal to the applied stress, which is however, insufficient to explain the enhanced nucleation rate due to pre-deformation.

By using the K-map technique it is possible to characterize not only the spatial strain distribution, but the average dislocation density of single grains in a polycrystal, too, which opens new perspectives in the analysis of polycrystal plasticity. Dislocation density has also been determined by Jiang et al. using HR-EBSD [85]. Since the corresponding theory is still under development the EBSD results should be cross-checked by other techniques, for example by classical peak profile analysis. A coupled K-map - HR-EBSD study can provide the direct comparisons between a) local stresses/strains distributions and b) average dislocation densities obtained from HR-EBSD and K-Map, respectively.

Appendix A - Experimental results: orientation maps

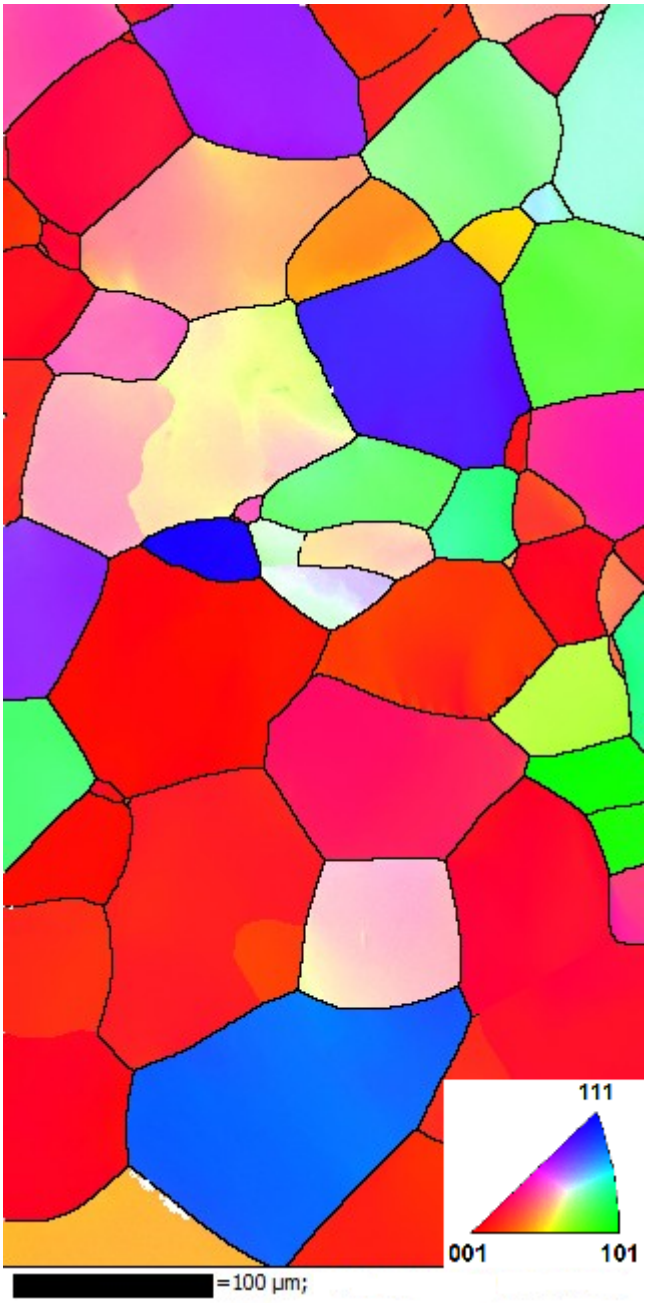

Figure 6.1 – *IPF colour map of Specimen A deformed at* $\varepsilon = 5\%$.

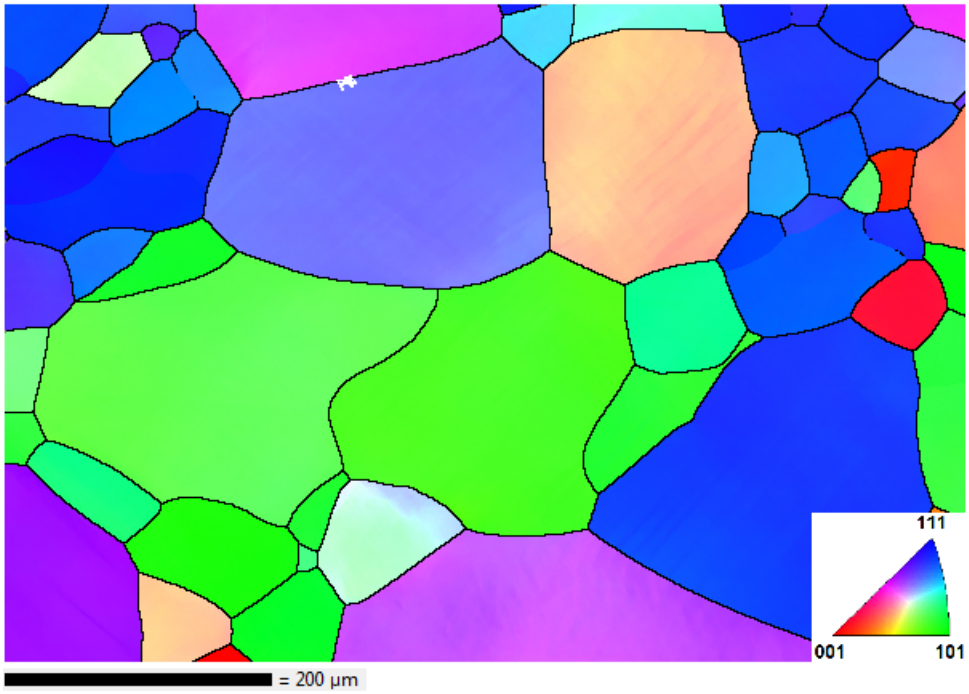

Figure 6.2 – *IPF colour map of Specimen B deformed at* $\varepsilon = 5\%$.

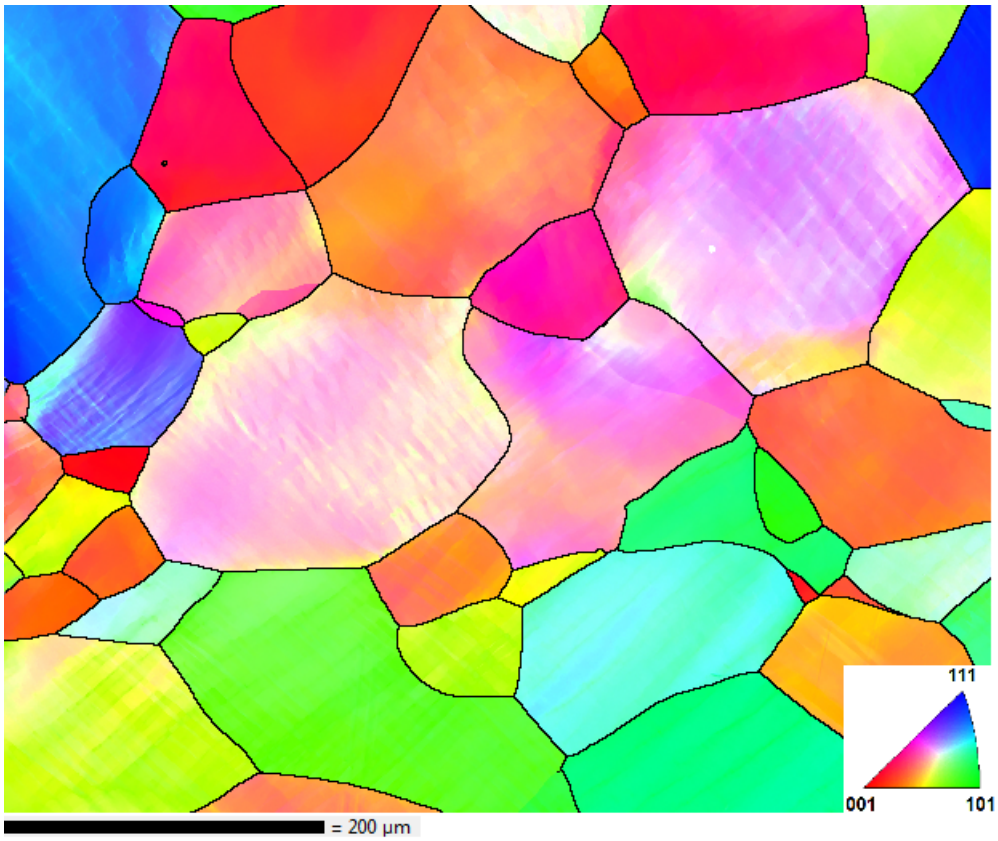

Figure 6.3 – *IPF colour map of Specimen C deformed at* $\varepsilon = 10\%$.

Appendix B - Representation of grain orientation

Grain orientation can be described in different ways. Here we present the representations used in this thesis:

- Orientation matrix.
- Euler angles.
- Rodrigues vector.
- Inverse pole figure.

Orientation matrix

Grain orientation can be represented by an *orientation matrix* U, that links the reference coordinate system (X_S, Y_S, Z_S) to the crystal coordinate system (X_C, Y_C, Z_C). U is defined as:

$$\begin{pmatrix} X_C \\ Y_C \\ Z_C \end{pmatrix} = \begin{pmatrix} U_{11} & U_{12} & U_{13} \\ U_{21} & U_{22} & U_{23} \\ U_{31} & U_{32} & U_{33} \end{pmatrix} \begin{pmatrix} X_S \\ Y_S \\ Z_S \end{pmatrix}$$

By definition, rows represent the components of the crystal coordinates system in the reference system, and similarly columns contain the components of the reference system in the crystal frame. since both the reference and the crystal systems are orthonormal, orientation matrices are always orthonormal, with determinant equal to +1.

Euler angles

The Euler angles represent a sequence of three rotations about the axes of a coordinate system. These rotations start from a known orientation. There are several conventions for Euler angles, depending on the axes about which the rotations are carried out; in Material Science, the most used is the Bunge convention, consisting in three rotations of type Z-X-Z, by the angles (ϕ_1, Φ, ϕ_2), where:

- the first rotation is by an angle $\phi_1 \epsilon [0, 2\pi]$ about the z-axis.
- the second rotation is by an angle $\Phi \epsilon [0, \pi]$ about the new x-axis.
- the third rotation is by an angle $\phi_2 \epsilon [0, 2\pi]$ about the final z-axis.

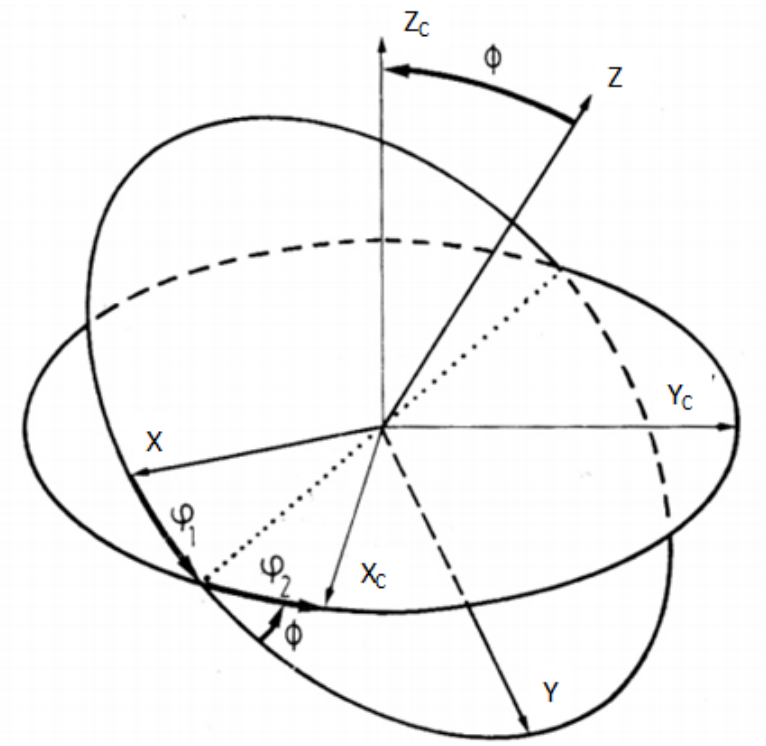

Figure 6.4 – *Definition of the Euler angles following the Bunge convention.*

Rodrigues vector

Any orientation with respect to a reference frame can be described by a Rodrigues vector $\vec{R}$. This vector points to the direction of the rotation axis, and its magnitude is equal to the rotation angle. The Rodrigues vector representation is mostly used for the characterization of grain boundaries in terms of their misorientation axes/angles.

Inverse pole figure

It is possible to represent the directions of the reference coordinate system in the crystal coordinate system; this leads to an *inverse pole figure*. To construct an IPF one consider the a reference sphere (with radius equal to one) attached to the crystal coordinate system. The normal of specific sample plane is plotted on its upper hemisphere. The point of intersection is projected on the equatorial plane by a *stereographic projection*, with spherical coordinates (α,β) defined by the Equation:

$$\begin{pmatrix} sin(\alpha)cos(\beta) \\ sin(\alpha)sin(\beta) \\ cos(\alpha) \end{pmatrix} = \frac{1}{\sqrt{h^2+k^2+l^2}} \cdot U^{-1} \begin{pmatrix} h \\ k \\ l \end{pmatrix}$$

Considering the reference system (X_S, Y_S, Z_S), three inverse pole figures are required for the description of the orientation.

Crystal symmetry leads to a subdivision of the equatorial plane in 24 equivalent

regions in the case of cubic symmetry, as shown in Fig. 6.5

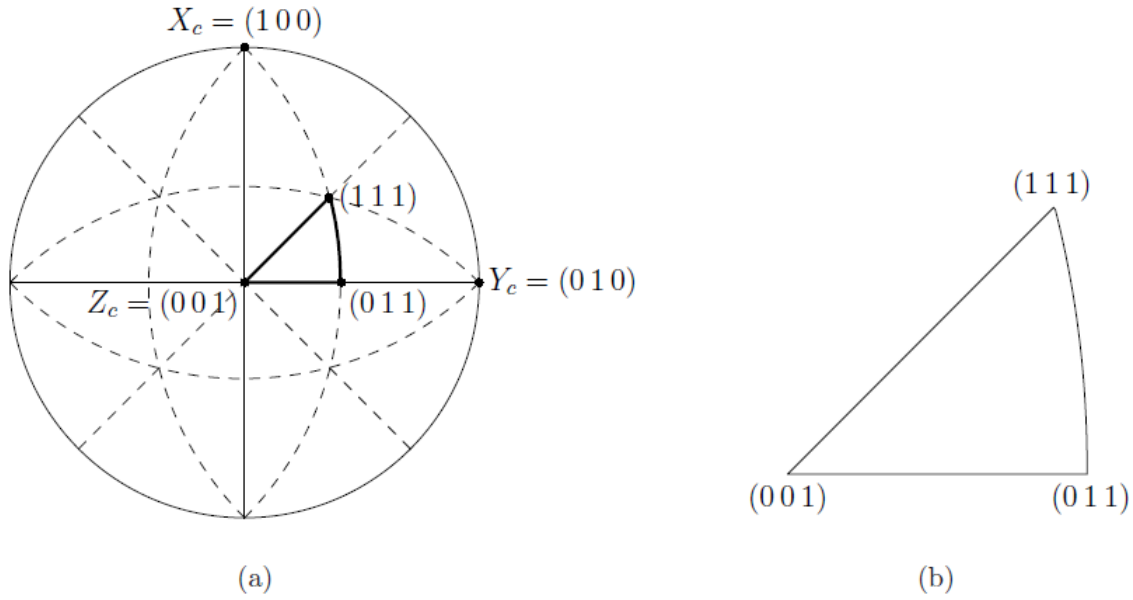

Figure 6.5 – *Equatorial plane of an Inverse Pole Figure. (a) Subdivision of the equatorial plane in 24 equivalent regions in the case of cubic symmetry. (b) stereographic triangle [72].*

References

[1] H. Mughrabi et T. Ungar : Long-range internal stresses in deformed single-phase materials: the composite model and its consequences. *Dislocations in solids*, 11:343–411, 2002.

[2] M. A. Krivoglaz : Theory of x-ray and thermal-neutron scattering by real crystals. 1969.

[3] A. J. Wilkinson, G. Meaden et D. J. Dingley : High-resolution elastic strain measurement from electron backscatter diffraction patterns: new levels of sensitivity. *Ultramicroscopy*, 106(4):307–313, 2006.

[4] C. Maurice, J. H. Driver et R. Fortunier : On solving the orientation gradient dependency of high angular resolution ebsd. *Ultramicroscopy*, 113:171–181, 2012.

[5] J. P. Hirth et J. Lothe : Theory of dislocations. 1982.

[6] D. Hull et D. J. Bacon : *Introduction to dislocations*, vol. 257. Pergamon Press Oxford, 1984.

[7] S. Karato : *Deformation of earth materials: an introduction to the rheology of solid earth*. Cambridge University Press, 2012.

[8] W. F. Hosford : The mechanics of crystals and textured polycrystals. *Oxford University Press(USA), 1993,*, p. 248, 1993.

[9] D. V. Louzguine-Luzgin, L. V. Louzguina-Luzgina et A. Y. Churyumov : Mechanical properties and deformation behavior of bulk metallic glasses. *Metals*, 3(1):1–22, 2012.

[10] G. S. Law : Crystal-plasticity fundamentals. 2009.

[11] D. Kuhlmann-Wilsdorf et N. Hansen : Geometrically necessary, incidental and subgrain boundaries. *Scripta metallurgica et materialia*, 25(7):1557–1562, 1991.

[12] B. Bay, N. Hansen, D. Hughes et D. Kuhlmann-Wilsdorf : Overview no. 96 evolution of fcc deformation structures in polyslip. *Acta metallurgica et materialia*, 40(2):205–219, 1992.

[13] U. Kocks : A statistical theory of flow stress and work-hardening. *Philosophical Magazine*, 13(123):541–566, 1966.

[14] H. Gao et Y. Huang : Geometrically necessary dislocation and size-dependent plasticity. *Scripta Materialia*, 48(2):113–118, 2003.

[15] W. Pantleon : Disorientations in dislocation structures. *Materials Science and Engineering: A*, 400:118–124, 2005.

[16] F. R. Nabarro et M. S. Duesbery : *Dislocations in solids*, vol. 11. Elsevier, 2002.

[17] X. Huang : Grain orientation effect on microstructure in tensile strained copper. *Scripta materialia*, 38(11):1697–1703, 1998.

[18] J. A. Wert, X. Huang, G. Winther, W. Pantleon et H. F. Poulsen : Revealing deformation microstructures. *Materials Today*, 10(9):24–32, 2007.

[19] G. Winther, X. Huang, A. Godfrey et N. Hansen : Critical comparison of dislocation boundary alignment studied by tem and ebsd: technical issues and theoretical consequences. *Acta Materialia*, 52(15):4437–4446, 2004.

[20] G. Winther : Slip systems, lattice rotations and dislocation boundaries. *Materials Science and Engineering: A*, 483:40–46, 2008.

[21] G. Winther : Slip patterns and preferred dislocation boundary planes. *Acta Materialia*, 51(2):417–429, 2003.

[22] G. Winther, L. Margulies, S. Schmidt et H. Poulsen : Lattice rotations of individual bulk grains Part II: correlation with initial orientation and model comparison. *Acta Materialia*, 52(10):2863–2872, 2004.

[23] R. J. McCabe, A. Misra et T. E. Mitchell : Experimentally determined content of a geometrically necessary dislocation boundary in copper. *Acta Materialia*, 52(3):705–714, 2004.

[24] Q. Liu et N. Hansen : Geometrically necessary boundaries and incidental dislocation boundaries formed during cold deformation. *Scripta metallurgica et materialia*, 32(8):1289–1295, 1995.

[25] C. Hong, X. Huang et G. Winther : Dislocation content of geometrically necessary boundaries aligned with slip planes in rolled aluminium. *Philosophical Magazine*, 93(23):3118–3141, 2013.

[26] B. E. Warren : *X-ray Diffraction*. Courier Corporation, 1969.

[27] J. Gubicza : *X-ray line profile analysis in materials science*. IGI Global, 2014.

[28] G. Zilahi, T. Ungár et G. Tichy : A common theory of line broadening and rocking curves. *Journal of Applied Crystallography*, 48(2):418–430, 2015.

[29] M. Wilkens : X-ray line broadening and mean square strains of straight dislocations in elastically anisotropic crystals of cubic symmetry. *Physica status solidi (a)*, 104(1):K1–K6, 1987.

[30] M. Wilkens : Diffraction line broadening of crystals containing small-angle boundaries. *Journal of applied crystallography*, 12(1):119–125, 1979.

[31] A. Borbély et T. Ungár : X-ray line profiles analysis of plastically deformed metals. *Comptes Rendus Physique*, 13(3):293–306, 2012.

[32] H. Mughrabi et B. Obst : Misorientations and geometrically necessary dislocations in deformed copper crystals: A microstructural analysis of X-ray rocking curves. *Zeitschrift für Metallkunde*, 96(7):688–697, 2005.

[33] P. Hirsch, R. Horne et M. Whelan : *LXVIII. Direct observations of the arrangement and motion of dislocations in aluminium*, btitle, 1956.

[34] R. I. Barabash et P. Klimanek : X-ray scattering by crystals with local lattice rotation ®elds. *J. Appl. Cryst*, 32:1050–1059, 1999.

[35] W. Pantleon : On the distribution function of disorientations in dislocation cell structures. *Scripta materialia*, 35(4):511–515, 1996.

[36] L. Priester : *Grain boundaries: from theory to engineering*, vol. 172. Springer Science & Business Media, 2012.

[37] M. Martinez-Hernandez, H. Kirchner, A. Korner, A. George et J. Michel : Dislocations at grain boundaries in deformed silicon. *Philosophical Magazine A*, 56(5):641–658, 1987.

[38] A. Beaudoin Jr, H. Mecking et U. Kocks : Development of localized orientation gradients in fcc polycrystals. *Philosophical Magazine A*, 73(6):1503–1517, 1996.

[39] D. Raabe, Z. Zhao et W. Mao : On the dependence of in-grain subdivision and deformation texture of aluminum on grain interaction. *Acta Materialia*, 50(17):4379–4394, 2002.

[40] D. Hughes, Q. Liu, D. Chrzan et N. Hansen : Scaling of microstructural parameters: misorientations of deformation induced boundaries. *Acta materialia*, 45(1):105–112, 1997.

[41] S. Zaefferer : New developments of computer-aided crystallographic analysis in transmission electron microscopy. *Journal of applied crystallography*, 33(1): 10–25, 2000.

[42] A. Akef et J. Driver : Orientation splitting of cube-oriented face-centred cubic crystals in plane strain compression. *Materials Science and Engineering: A*, 132:245–255, 1991.

[43] F. Basson et J. Driver : Deformation banding mechanisms during plane strain compression of cube-oriented fcc crystals. *Acta materialia*, 48(9):2101–2115, 2000.

[44] D. Hughes et N. Hansen : High angle boundaries formed by grain subdivision mechanisms. *Acta materialia*, 45(9):3871–3886, 1997.

[45] S. Skjervold et N. Ryum : Characterization of local texture in a moderately deformed polycrystalline alsi-alloy. *Acta metallurgica et materialia*, 43(8):3159–3176, 1995.

[46] L. S. Tóth, Y. Estrin, R. Lapovok et C. Gu : A model of grain fragmentation based on lattice curvature. *Acta Materialia*, 58(5):1782–1794, 2010.

[47] J. Wright : *ImageD11*, btitle, 2005.

[48] H. F. Poulsen : *3DXRD–a new probe for materials science*. Risø National Laboratory, 2004.

[49] N. Gueninchault, H. Proudhon et W. Ludwig : Nanox: a miniature mechanical stress rig designed for near-field x-ray diffraction imaging techniques. *Journal of synchrotron radiation*, 23(6), 2016.

[50] G. Sachs : Plasticity problems in metals. *Transactions of the Faraday Society*, 24:84–92, 1928.

[51] G. J. Taylor : Analysis of plastic strain in a cubic crystal. *Journal of the Institue of Metals*, 62:307, 1938.

[52] J. Oddershede, J. Wright, A. Beaudoin et G. Winther : Deformation-induced orientation spread in individual bulk grains of an interstitial-free steel. *Acta Materialia*, 85:301–313, 2015.

[53] H. Poulsen, L. Margulies, S. Schmidt et G. Winther : Lattice rotations of individual bulk grains. *Acta Materialia*, 51(13):3821–3830, 2003.

[54] L. Renversade, R. Quey, W. Ludwig, D. Menasche, S. Maddali, R. M. Suter et A. Borbely : Comparison between diffraction contrast tomography and high-energy diffraction microscopy on a slightly deformed aluminium alloy. *IUCrJ*, 3(1), 2016.

[55] L. Nervo, A. King, J. P. Wright, W. Ludwig, P. Reischig, J. Quinta da Fonseca et M. Preuss : Comparison between a near-field and a far-field indexing approach for characterization of a polycrystalline sample volume containing more than 1500 grains. *Journal of Applied Crystallography*, 47(4):1402–1416, 2014.

[56] L. Nervo, A. King, J. P. Wright, W. Ludwig, P. Reischig, J. Quinta Da Fonseca et M. Preuss : Comparison between a near-field and a far-field indexing approach for characterization of a polycrystalline sample volume containing more than 1500 grains. *Journal of Applied Crystallography*, 2014.

[57] R. Quey : *Suivi de microtextures dans l'aluminium en grande déformation à chaud*. Thèse de doctorat, Ecole Nationale Supérieure des Mines de Saint-Etienne, 2009.

[58] G. A. Chahine, M. I. Richard, R. A. Homs-Regojo, T. N. Tran-Caliste, D. Carbone, V. L. R. Jaques, R. Grifone, P. Boesecke, J. Katzer, I. Costina, H. Djazouli, T. Schroeder et T. U. Schülli : Imaging of strain and lattice orientation by quick scanning X-ray microscopy combined with three-dimensional reciprocal space mapping. *Journal of Applied Crystallography*, 2014.

[59] E. Filippelli, G. Chahine et A. Borbély : Evaluation of intragranular strain and average dislocation density in single grains of a polycrystal using k-map scanning. *Journal of Applied Crystallography*, 49(5):1814–1817, 2016.

[60] R. Lebensohn et C. Tomé : A self-consistent viscoplastic model: prediction of rolling textures of anisotropic polycrystals. *Materials Science and Engineering: A*, 175(1-2):71–82, 1994.

[61] C. Tomé, R. A. Lebensohn et U. Kocks : A model for texture development dominated by deformation twinning: application to zirconium alloys. *Acta metallurgica et materialia*, 39(11):2667–2680, 1991.

[62] W. R. Busing et H. A. Levy : Angle calculations for 3- and 4-circle X-ray and neutron diffractometers. *Acta Crystallographica*, 22(4):457–464, 1967.

[63] A. Householder : numerical treatment of a single nonlinear equation. 1973.

[64] H. Mughrabi et B. Obst : Misorientations and geometrically necessary dislocations in deformed copper crystals: a microstructural analysis of x-ray rocking curves. *Zeitschrift für Metallkunde*, 96(7):688–697, 2005.

[65] G. Winther, L. Margulies, S. Schmidt et H. F. Poulsen : Lattice rotations of individual bulk grains Part II: correlation with initial orientation and model comparison. *Acta Materialia*, 52(10):2863–2872, 2004.

[66] H. F. Poulsen, L. Margulies, S. Schmidt et G. Winther : Lattice rotations of individual bulk grains: Part I: 3D X-ray characterization. *Acta materialia*, 51(13):3821–3830, 2003.

[67] R. Pokharel, J. Lind, S. F. Li, P. Kenesei, R. A. Lebensohn, R. M. Suter et A. D. Rollett : In-situ observation of bulk 3d grain evolution during plastic deformation in polycrystalline cu. *International Journal of Plasticity*, 67:217–234, 2015.

[68] M. Kamaya, A. J. Wilkinson et J. M. Titchmarsh : Quantification of plastic strain of stainless steel and nickel alloy by electron backscatter diffraction. *Acta Materialia*, 54(2):539–548, 2006.

[69] M. Kamaya : Measurement of local plastic strain distribution of stainless steel by electron backscatter diffraction. *Materials Characterization*, 60(2):125–132, 2009.

[70] R. Suter, D. Hennessy, C. Xiao et U. Lienert : Forward modeling method for microstructure reconstruction using x-ray diffraction microscopy: Single-crystal verification. *Review of Scientific Instruments*, 77(12):123905, 2006.

[71] G. Daveau : *Interaction dislocations-joints de grains en déformation plastique monotone: étude expérimentale et modélisations numériques*. Thèse de doctorat, Ecole Centrale Paris, 2012.

[72] R. Quey : *ORILIB. A collection of routines for orientation manipulation*, btitle, 2012.

[73] J. C. Glez et J. Driver : Orientation distribution analysis in deformed grains. *Journal of Applied crystallography*, 34(3):280–288, 2001.

[74] M. Yoo et H. Trinkaus : Interaction of slip with grain boundary and its role in cavity nucleation. *Acta metallurgica*, 34(12):2381–2390, 1986.

[75] A. Borbely, C. Maurice et J. H. Driver : Rotation axis analysis of deformed crystals by x-rays and electrons. *Journal of Applied Crystallography*, 41(4):747–753, 2008.

[76] T. Ungt'ar, H. Mughrabi et M. Wilkt'ens : An x-ray line-broadening study of dislocations near the surface and in the bulk of deformed copper single crystals. *Acta Metallurgica*, 30(10):1861–1867, 1982.

[77] J. Jiang, T. B. Britton et A. J. Wilkinson : Mapping type iii intragranular residual stress distributions in deformed copper polycrystals. *Acta Materialia*, 61(15):5895–5904, 2013.

[78] I. Groma : X-ray line broadening due to an inhomogeneous dislocation distribution. *Physical Review B*, 57(13):7535, 1998.

[79] A. Borbély et I. Groma : Variance method for the evaluation of particle size and dislocation density from x-ray bragg peaks. *Applied Physics Letters*, 79(12):1772–1774, 2001.

[80] T. Ungár, I. Groma et M. Wilkens : Asymmetric x-ray line broadening of plastically deformed crystals. ii. evaluation procedure and application to [001]-cu crystals. *Journal of applied crystallography*, 22(1):26–34, 1989.

[81] I. Groma et G. Monnet : Analysis of asymmetric broadening of x-ray diffraction peak profiles caused by randomly distributed polarized dislocation dipoles and dislocation walls. *Journal of applied crystallography*, 35(5):589–593, 2002.

[82] T. Ungár, G. Ribárik, L. Balogh, A. A. Salem, S. L. Semiatin et G. B. Vaughan : Burgers vector population, dislocation types and dislocation densities in single grains extracted from a polycrystalline commercial-purity ti specimen by x-ray line-profile analysis. *Scripta Materialia*, 63(1):69–72, 2010.

[83] M. Wilkens : Theoretical aspects of kinematical x-ray diffraction profiles from crystals containing dislocation distributions(fourier transform of x ray diffraction line profiles from crystals with dislocations). *NBS Fundamental Aspects of Dislocation Theory*, 2, 1970.

[84] M. Miller et P. Dawson : Understanding local deformation in metallic polycrystals using high energy x-rays and finite elements. *Current Opinion in Solid State and Materials Science*, 18(5):286–299, 2014.

[85] J. Jiang, T. Britton et A. Wilkinson : Evolution of dislocation density distributions in copper during tensile deformation. *Acta Materialia*, 61(19): 7227–7239, 2013.

École Nationale Supérieure des Mines
de Saint-Étienne

NNT : *Communiqué le jour de la soutenance*

Ernesto Francesco Filippelli

NON DESTRUCTIVE ANALYSIS OF GRAIN SUB-STRUCTURATION IN SINGLE GRAINS OF AN ALUMINIUM POLYCRYSTAL DEFORMED IN UNIAXIAL TENSION

Speciality : Materials Science

Keywords : polycrystal, GNDs, 3DXRD, EBSD, K-map, intragranular strain, grain subdivision, aluminium

Abstract :

This work aims to improve the understanding of grain subdivision mechanisms and dynamics during deformation of polycrystals. For this purpose, in situ synchrotron experiments and EBSD acquisitions were coupled to study the response of single grains of an Al-0.1%wt.Mn polycrystal during tensile deformation. The specimen deformed in situ at the synchrotron was analyzed by 3DXRD. A new method provided a grain-by-grain analysis of the intragranular misorientation axes and their orientation distribution, through the investigation of the azimuthal broadening of diffraction spots. The 3DXRD results were crosschecked by classical EBSD analysis. Three acquisitions were carried out over the same region of interest at the undeformed state and after the application of 1% and 5% strain. Thanks to the available spatial resolution, the EBSD results allow for a better comprehension of the creation and dynamics of intragranular orientation gradients, and are in good agreement with pre-existing theoretical models. In addition, the characterization of grain subdivision and intragranular strain was performed through a novel scanning X-Ray technique, the K-map. The strain was found to be very heterogeneous with high compressive and tensile values in the grain interior and near two grain boundaries, respectively. The distribution of the magnitude of diffraction vectors indicated that dislocations are the origin of the strain.

École Nationale Supérieure des Mines
de Saint-Étienne

NNT : *Communiqué le jour de la soutenance*

Ernesto Francesco Filippelli

ANALYSE NON DESTRUCTIVE DE LA SOUS-STRUCTURATION DES GRAINS INDIVIDUELS DANS UN POLYCRYSTAL D'ALUMINIUM DÉFORMÉ EN TRACTION UNIAXIALE

Spécialité : Science et Génie des Matériaux

Mots clefs : polycrystal, GNDs, 3DXRD, EBSD, K-map, fragmentation des grains, déformation intragranulaire, aluminium

Résumé :

Ce travail vise à améliorer la compréhension des mécanismes et de la dynamique de fragmentation des grains pendant la déformation des matériaux polycristallins. Pour cela, des expériences in situ en synchrotron et des acquisitions EBSD ont été menées afin d'étudier les comportements des grains individuels d'un polycristal d'Aluminium déformé plastiquement. Une éprouvette d'un alliage Al-0.1%Mn a été déformée en traction in situ et analysée par microscropie 3D par diffraction des rayons X (3DXRD). Une nouvelle méthode de dépouillement a été developpée pour determiner les axes de désorientations intragranulaires et les distributions d'orientation, grâce à l'analyse de l'élargissement azimutal des tâches de diffraction. La technique EBSD a été appliquée pour obtenir des cartographies de désorientation des grains individuels d'une éprouvette déformée en traction. Trois acquisitions ont été réalisées sur la même région d'intérêt à l'état non déformé et après l'application des déformations 1% et 5%. Ces résultats permettent une meilleure compréhension de la formation et de l'évolution des gradients d'orientations intragranulaires, et sont en bon accord avec les modèles théoriques pré-existants. Aussi, la caractérisation de la fragmentation des grains et de la déformation intragranulaire a été réalisée grâce à la technique K-map. La déformation était très hétérogène avec des valeurs élevées de compression et de traction à l'intérieur des grains et à proximité de deux joints de grains, respectivement. La distribution de la norme des vecteurs de diffraction a montré que les dislocations sont à l'origine de la déformation.